Draft version August 24, 2016
Preprint typeset using LaTeX style emulateapj v. 12/16/11

AN ALMA SURVEY OF SUB-MILLIMETRE GALAXIES IN THE EXTENDED *CHANDRA* DEEP FIELD SOUTH: SPECTROSCOPIC REDSHIFTS

A. L. R. Danielson,[1,2] A. M. Swinbank,[1,2] Ian Smail,[1,2] J. M. Simpson,[1,2] C. M. Casey,[3,4] S. C. Chapman,[5] E. da Cunha,[6] J. A. Hodge,[7] F. Walter,[8] J. L. Wardlow,[1,2] D. M. Alexander,[1,2] W. N. Brandt,[9] C. de Breuck,[10] K. E. K. Coppin[11] H. Dannerbauer,[12] M. Dickinson,[13] A. C. Edge,[1] E. Gawiser,[14] R. J. Ivison,[10] A. Karim,[5] A. Kovacs,[15] D. Lutz,[16] K. Menten,[17] E. Schinnerer,[7] A. Weiss,[17] P. van der Werf,[7]

Draft version August 24, 2016

ABSTRACT

We present spectroscopic redshifts of $S_{870\mu m} \gtrsim 2$ mJy submillimetre galaxies (SMGs) which have been identified from the ALMA follow-up observations of 870-μm detected sources in the Extended *Chandra* Deep Field South (the ALMA-LESS survey). We derive spectroscopic redshifts for 52 SMGs, with a median of $z = 2.3 \pm 0.2$. However, the distribution features a high redshift tail, with $\sim 23\%$ of the SMGs at $z > 3$. Spectral diagnostics suggest that the SMGs are young starbursts, and the velocity offsets between the nebular emission and UV-ISM absorption lines suggest that many are driving winds, with velocity offsets up to $2000\,\mathrm{km\,s^{-1}}$. Using the spectroscopic redshifts and the extensive UV-to-radio photometry in this field, we produce optimised spectral energy distributions (SEDs) using Magphys, and use the SEDs to infer a median stellar mass of $M_\star = (6 \pm 1) \times 10^{10}\,\mathrm{M_\odot}$ for our SMGs with spectroscopic redshift. By combining these stellar masses with the star-formation rates (measured from the far-infrared SEDs), we show that SMGs (on average) lie a factor ~ 5 above the so-called "main-sequence" at $z \sim 2$. We provide this library of 52 template fits available as a resource for future studies of SMGs, and also release the spectroscopic catalog of all ~ 2000 (mostly infrared-selected) galaxies targeted as part of the spectroscopic campaign.

Subject headings: galaxies: starburst, submillimetre: galaxies

1. INTRODUCTION

Submillimeter galaxies (SMGs) with 850μm fluxes of $S_{850} > 1$ mJy represent a population of dusty starbursts whose space density peaked ~ 10 Gyr ago. Although they are relatively rare, their far-infrared luminosities ($L_{\rm IR} > 2 \times 10^{12}\,\mathrm{L_\odot}$) imply high star formation rates ($\gtrsim 300\,\mathrm{M_\odot\,yr^{-1}}$) and so SMGs appear to contribute up to 20% of the total cosmic star formation rate density over $z = 1$–4 (e.g. Chapman et al. 2005; Barger et al. 2012; Casey et al. 2014; Swinbank et al. 2014). If they can maintain their star formation rates, SMGs also have the potential to consume all their cold gas reservoir within just 100 Myr (e.g. Tacconi et al. 2008; Bothwell et al. 2013), and so double their stellar masses within their short but blazing lifetime (e.g. Hainline et al. 2009; Magnelli et al. 2012). Their ability to form up to $10^{11}\,\mathrm{M_\odot}$ of stars within a short period of time makes them reasonable candidates of progenitors of $z = 1$–2 compact quiescent galaxies (Toft et al. 2014; Simpson et al. 2015a; Ikarashi et al. 2015) as well as local massive ellipticals (e.g. Lilly et al. 1999; Genzel et al. 2003; Swinbank et al. 2006; Simpson et al. 2014). These characteristics suggest that bright SMGs represent an essential population for models of galaxy formation and evolution (e.g. Efstathiou & Rowan-Robinson 2003; Baugh et al. 2005; Swinbank et al. 2008; Narayanan et al. 2009; Davé et al. 2010; Hayward et al. 2011; Lacey et al. 2015).

However, to identify the physical processes that trigger the starbursts, measure the internal dynamics of the cold (molecular) and ionised gas, and infer stellar masses first requires accurate redshifts. To date, the largest such spectroscopic survey of 870μm-selected SMGs was carried out by Chapman et al. (2005) who targeted a sample of 104 radio-identified, SCUBA-detected submil-

[1] Institute for Computational Cosmology, Department of Physics, Durham University, South Road, Durham DH1 3LE, UK
[2] Centre for Extra Galactic Astronomy, Department of Physics, Durham University, South Road, Durham DH1 3LE, UK
[3] Department of Astronomy, The University of Texas at Austin, 2515 Speedway Boulevard Stop C1400, Austin, TX 78712, USA
[4] Department of Physics and Astronomy, University of California, Irvine, Irvine, CA 92697, USA
[5] Department of Physics and Atmospheric Science, Dalhousie University, Halifax, NS B3H 4R2, Canada
[6] Research School of Astronomy and Astrophysics, Australian National University, Canberra, ACT 2611, Australia
[7] Leiden Observatory, Leiden University, P.O. Box 9513, 2300 RA Leiden, The Netherlands 0000-0001-5434-5942
[8] Max-Planck-Institut für Astronomie, Königstuhl 17, D-69117 Heidelberg, Germany
[9] Department of Astronomy and Astrophysics and the Institute for Gravitation and the Cosmos, The Pennsylvania State University
[10] European Southern Observatory, Karl Schwarzschild Straße 2, 85748, Garching, Germany
[11] Centre for Astrophysics Research, Science and Technology Research Institute, University of Hertfordshire, College Lane, Hatfield AL10 9AB, UK
[12] Universität Wien, Institut für Astrophysik, Türkenschanzstraße 17, 1180, Wien, Austria
[13] National Optical Astronomy Observatory, Tucson, AZ 85719, USA
[14] Department of Physics and Astronomy, Rutgers University, Piscataway, NJ 08854-8019, USA
[15] Astronomy Department, University of Minnesota, MN 12345, USA
[16] Max-Planck-Institut für extraterrestrische Physik, Giessenbachstraße, 85748, Garching, Germany
[17] Max-Planck-Institut für Radioastronomie, Auf dem Hügel 69, D-53121 Bonn, Germany

limetre sources spread across seven extragalactic survey fields. Using rest-frame UV spectroscopy with the Low-resolution Imaging Spectrograph (LRIS) on Keck, they derived spectroscopic redshifts for 73 SMGs with a median redshift of $z\sim2.3$ for the radio-selected sample (with a maximum redshift in their sample of $z=3.6$).

Although the requirement for a radio detection in these previous surveys was a necessary step to identify the most probable galaxy counterpart responsible for the sub-mm emission, the radio wavelengths do not benefit from the same negative K-correction as submillimetre wavelengths and indeed, above $z\sim3.5$, the 1.4 GHz flux of a galaxy with a star formation rate of $\sim100\,\mathrm{M_\odot\,yr^{-1}}$ falls below $\sim15\mu$Jy and so below the typical sensitivity limit of deep radio surveys. This has the potential to bias the redshift distribution to $z\lesssim3.5$, especially if a significant fraction of sub-mm sources do not have multi-wavelength counterparts. Indeed, in single dish 850μm surveys, up to 50% of all submillimetre sources are undetected at radio wavelengths (e.g. Ivison et al. 2005, 2007; Biggs et al. 2011). Some progress can be made by targeting lensed sources whose multi-wavelength identifications are less ambiguous, and indeed spectroscopic redshifts have been derived for SMGs up to $z\sim5$ (e.g. Weiß et al. 2013).

Due to the angular resolution and sensitivity of the ALMA interferometer, it has become possible to identify the counterparts of sub-mm sources to $\lesssim0.3''$ accuracy without recourse to statistical asssociations at other wavelengths. To identify a sample of SMGs in a well studied field with a well defined selection function, we undertook an ALMA survey of 122 SMGs found in the ECDFS: the "ALESS" survey (Hodge et al. 2013). This survey followed up 122 of the 126 submillimetre sources originally detected with the LABOCA instrument on the Atacama Pathfinder Experiment 12 meter telescope (APEX) selected (the LESS survey Weiß et al. 2009). Each LESS submillimetre source was targeted with ALMA at 870μm (Band 7). The typical FWHM of the ALMA synthesised beam was $\sim1.5''$ (significantly smaller than the LABOCA 19.2$''$ beam), thus allowing us to directly pinpoint the position of the SMG precisely.

From these data, Karim et al. (2013) (see also Simpson et al. 2015b) showed that statistical identifications (e.g. using radio counterparts) provide mis-identifications in ~30% of cases, whilst the single-dish sub-mm sources also suffer from significant "multiplicity", with >35% of the single dish sources resolved into multiple SMGs brighter than $\gtrsim1$ mJy. This flux limit corresponds approximately to a far-infrared luminosity of $\mathrm{L_{FIR}}\gtrsim10^{12}\,\mathrm{L_\odot}$ at $z\sim2$, and so it appears that a large fraction of the single-dish sub-mm sources often contain two (or more) ULIRGs. Consequently, a new ALESS SMG catalog was defined comprising 131 SMGs (Hodge et al. 2013).

One of the primary goals of the ALESS survey is to provide an unbiased catalog of SMGs for which we can derive cold molecular gas masses, as well as measure spatially resolved dynamics of the gas and stars in order to identify the trigering mechanisms that cause the burst of star formation. The first necessary step in this process is to derive the precise spectroscopic redshifts. To this end, we have undertaken a spectroscopic survey of ALMA-identified SMGs using VLT, Keck and Gemini (supplemented by ALMA) and in this paper we describe the UV, optical and near-infrared spectroscopic follow-up. We use the resulting redshifts to investigate the redshift distribution, the environments and typical spectral features of these SMGs. In addition, we use these precise redshifts to better constrain the SED fitting from UV-to-radio wavelengths and provide template SEDs for the ALESS SMG population.

The structure of the paper is as follows. We discuss the observations and the data reduction in § 2, followed by redshift identification and sample properties in § 3. In § 4 we show the ALESS redshift distribution and discuss the spectroscopic completeness. In § 5 we discuss the velocity offsets of various different spectral lines, search for evidence of stellar winds and galaxy-scale outflows and investigate the environments of SMGs and the individual and composite spectral properties. We present our conclusions in § 6. In the Appendix, we give the table of ALESS SMG redshifts and provide information on individual SMGs from the sample.

Unless otherwise stated the quoted errors on the median values within this work are determined through bootstrap analysis. Throughout the paper we use a ΛCDM cosmology with $\mathrm{H_0}=72\,\mathrm{km\,s^{-1}\,Mpc^{-1}}$, $\Omega_\mathrm{m}=0.27$ and $\Omega_\Lambda=1-\Omega_\mathrm{m}$ (Spergel et al. 2003) and a Chabrier initial mass function (IMF; Chabrier 2003). Unless otherwise noted, all magnitudes are on the AB system.

2. OBSERVATIONS AND REDUCTION

2.1. *Sample definition*

The 870μm LESS survey (Weiß et al. 2009) was undertaken using the LABOCA camera on APEX, covering an area of 0.5×0.5 degrees centered on the ECDFS. The total exposure time for the survey was 310 hours, reaching a 1σ sensitivity of $\sigma_{870\mu\mathrm{m}}\sim1.2\,\mathrm{mJy\,beam^{-1}}$ with a beam of 19.2$''$ FWHM. In total, we identified 126 submillimetre sources above a signal-to-noise of 3.7σ. Follow-up observations of the LESS sources were carried out with ALMA (the ALMA-LESS, ALESS program). Details of the ALMA observations are described in Hodge et al. (2013) but in summary, the 120 s observations for each source were taken between October and November 2011 in the Cycle 0 Project #2011.1.00294.S. These submillimetre interferometric identifications confirmed some of the probabilistically determined counterparts (Biggs et al. 2011; Wardlow et al. 2011) but also revealed some mis-identified counterparts and a significant number of new counterparts. Therefore, the ALESS SMG catalog was formed, comprising a main (hereafter MAIN) catalog of the 99 of the most reliable ALMA-identified SMGs (i.e. lying within the the primary beam FWHM of the best-quality maps). A supplementary (hereafter SUPP) catalog was also defined comprising 32 ALMA-identified SMGs extracted from outside the ALMA primary beam, or in lower quality maps (Hodge et al. 2013). When searching for spectroscopic redshifts, we included both the MAIN and SUPP sources, and in § 4 we demonstrate that the inclusion of SUPP sources makes very little quantitative difference to the statistics of the redshift distribution.

To search for spectroscopic redshifts, we initiated an observing campaigh using the the FOcal Reducer and low dispersion Spectrograph (FORS2) and VIsible MultiObject Spectrograph (VIMOS) on VLT, but to supplement these observations, and in particular to increase the wavelength coverage and probability of determining redshifts, we also obtained observations with XSHOOTER on VLT, the Gemini Near-Infrared Spectrograph (GNIRS) and the Multi-Object Spectrometer for Infra-Red Exploration (MOSFIRE) on the Keck I telescope, all of which cover the near-infrared. As part of a spectroscopic campaign targeting *Herschel*-selected galaxies in the ECDFS, ALESS SMGs were included on DEep Imaging Multi-Object Spectrograph (DEIMOS) slit masks on Keck II (e.g. Casey et al. 2012). These observations probe a similar wavelength range to FORS2 targeting some of the ALMA-identified SMGs that could not be targeted with VLT (due to slit collisions). In total, we observed 109 out of the 131 ALESS SMGs. In many cases we have ALESS SMGs with spectra from five different spectrographs covering a broad wavelength range and we cross check the spectroscopic redshifts across all of the instruments. Next, we discuss the various instruments involved in our survey. We note that for all observations described below, flux calibration was carried out using standard stars to calibrate instrumental response.

2.2. *VLT FORS2 / VIMOS*

Our spectroscopic program aimed to target as many of the ALESS SMGs as possible using a dual approach with FORS2 and VIMOS (for a typical SMG redshift of $z\sim1$–3, we are sensitive to Lyα and UV ISM lines with VIMOS or [OII] $\lambda3727$ with FORS2). In total, we observed for 100 hours each with VIMOS and FORS as part of programme 183.A-0666. We used ten (overlapping) VIMOS masks to cover the field, plus sixteen FORS masks (which cover a sub-set of the field but target the regions with the highest density of ALMA SMGs; Fig. 1). All of the FORS observations were carried out in grey time and all of the VIMOS observations carried out in dark time during service mode runs with seeing $\leq 0.8''$ and clear sky conditions (transparency variations below 10%). Our dual-instrument approach allowed us to probe a large wavelength range using VIMOS LR-Blue grism (4000–6700Å) and FORS2 300I (6000 - 11000 AA). When designing the slit masks, the first priority was always given to the SMGs, but we also infilled the masks with other mid- or far-infrared selected galaxies from the FIDEL *Spitzer* survey (Magnelli et al. 2009), the HerMES and PEP *Herschel* surveys of this field (Oliver et al. 2012; Lutz et al. 2011), $S_{1.4\mathrm{GHz}} > 30\mu$Jy radio sources and *Chandra* X-ray sources (Lehmer et al. 2005; Luo et al. 2008) or optical/near-infrared colour selected galaxies (see Table A1 and Fig. 15).

In Fig. 1 we show the spectroscopic coverage of the ECDFS from our FORS2 and VIMOS programs, where the darkest areas demonstrate the areas with the longest total exposure time and the FORS2 pointings are overlaid. In total, we recorded 5221 galaxy spectra, targeting 2454 (unique) galaxies.

2.2.1. *FORS2*

FORS2 covers the the wavelength range $\lambda = 3300$–11000Å and provides an image scale of $0.25''$ pix^{-1} in the standard readout mode (2×2 binning). FORS2 was used in its multi-object spectroscopy mode with exchangeable masks (MXU). We varied the slit length and orientation for each target in order to observe the maximum number of sources on each mask (Fig. 1), but we consistently used a slit width of $1''$. We used ∼40 – 70 slits per mask and the OG590 order-sorting filter with the 300I grism which results in a wavelength range covering 6000–11000Å. The typical resolution in this configuration is $R = \lambda\,/\,\Delta\lambda\sim660$. We used 16 pointings, although in a small number of cases, we moved slits between exposures if there were multiple sources within $\sim5''$ which could not be simultaneously observed on a mask. Each mask was observed in blocks of 3×900 s with each exposure nodded up and down the slits by $\sim1.0''$ to aid sky-subtraction and cosmic-ray removal when the images were combined. Each mask was typically observed six times (with a range of three to nine times depending on the number of SMGs on the mask and their median brightness), resulting in an on-source exposure time 4.5 hrs (with a range of 2.25 – 6.75 hr).

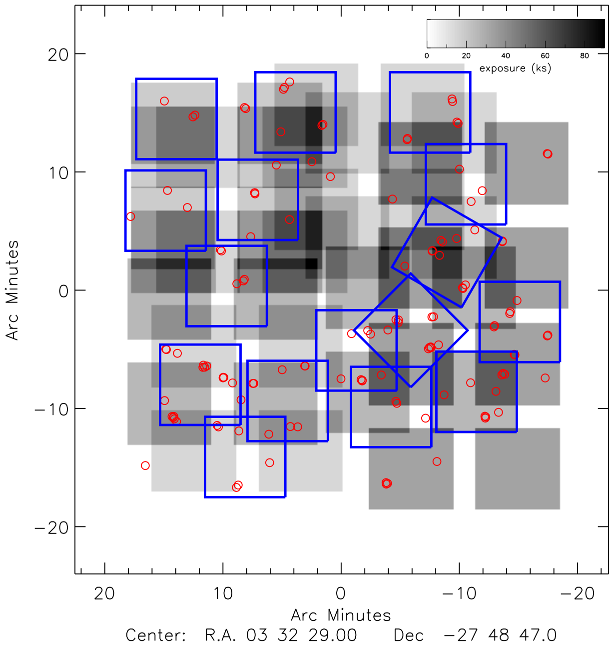

Fig. 1.— The coverage of our 10 VIMOS pointings (greyscale) and 16 FORS2 pointings (blue boxes) in the ECDFS. The ALESS SMG positions are shown as small red circles. VIMOS has four quadrants separated by small gaps. There is significant overlap between the VIMOS pointings, we therefore show the pointings here with the darkest areas corresponding to the regions with the longest total exposure time. Our FORS2/VIMOS programme covers 62 out of the 109 targeted SMGs in the ECDFS.

We reduced the data using the spectroscopic reduction package from Kelson (2003) adapted for use with FORS2 data FORS2 pipeline[18]. The pipeline produces two-dimensional, bias-corrected, flat-fielded, wavelength-calibrated, sky-subtracted images. Individual exposures were combined in two-dimensions by taking a median of the frames and sigma clipping. We then extracted one-dimensional spectra over the full spatial-extent of the continuum/emission lines visible, or in the case where

---

[18] http://www.ucolick.org/h̃olden/datareducetext/kelsonware.html

no emission was obvious in the two-dimensional image, we extracted data from the region around the expected source position.

2.2.2. *VIMOS*

The VIMOS observations were undertaken in multi-object spectroscopy (MOS) mode. VIMOS consists of four quadrants each of a field-of-view of $7' \times 8'$ with a detector pixel scale of $0.205''$. Each observing block comprised 3×1200 s exposures dithering $\pm 1.0''$ along the slit. The exposure time per mask was 3 – 9 hr, again depending on the number of SMGs on the mask and their average brightness. Slit widths of $1.0''$ were used, for which the typical resolution is $R \sim 180$ and the dispersion is 5.3Å/pixel for the LR_blue grism with the OS_blue order sorting filter (~ 4000 – 6700Å). We used 40 – 160 slits per quadrant, totalling 160 – 400 slits over the four quadrants. The data were reduced using the standard ESOREX pipeline package for VIMOS. The frames were stacked in two-dimensions before extracting the one-dimensional spectra. In a number of cases, the data suffer from overlapping spectra which results in a second order overlapping the adjacent spectrum (this can be seen in the VIMOS two-dimensional spectrum of ALESS 057.1 in Fig. 2).

2.3. *XSHOOTER*

To improve the wavelength coverage of our observations, we also obtained XSHOOTER observations of 20 ALESS SMGs. XSHOOTER simultaneously observes from UV to near-infrared wavelengths covering wavelength ranges of 3000 – 5600Å, 5500 – 10200Å and 10200 – 24800Å for the UV (UVB), visible (VIS) and near-infrared (NIR) arms respectively. Targets were prioritised for XSHOOTER follow-up based on their K-band magnitudes. Our XSHOOTER observations were taken in visitor mode as part of programme 090.A-0927(A) from 2012 December 7 – 10 in dark time. We observed each source for ~ 1hr in generally clear conditions with a typical seeing of $\sim 1.0''$. Our observing strategy was 4×600 s exposures per source, nodding the source up and down the slit. The pixel scales were 0.16, 0.16 and $0.21''$ pix^{-1} for the UVB, VIS and NIR arms respectively. The slits were all $11''$ long and $0.9''$ wide for the VIS and NIR arms and $1.0''$ wide for the UVB arm. The typical resolution was $R \sim 4350$, 7450, 5300 for the UVB, VIS and NIR arms respectively. The data reduction was carried out using the standard ESOREX pipeline package for XSHOOTER.

2.4. *MOSFIRE*

We also targeted 36 ALESS SMGs with the MOSFIRE spectrograph on Keck I (2012B_H251M, 2013B_U039M, and 2013B_N114M) in H- (1.46 – 1.81μm) and K-band (1.93 – 2.45μm). Observations were taken in clear or photometric conditions with the seeing varying from 0.4 – $0.9''$. In all cases we used slits of width $0.7''$. The pixel scale of MOSFIRE is $0.18''$ pix^{-1} and the typical spectral resolution for this slit width is $R \sim 3270$. The total exposure time per mask was 2.2 – 3.6 ks which was split in to 120 s (H-band) and 180 s (K-band) exposures, with an ABBA sequence and a $1.5''$ nod along the slit between exposures. Data reduction was completed with MOSPY[19].

2.5. *DEIMOS*

We targeted 71 of the ALESS SMGs as "mask infill" during a Keck II DEIMOS spectroscopy program to measure redshifts for *Herschel* / SPIRE sources (program 2012B_H251). The data were taken on 2012 December 9 – 10 in clear conditions with seeing between 1 – $1.3''$. We used a setup with the 600ZD (600 lines mm^{-1}) grating with a 7200Å blaze angle and the GG455 blocking filter which resulted in a wavelength range of 4850 – 9550Å. Slit widths of $0.75''$ were used and the masks were filled with 40 – 70 slits per mask. The pixel scale of DEIMOS is 0.1185" pix^{-1} and the typical resolution was $R \sim 3000$. Individual exposures were 1200 s, and the total integration times were 2–3 hrs. The data were reduced using the DEEP2 DEIMOS data reduction pipeline (Cooper et al. 2012; Newman et al. 2013).

2.6. *GNIRS*

The Gemini Near-Infrared Spectrograph (GNIRS) was used to target eight ALESS SMGs as (program GN-2012B-Q-90) between 2012 November 10 – 15 and December 4 – 23. The targets were selected based on their K-band magnitude and whether they had a photometric redshift that was predicted to place strong emission lines in the near-infrared. The instrument was used in cross-dispersing mode (via the SXD prism with 32 lines / mm), using the short camera, with slit widths of $0.3''$, slit lengths of $7''$ and a pixel scale of $0.15''$ pix^{-1}. The wavelength coverage with this setup is 9000–25600Å, typically with $R \sim 1700$. Our observing strategy comprised 200 s exposures and nodding up and down the slit by ~ 1". Each observing block comprised eight coadds of three exposures, resulting in an exposure of ~1.3 hr per source. The GNIRS data were reduced using the Gemini IRAF package.

2.7. *ALMA*

Spectroscopic redshifts for two of our SMGs, ALESS 61.1 and ALESS 65.1 were determined from serendipitous detections of the [CII]λ158μm line in the ALMA band (Swinbank et al. 2012). Although based on single line identifications, both redshifts have been confirmed by the identification of ^{12}CO(1–0) emission using ATCA (Huynh et al. 2013; Huynh et al. 2016 submitted).

Once all of the data were collected from the different spectrographs, we collated the spectra for each ALESS SMG. The instruments used to observe each SMG are listed in Table 2.

3. ANALYSIS

3.1. *Redshift identification*

To determine redshifts for the sample, all one- and two-dimensional spectra were independently examined by two investigators (AMS and ALRD). Any emission / absorption features that were identified were fit

---

[19] MOSPY is a publicly available python reduction package for MOSFIRE data written by Nick Konidaris (https://code.google.com/p/mosfire/wiki/mospy)

with a Gaussian profiles to determine their central wavelengths. In the FORS2, VIMOS and DEIMOS data the most commonly identified lines were Lyα, Civ $\lambda\lambda$1548.89,1550.77 Å , Ciii λ1909 Å , Heii λ1640 AA and [Oii]$\lambda\lambda$3726.03,3728.82 Å . In the near-infrared, we typically detect Hα, Nii λ6583 and [Oiii] $\lambda\lambda$4959, 5007 and in a small number of cases, Hβ (see Tables 1 and 2). The optical / near-infrared counterparts of the SMGs are often faint and we detect continuum in only $\sim$ 50% of the 52 SMGs for which we determine a redshift, (compared to $\sim$ 75% in Chapman et al. 2005).

The spectra often only contain weak continuum, emission and / or absorption lines, making redshifts difficult to determine robustly. We therefore assign four quality flags to our spectroscopic data:

1. Q = 1 denotes a secure redshift where multiple features were identified from bright emission / absorption lines;

2. Q = 2 denoted a secure redshift but derived from one or two bright emission (or strong absorption) lines;

3. Q = 3 is a tentative redshift based on one (or sometimes two tentative) emission or absorption lines. In these cases, we often use the photometric redshift as a guide to identify the line. These redshifts are therefore not independent of the photometric redshifts and are thus highlighted in the analysis;

4. Q = 4 is assigned to galaxies with no emission lines or continuum detected and so no redshift could be determined.

Examples of spectra from which Q = 1, 2 and 3 redshifts are determined are shown in Fig. 2. Since the ECDFS has been the focus of extensive spectroscopic campaigns (although focusing mainly on bright optical/UV-selected galaxies) six of our ALMA SMGs have already published spectroscopic redshifts, and we highlight these in Table 2 (see also Appendix § A).

The emission / absorption lines we are using to derive redshifts have a range of physical origins within the galaxies. For example, nebular emission lines arise from Hii regions and so are expected to trace the systemic redshift, whereas UV-ISM lines can trace outflowing material and can be offset from the systemic by several 100 km s^{-1} (e.g. Erb et al. 2006; Steidel et al. 2010). Lyα emission, which is often used to derive spectroscopic redshifts, also suffers resonant scattering. As such, to derive redshifts for each galaxy we adopt the following approach:

1. Wherever possible, systemic redshifts are determined using nebular emission lines such as Hα, [Oii] $\lambda\lambda$3726,3729, [Oiii] $\lambda\lambda$4959,5007 and/or Hβ. If none of these lines are available we use Heii or Ciii] λ1909 in emission if they are narrow.

2. If no nebular emission lines are detected, we determine the mean of the redshifts from the UV ISM absorption lines of Cii λ1334.53, Siiv λ1393.76 and Siii λ1526.72, or other strong emission lines such as Nv λ1240, Mgii λ2800 and Heii.

TABLE 1
Summary of spectroscopic features

Condition	Number of galaxies TOTAL [SUP]
TOTAL	131 [32]
Q=1	20 [1]
Q=2	11 [3]
Q=3	21 [3]
Redshifts measured	52 [7]
Not observed	22 [10]
Observed but no specz	58 [15]
Lyα	23 [1]
[OII]	10 [3]
[OIII]	6 [0]
Hα	14 [3]
[OIII] and Hα	3 [0]
Hβ	3 [0]

Notes: The numbers in brackets represents the number of sup sources contributing to the total in each row.

3. If Lyα is the *only* detected line then the redshift is determined from a fit to this line, although we caution that the velocity offset from the systemic can be up to $\sim$ 1000 km s^{-1}. In most of the galaxies where a redshift is determined solely from Lyα, the observations were taken with VIMOS using the low-resolution (R $\sim$ 180) grating, precluding any detailed analysis to determine the shape of the emission line. Similarly, where possible we avoid using Civ λ1549 for measuring the redshifts, since it can be strongly influenced by winds and frequently exhibits a profile which is a superposition of P-Cygni emission and absorption, nebular emission and interstellar absorption (or AGN activity).

For the ALESS SMGs, $\sim$ 30% of the redshifts are determined from a single line and generally these redshifts are allocated Q = 3 unless strong continuum features (such as breaks across Lyα) are also identified, which leads to an unambiguous identification and a higher quality flag. Single line redshifts are typically backed up by either continuum breaks across Lyα, the absence of other emission lines that would correspond to a different redshift, line profiles (i.e. asymmetric Lyα profile or identifying the doublet of [Oii] λ3726, 3729 emission). In seven cases, single line redshifts are based on detections of Lyα; in three cases they are determined from Hα detections in near-infrared spectra and in five cases they are from detections of the [Oii] doublet.

We summarise the main spectroscopic features that we detect in Table 1 and provide detailed information on each of the 109 observed SMGs in Table 2.

In Fig. 3 we compare the spectroscopic and photometric redshifts distribution for the ALESS SMGs, and compare this to the photometric redshift distribution for these SMGs from Simpson et al. (2014) who determine photometric redshifts for 77 of the ALESS SMGs which have 4 – 19 band photometry (we highlight the Q = 3 redshifts in this plot since their spectroscopic identification is often guided by the photometric redshifts). However, even if these Q = 3 SMGs are omitted, there is good

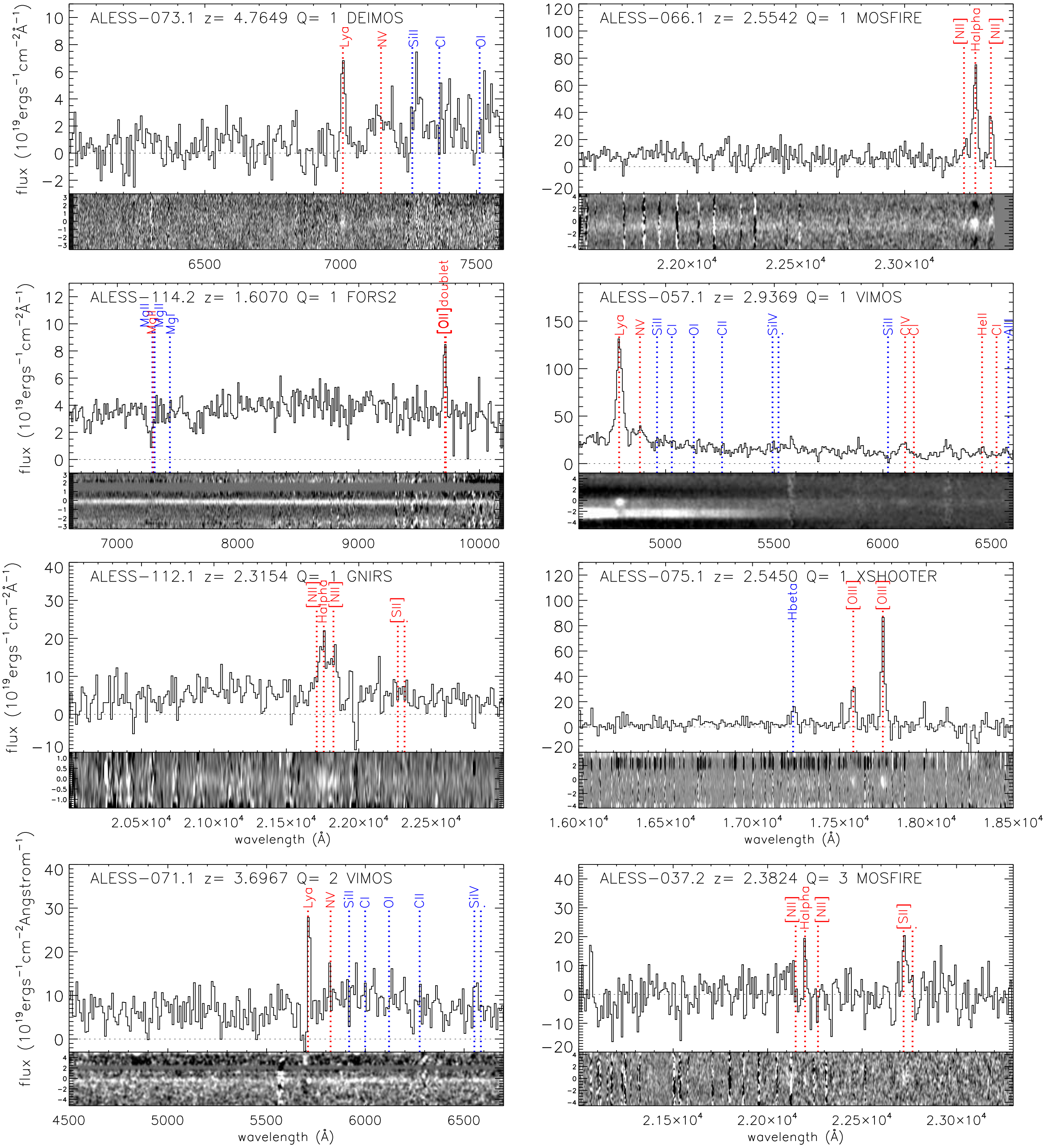

FIG. 2.— Example one- and two-dimensional spectra of ALESS SMGs from each spectrograph used. The upper three rows are high quality ($Q=1$) spectra while the bottom row shows lower quality examples ($Q=2$ and 3 spectra) and we mark identified and potential features in all panels, where red dashed lines mark typical emission lines and blue dashed lines mark typical absorption lines. In ALESS 057.1 (an X-ray AGN) the bright continuum below the central strong emission line and continuum is contamination from higher order emission from an adjacent slit on the VIMOS mask. ALESS 037.2 is an example of a $Q=3$ redshift where the redshift is determined from narrow Hα, although the apparent ratio of SII / Hα is unusually high.

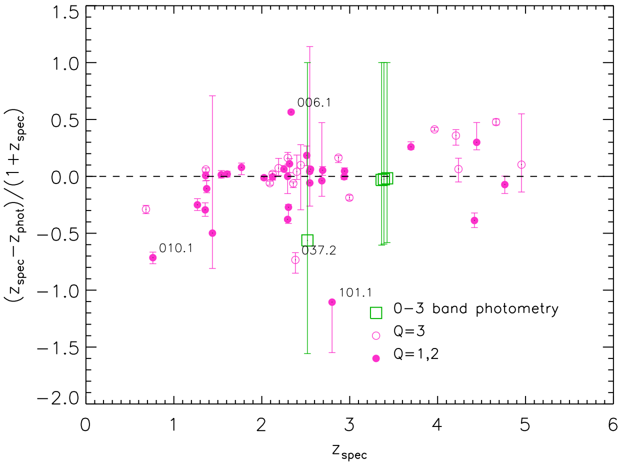

FIG. 3.— A comparison of the spectroscopically and photometrically-derived ALESS redshifts (Simpson et al. 2014). The green squares represent those SMGs with photometric detections in only 0 − 3 bands where the redshift has been determined by assuming these SMGs have an absolute *H*-band magnitude distribution comparable to that of a complete sample of $z \sim 1-2$ SMGs. For SMGs with 0 − 1, and 2 − 3 band photometry we set the photometric redshift at the median for those sources of $z \sim 4.5$ and $z \sim 3.5$ respectively. The errors represent the errors on the photometric redshifts determined from the SED fitting in Simpson et al. (2014). Overall, there is good agreement between the photometric and spectroscopic redshifts with a median $\Delta z/(1+z_{\rm spec}) = 0.00 \pm 0.02$.

agreement between the photometric and spectroscopic redshifts with a median $\Delta z/(1 + z_{\rm spec}) = 0.00 \pm 0.02$ and a variance of $\sigma^2 = 0.1$. In four cases, there appear to be significant outliers, with $|\Delta z/(1 + z_{\rm spec}))| > 0.5$. In these cases, the large offset between the photometric and spectroscopic redshifts appears to be associated with complex systems or incomplete photometric coverage, and we briefly discuss these here:

1. ALESS 006.1: the photometry of the ALESS SMG appears to contaminated by an adjacent low-redshift (and unassociated) QSO, and in this case it appears that the SMG is lensed. The photometry (and photometric redshift) is dominated by the foreground QSO.

2. ALESS 010.1: the Q = 1 spectroscopic redshift is significantly lower than predicted by the photometry. There is a blue source slightly offset ($< 1''$) from the ALMA position and an IRAC source coincident with the ALMA position. *HST* imaging (Chen et al. 2015) reveals two galaxies and it is possible that the blue source is a lens (as confirmed by high-resolution, $\sim 0.1''$ ALMA band 7 follow-up observations; Hodge et al. 2016).

3. ALESS 037.2: the Q = 3 spectroscopic redshift is significantly lower than the $z > 4$ predicted by the photometry. However, the spectroscopic redshift is based on two tentative line detections at the correct separation for Hα and [SII] (see Fig. 2; [NII], if present would lie under strong sky lines) and the photometric redshift is poorly constrained and based on detections in six bands and limits in a further six. Furthermore, the spectroscopic line identifications would not correspond to any common emission lines if the photometric redshift is correct;

4. ALESS 101.1: this has a Q = 2 redshift based on a single detection of Lyα. It has poor constraints on the photometric redshift with photometric detections in only five bands and no detections below *J*-band. Thus the spectroscopic redshift is significantly more reliable.

For a significant fraction of the ALMA sample, we were unable to derive a spectroscopic redshift (these are assigned $Q = 4$ in Table 2). To understand test whether this is caused by magnitude limits or their redshifts, first we compare the photometric redshifts of the spectroscopic failures to those for the SMGs for which we were able to determine a spectroscopic redshift. The median photometric redshift of spectroscopic failures is $z = 2.4 \pm 0.2$, compared to $z = 2.3 \pm 0.1$ for the sources for which we were able to measure a spectroscopic redshift. This suggests that the spectroscopic failures are not systematically SMGs at higher redshifts. There does not appear to be any correlation with sub-mm flux ($S_{870\mu{\rm m}}$) either. For the 52 SMGs with spectroscopic redshifts, the median 870-μm flux is $S_{870\mu{\rm m}} = 4.2 \pm 0.3$ mJy, whereas for those 57 SMGs where we could not determine a redshift the median $S_{870\mu{\rm m}} = 4.3 \pm 0.3$ mJy.

Instead, that for some ALMA SMGs, no spectroscopic redshift could be determined is simply due to their optical magnitudes. In Fig. 4 we show the distributions of the $S_{870\mu{\rm m}}$ flux density, *R*-band magnitude, 4.5μm magnitude and 1.4 GHz flux density for the 109 (out of 131) ALESS SMGs that were spectroscopically targeted. The median *R*-band magnitude of the ALESS SMGs with spectroscopic redshifts is $R = 24.0 \pm 0.2$ whereas the median magnitude of those sources for which we could not measure a redshift is $\sim$ 1-magnitude fainter, at $R = 25.0 \pm 0.4$. Turning to longer wavelengths, in the mid-infrared, the median magnitude at 4.5μm is $m_{4.5\mu{\rm m}} = 20.9 \pm 0.2$ for the ALESS SMGs with spectroscopic redshifts, as compared to a median of $m_{4.5\mu{\rm m}} = 21.7 \pm 0.2$ for those targeted SMGs for which we could not derive a spectroscopic redshift. Thus, the ALESS SMGs for which we were able to determine a spectroscopic redshift are marginally brighter in *R* and $m_{4.5\mu{\rm m}}$ than those for which we were unable to determine a spectroscopic redshift. In Fig. 5 we plot the redshifts of the ALESS SMGs versus their 4.5μm apparent magnitudes. At the typical redshift of SMGs ($z \sim 2.5$), the 4.5μm flux provides the most reliable tracer of the underlying stellar mass, since it corresponds to rest-frame 1.6μm (*H*-band). As a guide, to crudely test how the 4.5μm magnitude depend on redshift in our sample, we generate a non-evolving starburst track, based on the composite SED for the ALESS SMGs (shown in Simpson et al. 2014 but updated to contain the spectroscopic redshift information in Fig. 9). This model has been normalised to the median apparent magnitudes measured at 4.5μm for the SED at the median redshift of $z \sim 2.4$. The dependence of 4.5μm flux with redshift for our spectroscopic sample is consistent with this track, although with a spread of ~ 2 magnitudes at fixed redshift. However, the data do show a trend of decreasing 4.5μm flux with

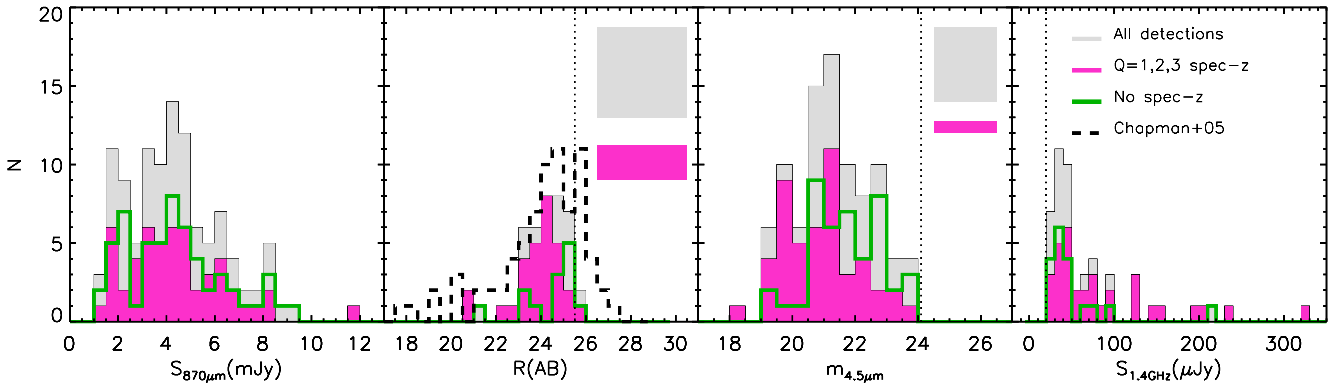

FIG. 4.— Sample properties showing histograms of the sample in different bands (where the sample comprises the 109/131 SMGs that were targeted in our spectroscopic survey). Grey regions represents the sample (with or without spectroscopic redshifts); solid magenta represents the SMGs with Q = 1, 2 or 3 spectroscopic redshifts. The green lines represent SMGs with photometry but no spectroscopic redshift. The grey boxes show the area covered by the subset of SMGs with no photometric detection and no spectroscopic redshift and the magenta boxes show the subset with spectroscopic redshifts but no photometric detections. The dotted lines show the 3σ detection limits in the specified bands. We note that ALESS 020.1 has a very high radio flux density of ~ 4.2 mJy and is therefore not shown within this plot range. The dashed line in the second panel shows the comparison with the *R*-band magnitude distribution of the 73 C05 SMGs. On average, the SMGs for which we were able to determine a redshift are marginally brighter in *R*-band, and $m_{4.5\mu m}$ than those for which we were unable to determine a redshift, however, the likelihood of determining a redshift is independent of the $S_{870\mu m}$ flux density.

increasing redshift. Smail et al. (2004) (see also Serjeant et al. 2003) also identify a similarly large spread in *K*-band magnitudes for SMGs which is be attributed to either a large mass range in the SMGs (a demonstration of the diversity of the SMG population), and/or varying levels of strong dust extinction.

In Fig. 5 we have highlighted the ten multi-component SMGs that appear to be pairs (or triples) on $\sim$3–12$''$ ($\sim$25–100 kpc) scales with spectroscopic redshift offsets between components $\leq$ 2000 km s^{-1}. The median apparent magnitude at 4.5μm for these ten SMGs is $m_{4.5\mu\mathrm{m}} = 20.8 \pm 0.6$ as compared to a median of $m_{4.5\mu\mathrm{m}} = 21.1 \pm 0.2$ for the 52 ALESS SMGs in the parent spectroscopic sample. Thus, these SMGs in 'associations' appear to be marginally brighter and thus potentially more massive than those not in 'associations' which may be expected if these sources lie in overdense structures.

In terms of the radio-detected sub-sample, from the entire MAIN+SUPP ALESS catalog, 53 / 131 ALESS SMGs are radio-detected, and we have targeted 52 with spectroscopy, measuring redshifts for 34. The median 1.4 GHz flux density of the SMGs with spectroscopic redshifts is $S_{1.4\mathrm{GHz}} = 63 \pm 12\mu$Jy compared to $S_{1.4\mathrm{GHz}} = 39 \pm 6\mu$Jy for those without spectroscopic redshifts (Fig. 4). Thus, SMGs for which we were unable to determine a spectroscopic redshift are fainter at radio wavelengths than those for which we measured a spectroscopic redshift.

4. SPECTROSCOPIC REDSHIFT DISTRIBUTION

The spectroscopic redshift distribution of the ALESS SMGs is shown in Fig. 6. In total 52 redshifts have been determined for the ALESS SMGs: 45 MAIN catalog SMGs and seven SUPP catalog SMGs. We also overlay the probability density function of the photometric redshift distribution of ALESS SMGs from Simpson et al. (2014), scaled to the peak of the spectroscopic redshift distribution. The Q = 1, 2 and Q = 1, 2, 3 distributions are shown as individual histograms to test the effect of including the Q = 3 redshifts. The full redshift distribution ranges between $z = 0.7$–5.0.

In Fig. 7 we show the ALESS spectroscopic redshift distribution and compare this with the spectroscopic sample of radio-identified SMGs from Chapman et al. (2005), the 1.1-mm selected (U)LIRGs from the recent ALMA / UDF image from Dunlop et al. (2016) and the (lensed) South Pole Telescope (SPT) sample from Weiß et al. (2013) (Strandet et al. 2016, see also). Given the different selection wavelengths and flux limit between the ALESS SMGs, ALMA / UDF galaxies and the SPT sample, we caution against drawing far-reaching conclusions between these redshift distributions (Béthermin et al. 2015). Nevertheless, all of these distributions peak at $z \sim 2.5 \pm 0.5$, and those that do not rely on pre-selection have significant (but not dominant) tails out to $z \sim 5$.

Before continuing with the analysis, we briefly assess the effect on our sample of including the SUPP SMGs and those with only Q = 3 redshifts. Karim et al. (2013) demonstrate that up to $\sim$30% of the SUPP sources are likely to be spurious. However, clearly SUPP sources which have an optical / near-infrared counterpart have a lower liklihood of being spurious sources. The median redshift of the MAIN catalog SMGs with Q = 1, 2, 3 redshifts is $z = 2.5 \pm 0.1$ with an interquartile range of $z = 2.1$–3.4, whereas the median redshift of the MAIN+SUPP catalog with Q = 1, 2, 3 redshifts is $z = 2.4 \pm 0.1$ with an interquartile range of $z = 2.1$–3.0. The median redshift of the Q = 1, 2 and 3 SMGs in the SUPP sample alone is $z = 2.3 \pm 0.5$. Thus, the median redshifts of these various samples are all consistent. Indeed, a two-sided Kolmogorov-Smirnov (K-S) test between the MAIN and SUPP samples suggests a $< 1\sigma$ probability that they are drawn from different populations. Since the statistics of the samples do not vary strongly with the inclusion of the SUPP sources, we are therefore confident that including the SUPP sources in our analyses does not bias any of our results.

Since previous SMGs redshift surveys have, by necessity, relied on radio detections to identify the probablistic counterparts, we briefly discuss the properties of the radio-detected subset of the ALESS SMGs, as this pro-

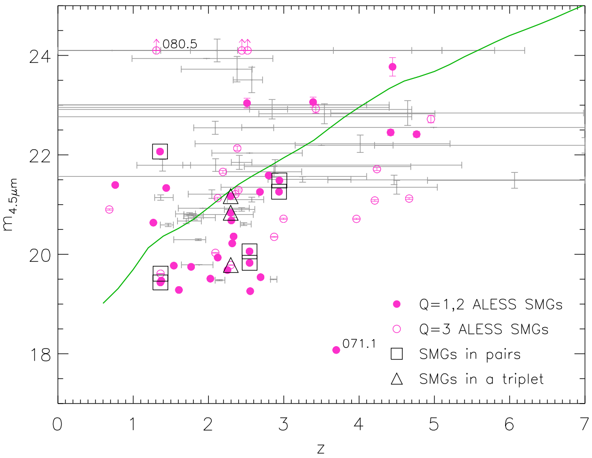

FIG. 5.— IRAC-4.5μm magnitude versus redshift. Photometric redshifts (where spectroscopic redshifts are not available) are shown as their $\pm 1\sigma$ ranges given in Simpson et al. (2014) and Table 2. The solid green line provides the expected variation with redshift for a non-evolving fixed luminosity galaxy, assuming the composite ALESS SED from Simpson et al. (2014) (see also Fig. 9). The track is normalised to the median apparent magnitude in 4.5μm at a median redshift of $z = 2.4$. Those SMGs which are found to be physically associated (pairs or triples) with other SMGs are highlighted. Those in associations tend to be among the brightest SMGs (and therefore likely to be among the most massive; see § 5.3. The outliers are labelled with their ALESS ID.

vides a reasonable comparison to previous work. In our sample we targeted 52 of the 53 radio-detected SMGs with spectroscopy and measured redshifts for 34 of them (65%). The median 1.4 GHz radio flux density of the 34 radio-detected ALESS SMGs with spectroscopic redshifts is $63 \pm 12\mu$Jy, as compared to $50 \pm 7\mu$Jy for *all* 52 radio-detected SMGs. In contrast, the median radio flux density of the 73 radio-detected SMGs in Chapman et al. (2005) with spectroscopic redshifts is $75 \pm 6\mu$Jy. On average, the radio-detected ALESS SMGs with redshifts are ~20% fainter at 1.4 GHz than the Chapman et al. (2005) sample and our spectroscopic completeness is 10% lower. We note that it apears that the Chapman et al. (2005) SMGs have a higher AGN fraction than our ALESS sample, and indeed up to ~40% of their SMG sample exhibit signatures of AGN activity in the X-rays, spectra or from their broad-band optical/mid-infrared SEDs (e.g. Alexander et al. 2008; Hainline et al. 2011). Wang et al. (2013) find an AGN fraction of $\sim 17^{+16}_{-6}\%$ for the ALESS SMGs. Typically AGN spectra have stronger, more easily identifiable emission features and thus our 10% lower spectroscopic completeness may be due to a lower AGN fraction.

5. DISCUSSION

Although the primary aim of this work is to determine the redshifts of unambiguously identified SMGs to support further detailed follow-up (e.g. CO or Hα dynamics), there is also a wealth of information contained within the spectra themselves concerning the dynamics, chemical composition, and energetics of these SMGs. Furthermore, the redshifts can be used as constraints in SED models (e.g. constraining the star formation history and so the stellar masses) and to investigate the environments in which these SMG reside.

5.1. *Spectral diagnostics*

5.1.1. *Stacked spectral properties*

Stacking spectra provides a useful tool to detect weak features that are not visible in individual spectra and for determining average properties of the population. We therefore produce a composite spectra over two different wavelength ranges, covering Lyα + UV ISM lines and that around the [OII] emission, searching for evidence of strong emission/absorption features and continuum breaks. To construct the composites, we first transform each spectrum to the rest-frame using the *best* redshift in Table 2. Where the sky subtraction leaves significant residuals, the region within ±5Å of the sky lines are masked before stacking (and we use the OH line catalog in the near-infrared from Rousselot et al. 2000 to identify the bright sky lines in the near-infrared). We then sum the spectra, inverse weighted by the noise (measured as the standard deviation in the region of continuum over which they have been normalised). In the case of the 1000 – 2000Å composite (Fig. 8), we normalise the spectra by their median continuum value at > 1250Å and in the case of the composite around 3400 – 4400Å (Fig. 9), we normalise by the median continuum value between 2900 – 3600Å. We note that when transforming the spectra to the rest-frame, in a number of cases, the UV ISM lines and Lyα can be significantly offset in velocity from this systemic redshift (see Fig. 12). In the rest-frame UV, the spectral features may therefore appear broadened.

We first discuss the composite spectra around Lyα. In Fig. 8 we show the composite around the range 1000 – 2000Å. First we combine only the Q = 1 and 2 spectra. We note that due to the different wavelength ranges of the different instruments used and the fact that we de-redshift and stack in the rest-frame, not all the spectra in the stack contribute to the full wavelenth range. This composite demonstrates strong Lyα and a continuum break at ~ 1200Å. The spectrum displays strong SiII absorption, potentially offset SiIV absorption and CIV and CIII] emission. There appears to be a significantly blueshifted SiIV feature and potentially blueshifted CIV which may be indicative of strong stellar winds. We also overlay the composite spectrum of ~ 200 Lyman break galaxies (LBGs) from Shapley et al. (2003) (the LBG composite shown here corresponds to the quartile of 200 LBGs from the Shapley et al. (2003) sample that has the closest match in Lyα equivalent width to our ALESS sample). also show the Q = 3 composite, which broadly validates the Q = 3 redshifts since Lyα and CIII] are identifiable in the composite.

To search for continuum breaks and Balmer absorption lines, and provide an independent measure of the luminosity weighted age of the stellar population, we also produce a rest-frame composite of the Q = 1 and 2 spectra over the wavelength range of 3400 – 4400Å (removing the bright X-ray AGN from the sample; Wang et al. 2013) and show this in Fig. 9. We detect strong [OII], Ca H&K and Hδ (Fig. 9). Furthermore, the continuum begins to fall off bluewards of ~ 3900Å. A break in this region can be due to the 4000Å break, typically observed in older stellar systems, or the Balmer break at ~3656Å. The Balmer break arises in stellar populations which

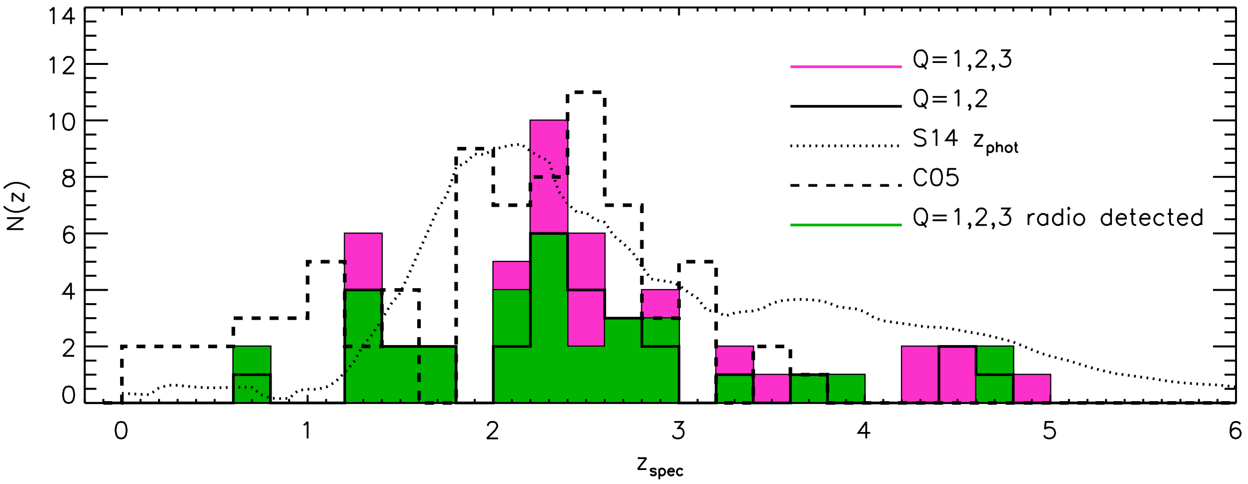

FIG. 6.— The spectroscopic redshift distribution of the SMGs in the ECDFS. The bin size is $\Delta z = 0.2$. The secure redshifts (Q = 1, 2) are shown as well as all Q = 1, 2 and 3 redshifts. We compare the distribution to the probability density function of the photometric redshifts from Simpson et al. (2014). We also compare to the SMG redshift distribution from Chapman et al. (2005), shown here as a dashed line. In order to compare the Chapman et al. (2005) redshift distribution directly with our sample, the radio-detected ALESS SMGs are highlighted. This shows that there are discernable differences between the redshift distributions of the radio-detected ALESS SMGs and that from the Chapman et al. (2005) sample. We note that the ALESS SMGs have a redshift distribution that extends to higher redshift, with $\sim 23\%$ of the SMGs at $z > 3$.

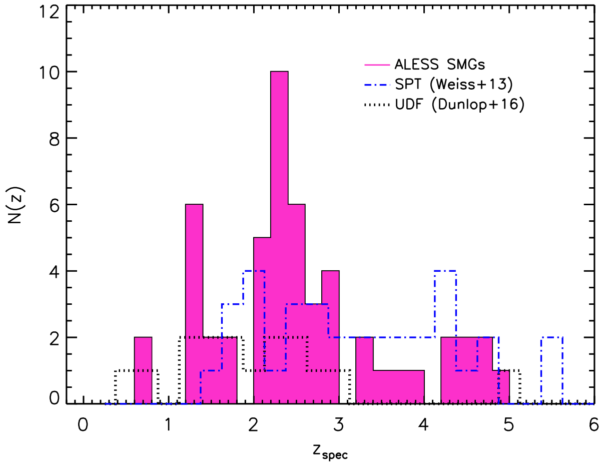

FIG. 7.— The spectroscopic redshift distribution of the SMGs in the ECDFS compared to that of the radio-detected SMGs from Chapman et al. (2005), the faint 1.1-mm selected sub-mm galaxies in the ALMA UDF mosaic from Dunlop et al. (2016) and the lensed SPT SMGs from Weiß et al. (2013). Although the SMG samples presented here have selection functions that are difficult to quantify (especially the lensed sample of Weiß et al. 2013), they all peak at $z \sim 2$–3, and the those without radio pre-selection have significant (but not dominant) tails out to $z \sim 5$.

are either experiencing ongoing star formation over the previous > 100 Myr, or in post-starburst stellar populations, 0.3 − 1 Gyr after the strongest star formation has ended (Shapley 2011). In the Q = 1, 2 composite, the discontinuity is more consistent with the Balmer break than a 4000Å break, as the continuum at 3500 − 3600Å is $(1.5 \pm 0.1)\times$ lower than it is at 3900 − 4000Å.

To infer the age of the stellar populations within the ALESS SMGs, we use the SED templates from Bruzual & Charlot (2003) to predict the resultant spectra from a starburst of 100 Myr duration observed at 10 Myr, 100 Myr and 1 Gyr (post-starburst). We redden the model spectra using the reddening law from Calzetti et al. (2000) using the median extinction of $A_V = 2$ for the ALESS SMGs, as derived from SED fitting (see § 5.1.2). As Fig. 9 shows, the composite spectrum is indeed similar to an ongoing burst (i.e. undergoing star-formation on 10–100 Myr timescales), as expected for these strongly star-forming galaxies.

As well as stacking the spectra, we can also create a rest-frame broad-band SED. Simpson et al. (2014) and Swinbank et al. (2014) discuss the optical / near-infrared and far-infrared / radio photometry of the ALESS SMGs (see also da Cunha et al. 2015). By combining the multi-wavelength photometry with spectroscopic redshifts for 52 ALESS SMGs, we create composite SEDs from the rest-frame UV to radio wavelengths. First, we transform the photometry to the rest-frame, and then stack the photometry (normalised by rest-frame *H*-band luminosity; see §5.1.2). A running median is then calculated through the data to produce an average SED which we show in Fig. 9. We also overlay a HYPER-Z fit using a constant star formation history, which predicts (as expected) a heavily dust reddenned spectrum of these SMGs.

5.1.2. *UV-to-radio SEDs*

With a sample of spectroscopically confirmed SMGs with extensive UV-to-radio photometry, we exploit the MAGPHYS SED fitting code from (see da Cunha et al. 2015) to fit the UV-to-radio emission on a galaxy-by-galaxy basis to derive the dust reddenning, far-infrared luminosity and estimate the stellar mass for each SMG. Estimates of these parameters have been made using photometric redshifts, but the addition of spectroscopic redshifts removes some of the degeneracies between photometric redshift, reddenning and star formation histories, and in particular allows stellar masses to be estimated. The UV–mid-infrared photometry for the ALESS SMGs

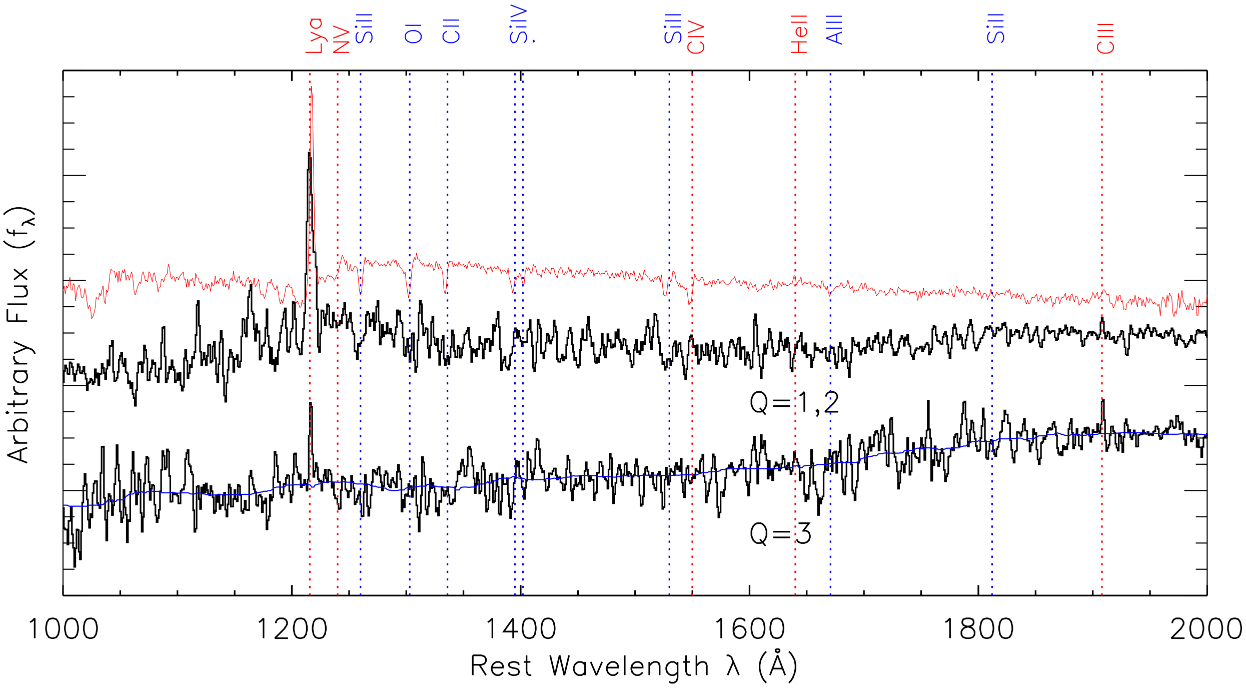

FIG. 8.— Composite spectra over the Lyman break (~ 1215Å). The spectra are summed and weighted by the noise. The top spectrum shows the stack of all the Q = 1 and 2 spectra. The composite spectrum of LBGs from Shapley et al. (2003) is overlaid in red (and offset for clarity). The Q = 3 stack was produced in order to broadly validate the Q = 3 redshifts and to identify additional features in the composite. The solid blue line is a running median of the Q = 3 composite. There are detections of both Lyα and CIII λ1909 in the composite.

is given in Simpson et al. (2014), whilst the (deblended) *Herschel* / SPIRE+PACS, ALMA and radio photometry are given in Swinbank et al. (2014) (see also da Cunha et al. 2015). For each SMG, we use MAGPHYS to fit the photometry at the spectroscopic redshift, and we show the best-fit SEDs (normalised by their $8-1000\mu$m luminosities) in Fig. 10 [20]. These normalised, rest-frame SEDs demonstrate a large spread in the UV- to optical-flux density which is dominated by the large spread in the dust attenuation. Indeed, the estimated range of extinctions vary from $A_V \sim 0.5$–7 magnitudes (see also da Cunha et al. 2015).

From the sample, we derive a median extinction of $A_V = 1.9 \pm 0.2$ and far infrared luminosity of $L_{FIR} = (3.2 \pm 0.4) \times 10^{12}\,L_\odot$, both of which are consistent with previous estimates (for the same sample) derived using photometric redshifts ($A_V = 1.7 \pm 0.2$ and $L_{FIR} = (3.5 \pm 0.4) \times 10^{12}\,L_\odot$ respectively). However, MAGPHYS also returns estimates of the stellar masses (solving for the star formation histories and ages) and we derive a median stellar mass for our 52 SMGs with spectroscopic redshifts of $M_\star = (6 \pm 1) \times 10^{10}\,M_\odot$, consistent with previous estimates (e.g. Hainline et al. 2011; da Cunha et al. 2015). This is consistent with the stellar masses estimates for the radio-selected SMGs in the Chapman et al. (2005) sample ($M_\star \sim 7 \times 10^{10}\,M_\odot$; Hainline et al. 2011). In Fig. 11 we plot the ALESS SMGs with spectroscopic redshifts on the stellar mass–star-formation rate plane. For comparison, we overlay the $z = 1.5$–2.5 star-forming galaxies from the multi-wavelength (UV–radio) study of BzK-selected galaxies by Rodighiero et al. (2014) (see also e.g. Elbaz et al. 2011). In this plot, we also overlay the median (and scatter) of the comparison sample as a function of stellar mass. From this plot, it is clear that the SMGs in our sample lie (on average) a factor ~5 above the so-called "main-sequence" at $z \sim 2$, with a median specific star formation rates (sSFR) of $sSFR = (6 \pm 1) \times 10^{-9}\,\mathrm{yr}^{-1}$ (see also e.g. Magnelli et al. 2012; Simpson et al. 2014)).

5.2. *Velocity offsets between emission / absorption lines*

Rest-frame UV optical spectroscopic analysis of high-redshift star forming galaxies have shown that redshifts derived from UV-ISM absorption lines typically display systematic blue-shifted offsets from the systemic (nebular) redshifts (e.g. Erb et al. 2006; Steidel et al. 2010; Martin et al. 2012), whilst redshifts determined from Lyα emission often show a systematic offset redward of the systemic. These velocity offsets are a consequence of large scale outflows (e.g. Pettini et al. 2002; Steidel et al. 2010), where the outflows material between the galaxy and the observer absorbs the UV and scatter Lyα photons from the receeding outflow, redshifting them with respect to the neutral medium within the galaxies. For some of the ALESS SMGs we are able to determine nebular, UV ISM and Lyα redshifts, allowing us to compare to the results for other star forming populations.

In Table 2 we summarise the lines detected for each ALESS SMG and the redshift associated with fitting to each line. We show the velocity offsets between the Lyα, UV-ISM and nebular emission lines in Fig. 12. We also overlay the velocity offsets for the SMGs studied by Chapman et al. (2005). Although the same trend is seen in the SMGs (Lyα is redshifted and the UV ISM lines are blueshifted with respect to the systemic red-

---

[21] The template SEDs are available from: http://astro.dur.ac.uk/~ams/zLESS/

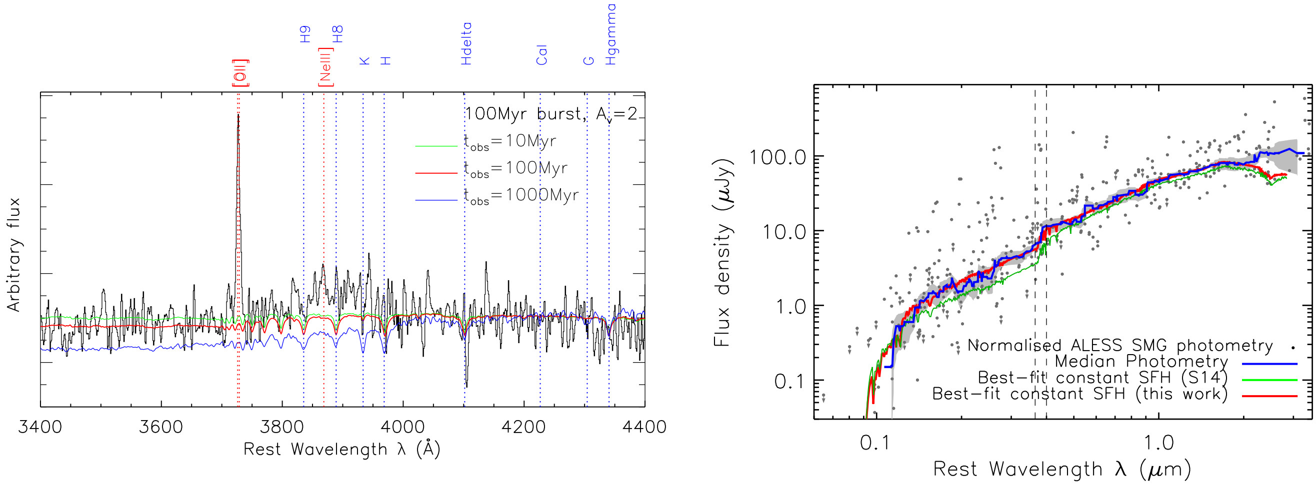

Fig. 9.— *Left:* The composite spectrum over restframe 3400 − 4400Å of the Q = 1 and 2 ALESS spectra with the spectra of X-ray AGN removed from the sample. The spectra were normalised by their median continuum flux between 2900 − 3600Å and sky-subtracted by the same method as in Fig. 8. 100 Myr starburst observed at 10, 100 and 1000 Myr. The model spectra with a 10 Myr burst provides the closest match to the strength of the Balmer break. *Right:* A composite SED using only the photometry from S14 for those ALESS SMGs with Q = 1, 2, 3 spectroscopic redshifts. The photometry for each sources has been de-redshifted and normalised by their *H*-band luminosity. The solid line represents the running median over 20 sources per box. The shaded region represents the bootstrap error on the running median. The red curve represents the best constant star formation history SED fit to the average photometry for all ALESS SMGs using HYPERZ and assuming a constant star formation rate, whereas the green curve is the constant star-formation history SED fit taken from S14. The de-redshifted photometry and limits are shown as grey points and arrows respectively. The vertical dashed lines are positioned at the Balmer (3646Å) and 4000Å breaks.

shift), the SMGs display significantly more scatter than LBGs, with velocity offsets ranging between ~ -1100 to $+700\,\mathrm{km\,s^{-1}}$ for the UV ISM-derived redshifts and between ~ -1500 to $+1200\,\mathrm{km\,s^{-1}}$ for the Lyα-derived redshifts, as compared to -600 to $+100\,\mathrm{km\,s^{-1}}$ and $\sim +100$ to $+900\,\mathrm{km\,s^{-1}}$ respectively for the LBGs in Steidel et al. (2010). In particular there is a significantly broader distribution in the velocity offsets of the ALESS SMGs, with Lyα being up to $+3000\,\mathrm{km\,s^{-1}}$ offset from the systemic redshift. The large spread in the velocity offsets may be due to a spread in the viewing angle of the winds or the presence of multiple components (Chen et al. 2015 demonstrate that most SMGs are major mergers and so the spectra may have contributions from merging components), or the diversity of conditions within these SMGs, in particular with regard to the strength of large-scale winds. Since the wind must be accelerated by star formation or AGN activity, in Fig. 12 we plot the velocity offsets between emission lines as a function of bolometric luminosity (we note that only two SMGs in our sample are X-ray AGN; Wang et al. 2013 and neither of these show Lyα and UV ISM lines with extreme offsets from the systemic redshift). Although there is significant scatter, the SMGs with lower bolometric luminosity tend to have wind velocities that are lower than those of the highest luminosity sources.

We note that the outliers in Fig. 12 are ALESS 088.5 and ALESS 049.1, with Lyα offset from the systemic velocity by $> 2000\,\mathrm{km\,s^{-1}}$. For both ALESS 088.5 and ALESS 049.1 the only line available to determine a nebular / systemic velocity was HeII λ1640, which, as we described previously can originate from the stellar winds from Wolf-Rayet stars, making it less reliable as a systemic velocity tracer than the typical nebular lines (i.e. Hα). It is important to note that the nebular lines such as Hα, [OIII] and [OII] may also be influenced by winds, however this is more typically observed as line broadening as opposed to centroid shifting.

5.3. *Environments*

Finally, in an attempt to understand the environments of SMG, we use the spectroscopic redshifts to search for physical associations between SMGs and between SMGs and the field galaxies. Various studies have investigated the environments of SMGs and demonstrated that SMGs commonly reside within overdense environments (e.g. Chapman et al. 2001; Blain et al. 2004; Chapman et al. 2009; Daddi et al. 2009; Capak et al. 2011; Walter et al. 2012; Ivison et al. 2013; Decarli et al. 2014; Smolcic et al. 2016). For example, Blain et al. (2004) (see also Chapman et al. 2009) identified an over-density of six SMGs and two radio galaxies at $z = 1.99$ within $1200\,\mathrm{km\,s^{-1}}$ of each other in the GOODS-N field. Clustering analysis has also suggested that SMGs cluster on scales of $(6.9 \pm 2.1)\,h^{-1}\,\mathrm{Mpc}^{-1}$ (e.g. Blain et al. 2004; Hickox et al. 2012; Chen et al. 2016; Wilkinson et al. 2016), while pair counting suggests SMGs have properties consistent with them evolving into the passive red galaxies at $z \sim 1$, and subsequently the members of rich galaxy groups or clusters at $z \sim 0$.

With our data, we can use a simple approach and exploit the spectroscopic redshifts to search for associations and structures in the ALESS SMG population. Karim et al. (2013) (see also Simpson et al. 2015b) demonstrate that single dish sub-mm sources suffer significant “multiplicity”, with $> 35\%$ of the single dish sources resolved into multiple SMGs (where an SMG is a far-infrared bright source with a 870μm flux brighter than 1 mJy). Simpson et al. (2015b) also demonstrate the number density of $S_{870} \gtrsim 2$ mJy SMGs in ALMA maps that target single-dish sub-mm sources is ~ 80 times higher than that derived from blank-field counts. An over-abundance of faint SMGs is inconsistent with line-of-sight projections dominating multiplicity in the brightest SMGs, and indi-

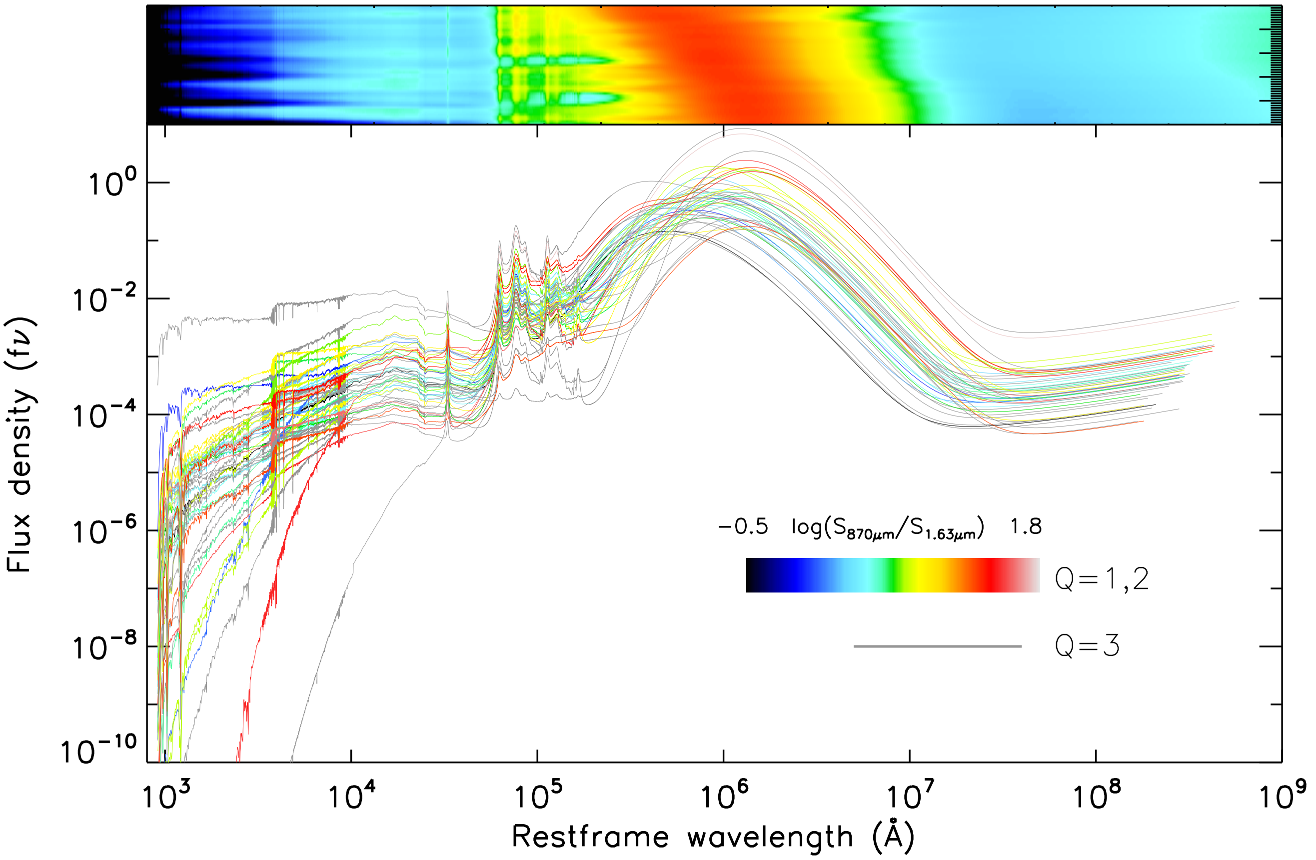

FIG. 10.— The best-fit rest-frame SEDs for each ALESS SMG with a spectroscopic redshift. These SEDs have been fitted using MAGPHYS (see da Cunha et al. 2008) and are normalised by their far-infrared ($8-1000\mu$m) luminosity. The coloured curves represent SEDs for SMGs with Q = 1 and 2 redshifts. They are colour-coded (purple to red) by the logarithm of their ratio of rest-frame $S_{870\mu m}/H$ flux density (with red denoting a higher ratio). Grey curves represent SEDs for SMGs with Q = 3 redshifts. There is a very large spread in the UV to optical flux density and hence a large spread in the attenuation. The colour scale in the upper image shows an image of the 52 SEDs, with the row they are positioned in ranked by their characteristic dust temperature.

cates that a significant proportion of these high-redshift ULIRGs are likely to be physically associated. These SMGs are typically separated by $\sim 6''$ which corresponds to $\sim$40–50 kpc if they lie at the same redshift.

First, we search for physical associations between SMGs in the same ALESS map (i.e. within $\sim 18''$) where the SMGs lie within 2000 km s^{-1} (although an offset of 2000 km s^{-1} is larger than the typical velocity dispersion of rich clusters; $<$ 1200 km s^{-1}; Blain et al. 2004 this is comparable to the random velocity offsets caused by emission from randomly-oriented galactic winds at high-redshift e.g. Erb et al. 2003). While there are only four ALESS maps in which we were able to determine a spectroscopic redshift for two or more of the SMGs (ALESS 017.1, 017.2; 067.1, 067.2; 075.1, 075.2; 088.1, 088.2; and 088.5, 088.11), only in one map do both SMGs (ALESS 067.1, ALESS 067.2) have redshifts which are within 2000 km s^{-1} - a clearly interacting pair in *HST* imaging (Chen et al. 2015). For the remaining three maps, the range of redshift offsets between these (previously blended) sources is $\Delta z = 0.25$–1.25.

Next, we search for physical associated between SMGs across the ECDFS (i.e. between the ALMA maps). We identify seven pairs of SMGs within 2000 km s^{-1} with ALESS 075.2, ALESS 088.5 and ALESS 102.1 also appearing as a triple "associations", with an average on-sky offset of ~4 Mpc in projection (with a range of ~2–15 Mpc). On these scales, the pairs (or triples) may lie within the same large-scale structure but are unlikely to lie within the same dark matter halos.

To determine whether these potential 'associations' correlate with redshift peaks in other background galaxy populations we compare the spectroscopic redshift distribution of the ALESS SMGs with that of the infill targets from our survey, as well as other galaxy populations in the ECDFS. Most of the spectroscopic redshifts for the other galaxy populations were taken from an extended version of a sample compiled in Luo et al. (2011) of $>$ 15,000 spectroscopic redshifts for galaxies in the ECDFS with a median redshift of $z \sim 0.670$ and an inter-quartile range of $z = 0.3$–1.0,[22]. From this catalog,

---

[22] http://www.eso.org/sci/activities/garching/projects/goods/MASTERCAT_v3.0.dat which includes redshifts from Cristiani et al. (2000); Croom et al. (2001); Bunker et al. (2003); Dickinson et al. (2004); Stanway et al. (2004a,b); Strolger et al. (2004); Szokoly et al. (2004); van der Wel et al. (2004); Le Fèvre et al. (2005); Doherty et al. (2005); Mignoli et al. (2005); Ravikumar

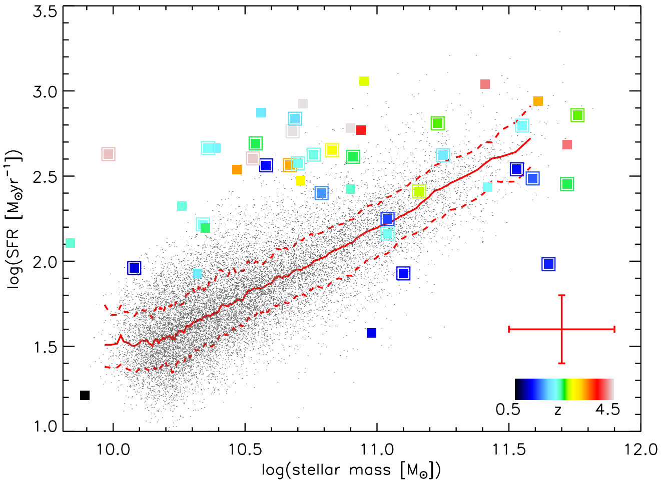

FIG. 11.— Stellar Mass–star-formation rate plane for ALESS SMGs with spectroscopic redshifts (large points) compared to star-forming galaxies at $z = 1.5$–2.5 in the COSMOS field (points) from the multi-wavelength (UV–radio) study by Rodighiero et al. (2014). The solid line denotes the running median (and central 68% of the distribution of the $z = 1.5$–2.5 Rodighiero et al. (2014) sample. The ALESS SMGs with the best spectroscopic redshifts (Q = 1 and Q = 2) are marked by double squares and the colour of the points are set by their spectroscopic redshift. This plot demonstrates that SMGs typically lie a factor of ∼ 5 (on average) above the so-called "main-sequence" at $z \sim 2$.

we select only secure redshifts and remove duplicates (we also remove cases in which two secure but differing redshifts are given from two different references).

In Fig. 13 we plot the spectroscopic redshift distribution of the ALESS SMGs, together with the field population. In the few cases where ≥ 2 SMGs lie within 2000 km s^{-1}, these associations do not often statistically coincide with significant over-densities in the background galaxy population, although the two SMGs at $z \sim 1.36$ are coincident with a peak in the radio / MIPS detections at that redshift.

6. CONCLUSIONS

In this work we present the results from a redshift survey of ALMA-identified SMGs. Our main conclusions are:

- The spectroscopic redshift distribution is centered at $z = 2.4 \pm 0.1$, but with a full range of $z = 0.7$-5.0 and an interquartile range of $z = 2.1$–3.0. This is consistent with the photometric redshift distribution for these sources, and the median is consistent with previous estimates based on the radio-detected SMGs (Chapman et al. 2005). However, since we do not require a radio selection, our sample is not biased to lower redshift and indeed, 23% of the ALESS SMGs lie at $z > 3$.

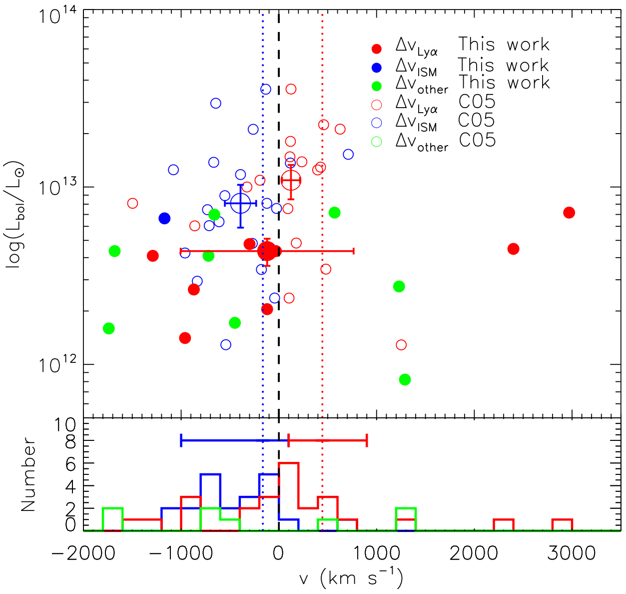

FIG. 12.— *Top:* Velocity offsets of the UV ISM absorption lines and Lyα from the systemic redshifts (shown as a dashed line) for all ALESS SMGs where multiple lines are detected versus the bolometric luminosity ($L_{8-1000\mu m}$). The green points represent the offsets between lines which can be either nebular or ISM lines and are frequently strongly influenced by winds, such as CIV λ1549, NV λ1240, CIII] λ1909, MgII λ2800 and HeII (if other nebular lines are available). Filled circles denote ALESS SMGs and open circles represent the the SMGs in Chapman et al. (2005). The median of each sample is shown as a larger symbol The red and blue dotted lines represent the mean of the distributions of Lyα and ISM velocity offsets respectively from the $z = 2$–3 LBG study from (Steidel et al. 2010) and the full range are shown as red and blue error bars on the bottom figure. We show a representative error bar for our data derived from the median error on the bolometric luminosity and we estimate a typical redshift measurement error of ∼100 km s^{-1} from fitting the spectral lines. *Bottom:* Histograms of the distributions of velocity offsets for Lyα (red), UV ISM lines (blue) and other lines (green). The histograms include the SMGs from ALESS and the Chapman et al. (2005) sample which demonstrates that Lyα and the UV ISM lines do indeed respectively peak redward and blueward of the systemic velocity.

- We identify velocity offsets up to ∼3000 km s^{-1} between the redshifts measured from nebular emission lines (i.e. Hα, [OIII], Hβ and [OII]) and those measured from Lyα or UV ISM absorption lines. We conclude that it is likely that the extreme SFRs within the SMGs (typically ∼ 300±30 M$_\odot$yr^{-1}) are driving strong galaxy-scale outflows in many of the SMGs.

- Since many of the spectra are too faint to exhibit any obvious emission or absorption features (continuum is only detected in ∼50% of the spectra), we produce composite spectra over various redshift ranges to search for interesting features in the 'typical' ALESS SMG optical-to-near infrared spectrum. Over 1000 – 2000Å we find strong asymmetric Lyα emission and blueshifted SiIV and CIV absorption indicative of strong stellar winds. Over 3400 – 4400Å we observe a strong Balmer break, indicative of ongoing star formation. Comparing our composite to various evolutionary models we find that it is most consistent with a young starburst of

---

et al. (2007); Vanzella, E. et al. (2008); Popesso et al. (2009); Balestra et al. (2010); Coppin et al. (2010); Silverman et al. (2010); Kurk et al. (2013); and redshifts also taken from Kriek et al. (2008); Boutsia et al. (2009); Taylor et al. (2009); Treister et al. (2009); Wuyts et al. (2009); Casey et al. (2011); Xia et al. (2011); Bonzini et al. (2012); Cooper et al. (2012); Coppin et al. (2012); Iwasawa et al. (2012); Mao et al. (2012); Le Fèvre et al. (2013); Georgantopoulos et al. (2013); De Breuck et al. (2014); Williams et al. (2014) and the 2df galaxy redshift survey (2dFGRS)

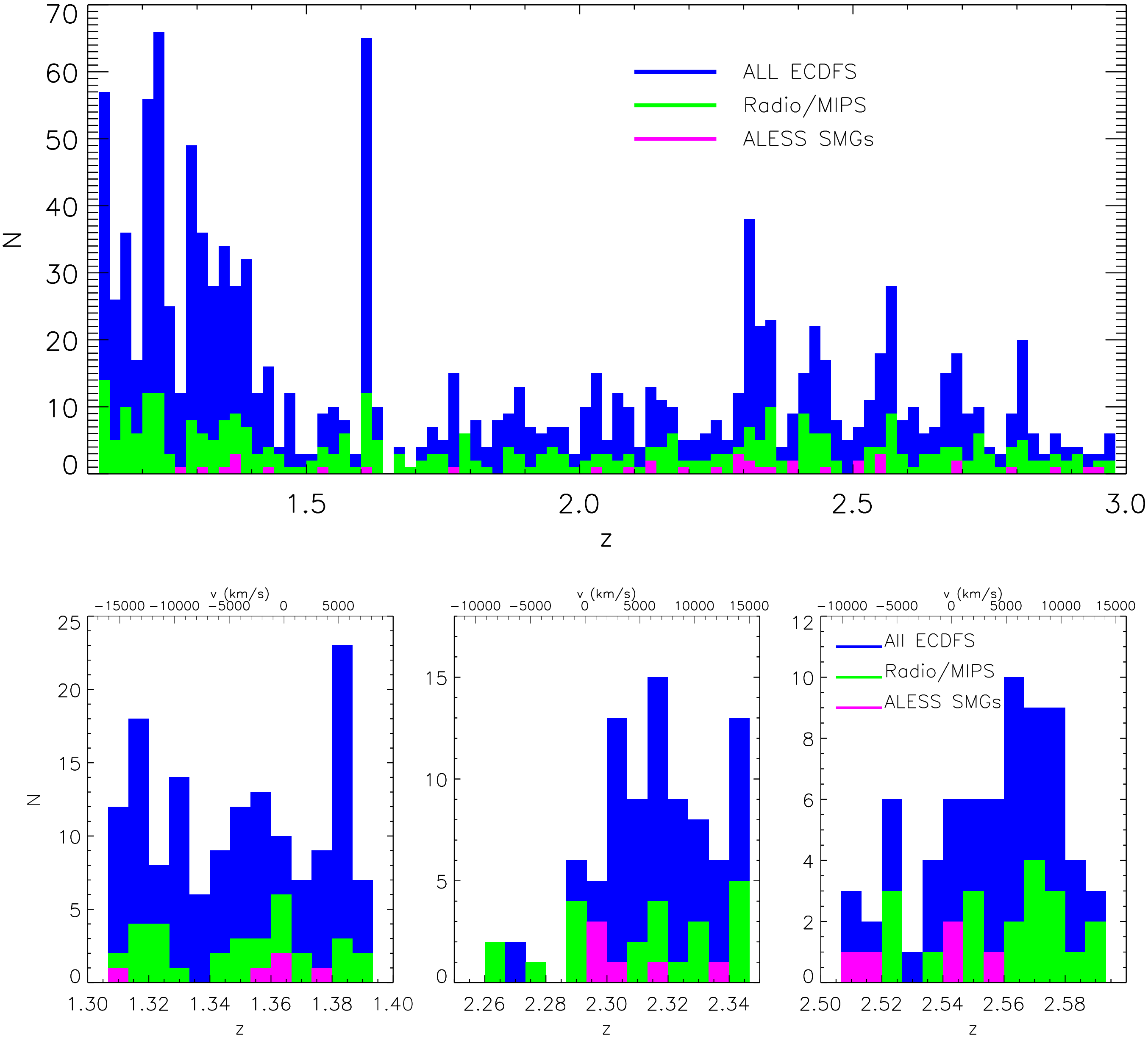

Fig. 13.— *Top:* The redshift distribution of Q = 1, 2 and 3 SMGs overlaid on the redshift distribution of field galaxies, compiled by Luo et al. with the addition of recent redshifts from the full FORS2/VIMOS survey (Table A1) and from Williams et al. (2014). The blue histogram represents all the galaxies in the ECDFS for which we have spectroscopic redshifts (including the SMGs). We show the radio/MIPS detected sources as well as the SMGs. The binning is 6000 $\mathrm{km\,s^{-1}}$. There is very little correlation between the peaks in the galaxy redshift distribution and the peaks in the SMG population. *Bottom:* A zoomed in view of the redshift associations in the ALESS SMG spectroscopic redshift distribution to search for coincidence with peaks in the overall galaxy redshift distribution. The colours are the same as Fig. 13. The maximum number of SMGs in a 2000 $\mathrm{km\,s^{-1}}$ bin is three and there are three other bins containing two SMGs. The top axis gives the velocity offsets, with 0 being set at the position of the redshift pair/triplet. The pairs/triplets in the SMG population do not obviously coincide with overdensities in other galaxy populations.

100 Myr duration observed at 10 Myr.

- We use the newly-derived redshifts as constraints in SED model fitting for each SMG using MAGPHYS and find a large spread in the dust attenuation (A_V ∼0.5–7 magnitudes) with a median $A_V = 1.7 \pm 0.2$. Using the spectroscopic redshifts and the extensive UV-to-radio photometry in this field, we produce optimised spectral energy distributions (SEDs) using MAGPHYS. We derive a median stellar mass for our SMGs with spectroscopic redshifts of $M_\star = (6 \pm 1) \times 10^{10}\,M_\odot$ and by combining with the star-formation rates, we show that SMGs lie (on average) ∼5 times above the so-called "main-sequence" at $z \sim 2$. We provide this library of 52 templates as a resource for future studies of SMGs.

This work has highlighted the difficulty of measuring spectroscopic redshifts at optical-to-near infrared wavelengths for dusty star-forming galaxies identified by ALMA, and thus demonstrates the importance of alternative methods of measuring redshifts such as mid-infrared spectroscopy (e.g. Valiante et al. 2007) and the increasing importance of blind submillimetre / millimetre spectral searches with ALMA (e.g. Weiß et al. 2013).

Neverthless, we find that the SMG population is a diverse population of dusty galaxies most common at $z \sim 2.4$, with strong evidence of energetic outflows which are likely to be predominantly driven by star formation but may have a contribution from AGN. The main goal of this study was to provide redshifts for subsequent studies such as CO gas studies or further detailed integral field unit (IFU) follow-up observations. Such studies will allow us to separate out the relative contributions of star formation and AGN, to probe the conditions within the star-forming gas to better understand this extreme and diverse population of galaxies.

ACKNOWLEDGMENTS

We acknowledge the ESO programmes 183.A-0666 and 090.A-0927(A). The ALMA observations were carried out under program 2011.0.00294.S. ALMA is a partnership of ESO (representing its member states), NSF (USA) and NINS (Japan), together with NRC (Canada) and NSC and ASIAA (Taiwan), in cooperation with the Republic of Chile. The Joint ALMA Observatory is operated by ESO, AUI/NRAO and NAOJ. ALRD acknowledges an STFC studentship (ST/F007299/1) and an STFC STEP award. AMS gratefully acknowledges an STFC Advanced Fellowship through grant ST/H005234/1, STFC grant ST/L00075X/1 and the Leverhume foundation. IRS acknowledges support from STFC, a Leverhulme Fellowship, the ERC Advanced Investigator programme DUSTYGAL 321334 and a Royal Society/Wolfson Merit Award. WNB acknowledges STScI grant HST-GO-12866.01-A. CMC acknowledges support from a McCue Fellowship at the University of California, Irvines Center for Cosmology and the University of Texas at Austins College of Natural Science. JLW is supported by a European Union COFUND/Durham Junior Research Fellowship under EU grant agreement number 267209. AK acknowledges support by the Collaborative Research Council 956, sub-project A1, funded by the Deutsche Forschungsgemeinschaft (DFG).

REFERENCES

Alexander, D. M., Brandt, W. N., Smail, I., Swinbank, A. M., Bauer, F. E., Blain, A. W., Chapman, S. C., & Coppin et al. 2008, AJ, 135, 1968

Alexander, D. M., Swinbank, A. M., Smail, I., McDermid, R., & Nesvadba, N. P. H. 2010, MNRAS, 402, 2211

Balestra, I., Mainieri, V., Popesso, P., Dickinson, M., Nonino, M., Rosati, P., Teimoorinia, H., Vanzella, E., Cristiani, S., Cesarsky, C., Fosbury, R. A. E., Kuntschner, H., & Rettura, A. 2010, A&A, 512, A12

Barger, A. J., Wang, W.-H., Cowie, L. L., Owen, F. N., Chen, C.-C., & Williams, J. P. 2012, ApJ, 761, 89

Baugh, C. M., Lacey, C. G., Frenk, C. S., Granato, G. L., Silva, L., Bressan, A., Benson, A. J., & Cole, S. 2005, MNRAS, 356, 1191

Béthermin, M., De Breuck, C., Sargent, M., & Daddi, E. 2015, A&A, 576, L9

Biggs, A. D., Ivison, R. J., Ibar, E., Wardlow, J. L., Dannerbauer, H., Smail, I., Walter, F., & Weiß, A. et al. 2011, MNRAS, 413, 2314

Blain, A. W., Chapman, S. C., Smail, I., & Ivison, R. 2004, ApJ, 611, 725

Bonzini, M., Mainieri, V., Padovani, P., Kellermann, K. I., Miller, N., Rosati, P., Tozzi, P., Vattakunnel, S., Balestra, I., Brandt, W. N., Luo, B., & Xue, Y. Q. 2012, ApJS, 203, 15

Bothwell, M. S., Smail, I., Chapman, S. C., Genzel, R., Ivison, R. J., Tacconi, L. J., Alaghband-Zadeh, S., & Bertoldi, F. et al. 2013, MNRAS, 429, 3047

Boutsia, K., Leibundgut, B., Trevese, D., & Vagnetti, F. 2009, A&A, 497, 81

Bruzual, G. & Charlot, S. 2003, MNRAS, 344, 1000

Bunker, A. J., Stanway, E. R., Ellis, R. S., McMahon, R. G., & McCarthy, P. J. 2003, MNRAS, 342, L47

Calzetti, D., Armus, L., Bohlin, R. C., Kinney, A. L., Koornneef, J., & Storchi-Bergmann, T. 2000, ApJ, 533, 682

Capak, P. L., Riechers, D., Scoville, N. Z., Carilli, C., Cox, P., Neri, R., Robertson, B., Salvato, M., Schinnerer, E., Yan, L., Wilson, G. W., Yun, M., Civano, F., Elvis, M., Karim, A., Mobasher, B., & Staguhn, J. G. 2011, Nature, 470, 233

Casey, C. M., Berta, S., Béthermin, M., Bock, J., Bridge, C., Budynkiewicz, J., Burgarella, D., & Chapin, E. et al. 2012, ApJ, 761, 140

Casey, C. M., Chapman, S. C., Smail, I., Alaghband-Zadeh, S., Bothwell, M. S., & Swinbank, A. M. 2011, MNRAS, 411, 2739

Casey, C. M., Narayanan, D., & Cooray, A. 2014, ArXiv e-prints

Chabrier, G. 2003, PASP, 115, 763

Chapman, S. C., Blain, A., Ibata, R., Ivison, R. J., Smail, I., & Morrison, G. 2009, ApJ, 691, 560

Chapman, S. C., Blain, A. W., Smail, I., & Ivison, R. J. 2005, ApJ, 622, 772

Chapman, S. C., Richards, E. A., Lewis, G. F., Wilson, G., & Barger, A. J. 2001, ApJL, 548, L147

Chen, C.-C., Smail, I., Ivison, R. J., Arumugam, V., Almaini, O., Conselice, C. J., Geach, J. E., & Hartley, W. G. e al. 2016, ApJ, 820, 82

Chen, C.-C., Smail, I., Swinbank, A. M., Simpson, J. M., Ma, C.-J., Alexander, D. M., Biggs, A. D., & Brandt, W. N. e. a. 2015, ApJ, 799, 194

Cooper, M. C., Newman, J. A., Davis, M., Finkbeiner, D. P., & Gerke, B. F. 2012, spec2d: DEEP2 DEIMOS Spectral Pipeline, Astrophysics Source Code Library

Coppin, K. E. K., Chapman, S. C., Smail, I., Swinbank, A. M., Walter, F., Wardlow, J. L., Weiss, A., & Alexander, D. M. et al. 2010, MNRAS, 407, L103

Coppin, K. E. K., Danielson, A. L. R., Geach, J. E., Hodge, J. A., Swinbank, A. M., Wardlow, J. L., Bertoldi, F., & Biggs, A. et al. 2012, MNRAS, 427, 520

Coppin, K. E. K., Smail, I., Alexander, D. M., Weiss, A., Walter, F., Swinbank, A. M., Greve, T. R., Kovacs, A., & De Breuck, C. et al. 2009, MNRAS, 395, 1905

Cristiani, S., Appenzeller, I., Arnouts, S., Nonino, M., Aragón-Salamanca, A., Benoist, C., da Costa, L., Dennefeld, M., Rengelink, R., Renzini, A., Szeifert, T., & White, S. 2000, A&A, 359, 489

Croom, S. M., Shanks, T., Boyle, B. J., Smith, R. J., Miller, L., Loaring, N. S., & Hoyle, F. 2001, MNRAS, 325, 483

da Cunha, E., Charlot, S., & Elbaz, D. 2008, MNRAS, 388, 1595

da Cunha, E., Walter, F., Smail, I. R., Swinbank, A. M., Simpson, J. M., Decarli, R., Hodge, J. A., Weiss, A., van der Werf, P. P., Bertoldi, F., Chapman, S. C., Cox, P., Danielson, A. L. R., Dannerbauer, H., Greve, T. R., Ivison, R. J., Karim, A., & Thomson, A. 2015, ApJ, 806, 110

Daddi, E., Dannerbauer, H., Krips, M., Walter, F., Dickinson, M., Elbaz, D., & Morrison, G. E. 2009, ApJL, 695, L176

Davé, R., Finlator, K., Oppenheimer, B. D., Fardal, M., Katz, N., Kereš, D., & Weinberg, D. H. 2010, MNRAS, 404, 1355

De Breuck, C., Williams, R. J., Swinbank, M., Caselli, P., Coppin, K., Davis, T. A., Maiolino, R., & Nagao, T. et al. 2014, A&A, 565, A59

Decarli, R., Walter, F., Carilli, C., Riechers, D., Cox, P., Neri, R., Aravena, M., & Bell, E. et al. 2014, ApJ, 782, 78

Dickinson, M., Stern, D., Giavalisco, M., Ferguson, H. C., Tsvetanov, Z., Chornock, R., Cristiani, S., & Dawson, S. et al. 2004, ApJL, 600, L99

Doherty, M., Bunker, A. J., Ellis, R. S., & McCarthy, P. J. 2005, MNRAS, 361, 525

Efstathiou, A. & Rowan-Robinson, M. 2003, MNRAS, 343, 322

Elbaz, D., Dickinson, M., Hwang, H. S., Díaz-Santos, T., Magdis, G., Magnelli, B., Le Borgne, D., & Galliano, F. et al. 2011, A&A, 533, A119

Erb, D. K., Shapley, A. E., Steidel, C. C., Pettini, M., Adelberger, K. L., Hunt, M. P., Moorwood, A. F. M., & Cuby, J. 2003, ApJ, 591, 101

Erb, D. K., Steidel, C. C., Shapley, A. E., Pettini, M., Reddy, N. A., & Adelberger, K. L. 2006, ApJ, 647, 128

Genzel, R., Baker, A. J., Tacconi, L. J., Lutz, D., Cox, P., Guilloteau, S., & Omont, A. 2003, ApJ, 584, 633

Georgantopoulos, I., Comastri, A., Vignali, C., Ranalli, P., Rovilos, E., Iwasawa, K., Gilli, R., & Cappelluti, N. et al. 2013, A&A, 555, A43

Hainline, L. J., Blain, A. W., Smail, I., Alexander, D. M., Armus, L., Chapman, S. C., & Ivison, R. J. 2011, ApJ, 740, 96

Hainline, L. J., Blain, A. W., Smail, I., Frayer, D. T., Chapman, S. C., Ivison, R. J., & Alexander, D. M. 2009, ApJ, 699, 1610

Harrison, C. M., Alexander, D. M., Swinbank, A. M., Smail, I., Alaghband-Zadeh, S., Bauer, F. E., Chapman, S. C., Del Moro, A., Hickox, R. C., Ivison, R. J., Menéndez-Delmestre, K., Mullaney, J. R., & Nesvadba, N. P. H. 2012, MNRAS, 426, 1073

Hayward, C. C., Kereš, D., Jonsson, P., Narayanan, D., Cox, T. J., & Hernquist, L. 2011, ApJ, 743, 159

Hickox, R. C., Wardlow, J. L., Smail, I., Myers, A. D., Alexander, D. M., Swinbank, A. M., Danielson, A. L. R., & Stott, J. P. et al. 2012, MNRAS, 421, 284

Hodge, J. A., Karim, A., Smail, I., Swinbank, A. M., Walter, F., Biggs, A. D., Ivison, R. J., & Weiss, A. et al. 2013, ApJ, 768, 91

Huynh, M. T., Norris, R. P., Coppin, K. E. K., Emonts, B. H. C., Ivison, R. J., Seymour, N., Smail, I., Smolčić, V., Swinbank, A. M., Brandt, W. N., Chapman, S. C., Dannerbauer, H., De Breuck, C., Greve, T. R., Hodge, J. A., Karim, A., Knudsen, K. K., Menten, K. M., van der Werf, P. P., Walter, F., & Weiss, A. 2013, MNRAS, 431, L88

Ikarashi, S., Ivison, R. J., Caputi, K. I., Aretxaga, I., Dunlop, J. S., Hatsukade, B., Hughes, D. H., & Iono, D. et al. 2015, ApJ, 810, 133

Ivison, R. J., Greve, T. R., Dunlop, J. S., Peacock, J. A., Egami, E., Smail, I., & Ibar et al. 2007, MNRAS, 380, 199

Ivison, R. J., Smail, I., Dunlop, J. S., Greve, T. R., Swinbank, A. M., Stevens, J. A., Mortier, A. M. J., & Serjeant et al. 2005, MNRAS, 364, 1025

Ivison, R. J., Swinbank, A. M., Smail, I., Harris, A. I., Bussmann, R. S., Cooray, A., Cox, P., & Fu, H. et al. 2013, ApJ, 772, 137

Iwasawa, K., Gilli, R., Vignali, C., Comastri, A., Brandt, W. N., Ranalli, P., Vito, F., & Cappelluti, N. et al. 2012, A&A, 546, A84

Karim, A., Swinbank, A. M., Hodge, J. A., Smail, I. R., Walter, F., Biggs, A. D., Simpson, J. M., & Danielson, A. L. R. et al. 2013, MNRAS, 432, 2

Kelson, D. D. 2003, PASP, 115, 688

Kennicutt, R. C. 1998, ARAA, 36, 189

Kriek, M., van Dokkum, P. G., Franx, M., Illingworth, G. D., Marchesini, D., Quadri, R., Rudnick, G., & Taylor, E. N. et al. 2008, ApJ, 677, 219

Kurk, J., Cimatti, A., Daddi, E., Mignoli, M., Pozzetti, L., Dickinson, M., Bolzonella, M., Zamorani, G., Cassata, P., Rodighiero, G., Franceschini, A., Renzini, A., Rosati, P., Halliday, C., & Berta, S. 2013, A&A, 549, A63

Lacey, C. G., Baugh, C. M., Frenk, C. S., Benson, A. J., Bower, R. G., Cole, S., Gonzalez-Perez, V., Helly, J. C., Lagos, C. D. P., & Mitchell, P. D. 2015, ArXiv e-prints

Le Fèvre, O., Cassata, P., Cucciati, O., Garilli, B., Ilbert, O., Le Brun, V., Maccagni, D., & Moreau, C. et al. 2013, A&A, 559, A14

Le Fèvre, O., Vettolani, G., Garilli, B., Tresse, L., Bottini, D., Le Brun, V., Maccagni, D., & Picat, J. P. et al. 2005, A&A, 439, 845

Lehmer, B. D., Brandt, W. N., Alexander, D. M., Bauer, F. E., Schneider, D. P., Tozzi, P., Bergeron, J., & Garmire, G. P. et al. 2005, ApJS, 161, 21

Leitherer, C. & Heckman, T. M. 1995, ApJS, 96, 9

Lilly, S. J., Eales, S. A., Gear, W. K. P., Hammer, F., Le Fèvre, O., Crampton, D., Bond, J. R., & Dunne, L. 1999, ApJ, 518, 641

Luo, B., Bauer, F. E., Brandt, W. N., Alexander, D. M., Lehmer, B. D., Schneider, D. P., Brusa, M., & Comastri et al., A. 2008, ApJS, 179, 19

Luo, B., Brandt, W. N., Xue, Y. Q., Alexander, D. M., Brusa, M., Bauer, F. E., Comastri, A., Fabian, A. C., Gilli, R., Lehmer, B. D., Rafferty, D. A., Schneider, D. P., & Vignali, C. 2011, ApJ, 740, 37

Lutz, D., Poglitsch, A., Altieri, B., Andreani, P., Aussel, H., Berta, S., Bongiovanni, A., & Brisbin D. et al. 2011, A&A, 532, A90

Magnelli, B., Elbaz, D., Chary, R. R., Dickinson, M., Le Borgne, D., Frayer, D. T., & Willmer, C. N. A. 2009, A&A, 496, 57

Magnelli, B., Lutz, D., Santini, P., Saintonge, A., Berta, S., Albrecht, M., Altieri, B., & Andreani, P. et al. 2012, A&A, 539, A155

Mao, M. Y., Sharp, R., Norris, R. P., Hopkins, A. M., Seymour, N., Lovell, J. E. J., Middelberg, E., Randall, K. E., Sadler, E. M., Saikia, D. J., Shabala, S. S., & Zinn, P.-C. 2012, MNRAS, 426, 3334

Martin, C. L., Shapley, A. E., Coil, A. L., Kornei, K. A., Bundy, K., Weiner, B. J., Noeske, K. G., & Schiminovich, D. 2012, ApJ, 760, 127

Mignoli, M., Cimatti, A., Zamorani, G., Pozzetti, L., Daddi, E., Renzini, A., Broadhurst, T., Cristiani, S., D'Odorico, S., Fontana, A., Giallongo, E., Gilmozzi, R., Menci, N., & Saracco, P. 2005, A&A, 437, 883

Narayanan, D., Cox, T. J., Hayward, C. C., Younger, J. D., & Hernquist, L. 2009, MNRAS, 400, 1919

Newman, J. A., Cooper, M. C., Davis, M., Faber, S. M., Coil, A. L., Guhathakurta, P., Koo, D. C., & Phillips, A. C. et al. 2013, ApJS, 208, 5

Oliver, S. J., Bock, J., Altieri, B., Amblard, A., Arumugam, V., Aussel, H., Babbedge, T., & Beelen, A. et al. 2012, MNRAS, 424, 1614

Pettini, M., Rix, S. A., Steidel, C. C., Adelberger, K. L., Hunt, M. P., & Shapley, A. E. 2002, ApJ, 569, 742

Popesso, P., Dickinson, M., Nonino, M., Vanzella, E., Daddi, E., Fosbury, R. A. E., Kuntschner, H., Mainieri, V., Cristiani, S., Cesarsky, C., Giavalisco, M., Renzini, A., & GOODS Team. 2009, A&A, 494, 443

Ravikumar, C. D., Puech, M., Flores, H., Proust, D., Hammer, F., Lehnert, M., Rawat, A., & Amram, P. et al. 2007, A&A, 465, 1099

Rodighiero, G., Renzini, A., Daddi, E., Baronchelli, I., Berta, S., Cresci, G., Franceschini, A., & Gruppioni, C. et al. 2014, MNRAS, 443, 19

Rousselot, P., Lidman, C., Cuby, J.-G., Moreels, G., & Monnet, G. 2000, A&A, 354, 1134

Serjeant, S., Farrah, D., Geach, J., Takagi, T., Verma, A., Kaviani, A., & Fox, M. 2003, MNRAS, 346, L51

Shapley, A. E. 2011, ARAA, 49, 525

Shapley, A. E., Steidel, C. C., Pettini, M., & Adelberger, K. L. 2003, ApJ, 588, 65
Silverman, J. D., Mainieri, V., Salvato, M., Hasinger, G., Bergeron, J., Capak, P., Szokoly, G., & Finoguenov, A. et al. 2010, ApJS, 191, 124
Simpson, J. M., Smail, I., Swinbank, A. M., Almaini, O., Blain, A. W., Bremer, M. N., Chapman, S. C., & Chen, C.-C. 2015a, ApJ, 799, 81
Simpson, J. M., Smail, I., Swinbank, A. M., Chapman, S. C., Geach, J. E., Ivison, R. J., Thomson, A. P., & Aretxaga, I. et al. 2015b, ApJ, 807, 128
Simpson, J. M., Swinbank, A. M., Smail, I., Alexander, D. M., Brandt, W. N., Bertoldi, F., de Breuck, C., & Chapman, S. C. 2014, ApJ, 788, 125
Smail, I., Chapman, S. C., Blain, A. W., & Ivison, R. J. 2004, ApJ, 616, 71
Smolcic, V., Miettinen, O., Tomicic, N., Zamorani, G., Finoguenov, A., Lemaux, B. C., Aravena, M., & Capak, P. et al. 2016, ArXiv e-prints
Spergel, D. N., Verde, L., Peiris, H. V., Komatsu, E., Nolta, M. R., Bennett, C. L., Halpern, M., & Hinshaw, G., et al. 2003, ApJS, 148, 175
Stanway, E. R., Bunker, A. J., McMahon, R. G., Ellis, R. S., Treu, T., & McCarthy, P. J. 2004a, ApJ, 607, 704
Stanway, E. R., Glazebrook, K., Bunker, A. J., Abraham, R. G., Hook, I., Rhoads, J., McCarthy, P. J., Boyle, B., Colless, M., Crampton, D., Couch, W., Jørgensen, I., Malhotra, S., Murowinski, R., Roth, K., Savaglio, S., & Tsvetanov, Z. 2004b, ApJL, 604, L13
Steidel, C. C., Erb, D. K., Shapley, A. E., Pettini, M., Reddy, N., Bogosavljević, M., Rudie, G. C., & Rakic, O. 2010, ApJ, 717, 289
Strandet, M. L., Weiss, A., Vieira, J. D., de Breuck, C., Aguirre, J. E., Aravena, M., Ashby, M. L. N., & Béthermin, M. et al. 2016, ApJ, 822, 80
Strolger, L.-G., Riess, A. G., Dahlen, T., Livio, M., Panagia, N., Challis, P., Tonry, J. L., & Filippenko, A. V. et al. 2004, ApJ, 613, 200
Swinbank, A. M., Chapman, S. C., Smail, I., Lindner, C., Borys, C., Blain, A. W., Ivison, R. J., & Lewis, G. F. 2006, MNRAS, 371, 465
Swinbank, A. M., Karim, A., Smail, I., Hodge, J., Walter, F., Bertoldi, F., Biggs, A. D., & de Breuck, C. et al. 2012, MNRAS, 427, 1066
Swinbank, A. M., Lacey, C. G., Smail, I., Baugh, C. M., Frenk, C. S., Blain, A. W., Chapman, S. C., & Coppin et al. 2008, MNRAS, 391, 420
Swinbank, A. M., Simpson, J. M., Smail, I., Harrison, C. M., Hodge, J. A., Karim, A., Walter, F., & Alexander, D. M. et al. 2014, MNRAS, 438, 1267
Szokoly, G. P., Bergeron, J., Hasinger, G., Lehmann, I., Kewley, L., Mainieri, V., Nonino, M., Rosati, P., Giacconi, R., Gilli, R., Gilmozzi, R., Norman, C., Romaniello, M., Schreier, E., Tozzi, P., Wang, J. X., Zheng, W., & Zirm, A. 2004, ApJS, 155, 271
Tacconi, L. J., Genzel, R., Smail, I., Neri, R., Chapman, S. C., Ivison, R. J., Blain, A., & Cox, P., et al. 2008, ApJ, 680, 246
Taylor, E. N., Franx, M., van Dokkum, P. G., Quadri, R. F., Gawiser, E., Bell, E. F., Barrientos, L. F., & Blanc, G. A. et a. 2009, ApJS, 183, 295
Toft, S., Smolčić, V., Magnelli, B., Karim, A., Zirm, A., Michalowski, M., Capak, P., & Sheth, K. et al. 2014, ApJ, 782, 68
Treister, E., Virani, S., Gawiser, E., Urry, C. M., Lira, P., Francke, H., Blanc, G. A., Cardamone, C. N., Damen, M., Taylor, E. N., & Schawinski, K. 2009, ApJ, 693, 1713
Valiante, E., Lutz, D., Sturm, E., Genzel, R., Tacconi, L. J., Lehnert, M. D., & Baker, A. J. 2007, ApJ, 660, 1060
van der Wel, A., Franx, M., van Dokkum, P. G., & Rix, H.-W. 2004, ApJL, 601, L5
Vanzella, E. et al. 2008, A&A, 478, 83
Walter, F., Decarli, R., Carilli, C., Bertoldi, F., Cox, P., da Cunha, E., Daddi, E., & Dickinson, M. et al. 2012, Nature, 486, 233
Wang, S. X., Brandt, W. N., Luo, B., Smail, I., Alexander, D. M., Danielson, A. L. R., Hodge, J. A., Karim, A., Lehmer, B. D., Simpson, J. M., Swinbank, A. M., Walter, F., Wardlow, J. L., Xue, Y. Q., Chapman, S. C., Coppin, K. E. K., Dannerbauer, H., De Breuck, C., Menten, K. M., & van der Werf, P. 2013, ApJ, 778, 179
Wardlow, J. L., Smail, I., Coppin, K. E. K., Alexander, D. M., Brandt, W. N., Danielson, A. L. R., Luo, B., & Swinbank, A. M. et al. 2011, MNRAS, 415, 1479
Weiß, A., De Breuck, C., Marrone, D. P., Vieira, J. D., Aguirre, J. E., Aird, K. A., Aravena, M., & Ashby, M. L. N. et al. 2013, ApJ, 767, 88
Weiß, A., Kovács, A., Coppin, K., Greve, T. R., Walter, F., Smail, I., Dunlop, J. S., & Knudsen, K. K. et al. 2009, ApJ, 707, 1201
Wilkinson, A., Almaini, O., Chen, C.-C., Smail, I., Arumugam, V., Blain, A., Chapin, E. L., & Chapman, S. C. et al. 2016, ArXiv e-prints
Williams, R. J., Maiolino, R., Santini, P., Marconi, A., Cresci, G., Mannucci, F., & Lutz, D. 2014, MNRAS, 443, 3780
Wuyts, S., van Dokkum, P. G., Franx, M., Förster Schreiber, N. M., Illingworth, G. D., Labbé, I., & Rudnick, G. 2009, ApJ, 706, 885
Xia, L., Malhotra, S., Rhoads, J., Pirzkal, N., Zheng, Z., Meurer, G., Straughn, A., Grogin, N., & Floyd, D. 2011, AJ, 141, 64

APPENDIX

Table 2: ALESS spectroscopic redshift catalog

ALESS ID	RA (J2000)	DEC (J2000)	z_{spec}	Q_{spec}	$z_{\rm phot}$[a]	M/S[b]	Instruments[c]	Notes
ALESS 001.1	53.310270	-27.937366	4.9540	3	$4.34^{+2.66}_{-1.43}$	M	GMX	[OII] in M-K
ALESS 001.2	53.310059	-27.936562	...	4	$4.65^{+2.34}_{-1.02}$	M	FVX	BLANK
ALESS 001.3	53.309069	-27.936759	...	4	$2.85^{+0.20}_{-0.30}$	M	X	BLANK
ALESS 002.1	53.261188	-27.945211	2.1913	3	$1.96^{+0.27}_{-0.20}$	M	DV	poss. CIII] em in D
ALESS 002.2	53.262800	-27.945252	...	4	-	M	D	BLANK
ALESS 003.1	53.339603	-27.922304	4.2373	3	$3.90^{+0.50}_{-0.59}$	M	FMV	poss. Lyα em in F+V
ALESS 003.2	*53.342461*	*-27.922486*	*...*	*4*	$1.44^{+0.43}_{-0.38}$	*S*	*M*	*BLANK*
ALESS 003.3	*53.336294*	*-27.920555*	*...*	*4*	-	*S*	*M*	*BLANK*
ALESS 003.4	*53.341644*	*-27.919379*	*...*	*4*	-	*S*	*M*	*BLANK*
ALESS 005.1	52.870467	-27.985840	...	4	$2.86^{+0.05}_{-0.04}$	M	DMX	BLANK
ALESS 006.1	53.237331	-28.016856	2.3338	1	$0.45^{+0.06}_{-0.04}$	M	GX	cont. from bright sources above SMG; Lyα em ($z = 2.3295$) and CIV em ($z = 2.3314$) in X-UVB; Hα and [OIII]5007 in G ($z = 2.3338$)
ALESS 007.1	53.314242	-27.756750	2.6923	1	$2.50^{+0.12}_{-0.16}$	M	DFXS	strong cont.; z from Hα in X-NIR; HeII in X-VIS ($z = 2.6901$)
ALESS 007.2	*53.312522*	*-27.758499*	*...*	*4*	-	*S*	*D*	*BLANK*
ALESS 009.1	53.047244	-27.869981	...	4	$4.50^{+0.54}_{-2.33}$	M	D	BLANK
ALESS 010.1	53.079418	-27.870781	0.7616	1	$2.02^{+0.09}_{-0.09}$	M	FV	[OII] in V; [OII] ($z = 0.7613$), [OIII]4959 ($z = 0.7619$), Hβ ($z = 0.7617$) in F; z is mean from [OII], [OIII], Hβ, possible lens
ALESS 011.1	53.057688	-27.933403	2.6832	2	$2.83^{+1.88}_{-0.50}$	M	FV	Lyα em in V, no cont.
ALESS 013.1	53.204132	-27.714389	...	4	$3.25^{+0.64}_{-0.46}$	M	DG	BLANK
ALESS 014.1	52.968716	-28.055300	...	4	$4.47^{+2.54}_{-0.88}$	M	VX	BLANK
ALESS 015.1	53.389034	-27.991547	...	4	$1.93^{+0.62}_{-0.33}$	M	DFGVX	BLANK
ALESS 015.2	*53.391876*	*-27.991724*	*...*	*4*	-	*S*	*M*	*BLANK*
ALESS 015.3	53.389976	-27.993176	3.4252	3	-	M	DM	Lyα em ($z = 3.4399$) and CIV em ($z = 3.4106$) in D
ALESS 015.6	*53.388192*	*-27.995048*	*...*	*4*	-	*S*	*M*	*BLANK*
ALESS 017.1	53.030410	-27.855765	1.5397	1	$1.51^{+0.10}_{-0.07}$	M	DFMV	strong cont.; z from Hα in M-H; MgII abs in F ($z = 1.5382$)
ALESS 017.2	*53.034437*	*-27.855470*	*2.4431*	*3*	$2.10^{+0.65}_{-1.37}$	*S*	*M*	*poss. Hα in M-K*
ALESS 017.3	*53.030718*	*-27.859423*	*...*	*4*	$2.58^{+0.16}_{-0.32}$	*S*	*D*	*BLANK*
ALESS 018.1	53.020343	-27.779927	2.2520[d]	1	$2.04^{+0.10}_{-0.06}$	M	V	cont. in V; archival z from Casey+11
ALESS 019.1	53.034401	-27.970609	...	4	$2.41^{+0.17}_{-0.11}$	M	FV	BLANK
ALESS 020.1	*53.319834*	*-28.004431*	*...*	*4*	$2.58^{+0.16}_{-0.32}$	*S*	*DFV*	*cont. in F*
ALESS 020.2	*53.317807*	*-28.006470*	*...*	*4*	-	*S*	*D*	*BLANK*
ALESS 022.1	52.945494	-27.544250	...	4	$1.88^{+0.18}_{-0.23}$	M	FV	cont. in F+V
ALESS 023.1	53.050039	-28.085128	...	4	$4.99^{+2.01}_{-2.55}$	M	V	BLANK
ALESS 025.1	52.986997	-27.994259	2.8719	3	$2.24^{+0.07}_{-0.17}$	M	V	Lyα + break, cont.
ALESS 029.1	53.403749	-27.969259	1.438 9	2	$2.66^{+2.94}_{-0.76}$	M	DGMV	Hα in M-H
ALESS 031.1	52.957448	-27.961322	...	4	$2.89^{+1.80}_{-0.41}$	M	FVX	BLANK
ALESS 034.1	*53.074833*	*-27.875910*	*2.5115*	*2*	$1.87^{+0.29}_{-0.32}$	*S*	*M*	*broad Hα in M-K*
ALESS 035.1	52.793776	-27.620948	...	4	-	M	V	BLANK
ALESS 037.2	53.401514	-27.896742	2.3824	3	$4.87^{+0.22}_{-0.40}$	M	M	Hα ($z = 2.3824$) and [SII] ($z = 2.3831$)
ALESS 038.1	*53.295153*	*-27.944501*	*...*	*4*	$2.47^{+0.11}_{-0.05}$	*S*	*D*	*strong cont.+emission lines from contaminating source*
ALESS 039.1	52.937629	-27.576871	...	4	$2.44^{+0.17}_{-0.23}$	M	X	poss. faint lines, no cont.
ALESS 041.1	52.791959	-27.876850	2.5460	2	$2.75^{+4.25}_{-0.72}$	M	FV	strong cont. in F+V; CIII]1909 em ($z = 2.5459$), CII]2326 em ($z = 2.5500$) in F; cont. break in V
ALESS 041.3	52.792927	-27.878001	...	4	-	M	M	weak cont.
ALESS 043.1	53.277670	-27.800677	...	4	$1.71^{+0.20}_{-0.12}$	M	DFV	possible faint lines, no cont.
ALESS 043.3	*53.276120*	*-27.798534*	*...*	*4*	-	*S*	*D*	*BLANK*
ALESS 045.1	53.105255	-27.875148	...	4	$2.34^{+0.26}_{-0.67}$	M	FV	no cont.; poss. Lyα em $z = 2.9690$ from V and CIV $z = 2.9867$ from F
ALESS 046.1	*53.402937*	*-27.547072*	*...*	*4*	-	*S*	*FV*	*faint cont. in F*
ALESS 049.1	52.852998	-27.846406	2.9417	2	$2.76^{+0.11}_{-0.14}$	M	DFV	strong cont. in F + V; HeII em ($z = 2.9417$), CIV em ($z = 2.9436$),

Continued from previous page

ALESS ID	RA (J2000)	DEC (J2000)	z_{spec}	Q_{spec}	$z^{a}_{\rm phot}$	M/S[b]	Instruments[c]	Notes
ALESS 049.2	52.851956	-27.843914	...	4	$1.47^{+0.07}_{-0.10}$	M	M	BLANK
ALESS 051.1	52.937754	-27.740922	1.3638	3	$1.22^{+0.03}_{-0.06}$	M	FV	strong cont. in F+V, [OII] ($z = 1.3638$) and break ∼ 8000Å and poss. MgII em ($z = 1.3681$) in F
ALESS 055.1	53.259242	-27.676513	1.3564	2	$2.05^{+0.15}_{-0.13}$	M	DF	strong cont. in F+D; MgIIem ($z = 1.3556$) and H+K abs. (Kabs. $z = 1.3572$) in F
ALESS 055.2	53.258983	-27.678148	...	4	-	M	D	BLANK
ALESS 057.1	52.966348	-27.890850	2.9369[d]	1	$2.95^{+0.05}_{-0.10}$	M	FV	cont. + Lyα em ($z = 2.9387$), CIV em ($z = 2.9332$), HeII em ($z = 2.9388$) in V
ALESS 059.2	53.265897	-27.738390	...	4	$2.09^{+0.78}_{-0.29}$	M	X	BLANK
ALESS 061.1	53.191128	-28.006490	4.4190	1	$6.52^{+0.36}_{-0.34}$	M	A	ALMA [CII]158μm
ALESS 062.1	*53.150677*	*-27.580258*	*...*	*4*	-	*S*	*D*	*BLANK*
ALESS 062.2	*53.152410*	*-27.581619*	*1.3614*	*1*	$1.35^{+0.08}_{-0.11}$	*S*	*DFV*	*[OII] in D+F*
ALESS 063.1	53.285193	-28.012179	...	4	$1.87^{+0.10}_{-0.33}$	M	G	poss. faint em lines
ALESS 065.1	53.217771	-27.590630	4.4445	1	-	M	AD	z from ALMA [CII158]μm, Lyα
ALESS 066.1	53.383053	-27.902645	2.5542	1	$2.33^{+0.05}_{-0.04}$	M	FMV	Hα and [NII] in M; lensed?
ALESS 067.1	53.179981	-27.920649	2.1230[d]	1	$2.14^{+0.05}_{-0.09}$	M	FVX	cont. in F+V; Hα, [OIII]5007 in X-NIR; merging with 067.2
ALESS 067.2	53.179253	-27.920749	2.1230	3	$2.05^{+0.15}_{-0.13}$	M	X	BLANK but likely merging with 067.1
ALESS 068.1	53.138888	-27.653770	...	4	-	M	VX	BLANK
ALESS 069.1	52.890731	-27.992345	4.2071	3	$2.34^{+0.27}_{-0.44}$	M	D	single line, poss. Lyα with asymmetric profile
ALESS 069.2	52.892226	-27.991361	...	4	-	M	M	BLANK
ALESS 069.3	52.891524	-27.993990	...	4	-	M	DM	BLANK
ALESS 070.1	52.933425	-27.643200	2.0918	3	$2.28^{+0.05}_{-0.06}$	M	FX	strong cont. in F; poss. Lyα in X-UVB
ALESS 071.1	53.273528	-27.557831	3.6967	2	$2.48^{+0.21}_{-0.11}$	M	V	Lyα ($z = 3.7006$); very bright line; NV em ($z = 3.6927$)
ALESS 072.1	53.168322	-27.632807	...	4	-	M	DX	poss. faint lines, no cont.
ALESS 073.1	53.122046	-27.938807	4.7649[d]	1	$5.18^{+0.43}_{-0.45}$	M	DF	very broad Lyα and NV em in D+F; Lyα ($z = 4.7648$), NV ($z = 4.7649$)
ALESS 074.1	53.288112	-27.804774	...	4	$1.80^{+0.13}_{-0.13}$	M	DFV	BLANK
ALESS 075.1	52.863303	-27.930928	2.5450	1	$2.39^{+0.08}_{-0.06}$	M	FVX	very interesting source; strong cont. in V+F; [OIII]4959 ($z = 2.5452$), [OIII]5007 ($z = 2.5447$) broad red components to [OIII], Hβ ($z = 2.5451$), [OII] doublet ($z = 2.5446$), Hα ($z = 2.5452$), Lyα in X ($z = 2.5440$)
ALESS 075.2	*52.865276*	*-27.933116*	*2.2944*	*2*	$0.39^{+0.02}_{-0.03}$	*S*	*DM*	*Hα, [NII]* ($z = 2.2941$)*, [SII]* ($z = 2.2886$) *in M-K*
ALESS 075.4	52.860715	-27.932144	...	4	$2.10^{+0.29}_{-0.34}$	M	DM	BLANK
ALESS 076.1	53.384731	-27.998786	3.3895	2	-	M	DFMV	[OIII]5007 + [OIII]4959 in M; poss. Lyα ($z \sim 3.3984$) in V
ALESS 079.1	53.088064	-27.940830	...	4	$2.04^{+0.63}_{-0.31}$	M	D	BLANK
ALESS 079.2	53.090004	-27.939988	1.7693	1	$1.55^{+0.11}_{-0.18}$	M	FVX	Strong Hα, [NII]6548, 6583 in X-NIR; structured lines- 2 components
ALESS 079.4	53.088261	-27.941808	...	4	-	M	D	BLANK
ALESS 080.1	52.928347	-27.810244	4.6649	3	$1.96^{+0.16}_{-0.14}$	M	FV	poss Lyα in F
ALESS 080.2	52.927570	-27.811376	...	4	$1.37^{+0.17}_{-0.08}$	M	D	BLANK
ALESS 080.5	*52.923654*	*-27.806318*	*1.3078*	*3*	-	*S*	*D*	*tentative [OII] + [NeIII]*
ALESS 081.1	*52.864805*	*-27.744336*	*...*	*4*	$1.70^{+0.29}_{-0.20}$	*S*	*V*	*BLANK*
ALESS 082.1	53.224989	-27.637470	...	4	$2.10^{+3.27}_{-0.44}$	M	DFV	BLANK
ALESS 084.1	52.977090	-27.851568	3.9651	3	$1.92^{+0.09}_{-0.07}$	M	DFM	Lyα ($z = 3.9639$), NV ($z = 3.9672$) in F; cont. in F
ALESS 084.2	52.974388	-27.851207	...	4	$1.75^{+0.08}_{-0.19}$	M	DF	cont. in F; poss faint lines
ALESS 087.1	53.212016	-27.528187	2.3086	1	$3.20^{+0.08}_{-0.47}$	M	FV	Lyα em ($z = 2.3188$), SiIV abs ($z = 2.3050$), SiII abs ($z = 2.3019$) in V; Lyα offset from cont.
ALESS 088.1	52.978175	-27.894858	1.2679	1	$1.84^{+0.12}_{-0.11}$	M	FVMX	[OII] ($z = 1.2679$); [OII]3726,3729 visible in X-VIS
ALESS 088.2	52.980797	-27.894529	2.5192	3	-	M	DM	CII]2326 em ($z = 2.5227$), CIV em ($z = 2.5156$) in D
ALESS 088.5	52.982524	-27.896446	2.2941	2	$2.30^{+0.11}_{-0.50}$	M	DFV	strong cont. in V, poss break; Lyα em ($z = 2.3021$), HeII ($z = 2.2941$) in V
ALESS 088.11	52.978949	-27.893785	2.3583	3	$2.57^{+0.04}_{-0.12}$	M	D	CIII] em ($z = 2.3585$), Lyα em ($z = 2.3581$) + break
ALESS 089.1	*53.202879*	*-28.006079*	*0.6830*	*3*	$1.17^{+0.06}_{-0.15}$	*S*	*F*	*bright [OII] + cont*

Continued from previous page

ALESS ID	RA (J2000)	DEC (J2000)	z_{spec}	Q_{spec}	$z^{a}_{\rm phot}$	M/S[b]	Instruments[c]	Notes
ALESS 094.1	53.281640	-27.968281	...	4	$2.87^{+0.37}_{-0.64}$	M	DV	BLANK
ALESS 098.1	52.874654	-27.956317	1.3745[d]	1	$1.63^{+0.17}_{-0.09}$	M	DFMVX	[OII] ($z = 1.3745$) brightest in F; cont. in M and F, real Hα under sky in X-NIR
ALESS 099.1	53.215910	-27.925996	...	4	-	M	D	BLANK
ALESS 101.1	*52.964987*	*-27.764718*	*2.7999*	*2*	$3.49^{+03.52}_{-0.88}$	*S*	*V*	*Lyα*
ALESS 102.1	53.398333	-27.673061	2.2960	3	$1.76^{+0.16}_{-0.18}$	M	FV	cont. in V, Lyα ($z = 2.2931$), CIII] ($z = 2.2960$) in V
ALESS 106.1	*52.915187*	*-27.944236*	...	*4*	$7.00^{+0.00}_{-4.07}$	*S*	*DM*	*BLANK*
ALESS 107.1	52.877082	-27.863647	2.9965	3	$3.75^{+0.09}_{-0.08}$	M	VM	Lyα em ($z = 2.9757$), CIV em ($z = 2.9965$) in V; cont. in V+M; poss. [OII], [OIII] in M
ALESS 107.3	52.878013	-27.865465	...	4	$2.12^{+1.54}_{-0.81}$	M	D	BLANK
ALESS 110.1	52.844411	-27.904784	...	4	$2.55^{+0.70}_{-0.50}$	M	FMV	BLANK
ALESS 110.5	52.845677	-27.904005	...	4	-	M	DM	BLANK
ALESS 112.1	53.203596	-27.520362	2.3154	1	$1.95^{+0.15}_{-0.26}$	M	FGV	Lyα em ($z = 2.3122$) + cont. in V , Hα ($z = 2.3145$), poss [OIII]5007 ($z = 2.3157$), Hβ em ($z = 2.3160$) in G
ALESS 114.2	52.962945	-27.743693	1.6070	1	$1.56^{+0.07}_{-0.07}$	M	FV	strong cont in F+V, [OII] doublet in F ($z = 1.6070$)
ALESS 115.1	53.457070	-27.709609	3.3631	3	-	M	V	cont., poss Lyα em ($z = 3.3631$)
ALESS 116.1	52.976342	-27.758039	...	4	$3.54^{+1.47}_{-0.87}$	M	FV	BLANK
ALESS 116.2	52.976826	-27.758735	...	4	$4.02^{+1.19}_{-2.19}$	M	F	BLANK
ALESS 118.1	52.841347	-27.828161	2.3984	3	$2.26^{+0.50}_{-0.23}$	M	DFV	strong cont in F+V, Lyα abs + break, CIV em ($z = 2.3984$) in V
ALESS 119.1	53.235993	-28.056988	...	4	$3.50^{+0.95}_{-0.35}$	M	V	BLANK
ALESS 122.1	52.914768	-27.688792	2.0232[d]	1	$2.06^{+0.05}_{-0.06}$	M	FV	very strong blue cont. and abs. lines. V: CII] abs ($z = 2.0197$), SiIV abs ($z = 2.0229$), HeII em ($z = 2.0282$), Very broad CIV and SiII blended abs.; CIII] ($z = 2.0222$). F: FeII 2344, FeII 2375, FeII 2383 abs
ALESS 124.1	53.016843	-27.601769	...	4	$6.07^{+0.94}_{-1.16}$	M	FV	poss faint lines
ALESS 126.1	53.040033	-27.685466	...	4	$1.82^{+0.28}_{-0.08}$	M	V	BLANK

TABLE 2

NOTES: THE 22 ALESS SMGS NOT TARGETED IN OUR SPECTROSCOPY PROGRAMME (AND WITHOUT REDSHIFTS FROM LITERATURE) ARE NOT LISTED HERE. THE SUPP SMGS ARE SHOWN IN ITALICS. $z_{spec} = -99$ MEANS WE COULD NOT DETERMINE A SPECTROSCOPIC REDSHIFT. [a]PHOTOMETRIC REDSHIFTS FROM S14. THOSE SMGS WITHOUT A PHOTOMETRIC REDSHIFT HAVE POOR PHOTOMETRIC CONSTRAINTS (DETECTIONS IN < 4 BANDS). [b]M = MAIN CATALOG, S = SUPP CATALOG. [c]F = VLT/FORS2, V = VLT/VIMOS, X = VLT/XSHOOTER, M = KECK/MOSFIRE (BAND H OR K), D = KECK/DEIMOS, G = GEMINI/GNIRS. [d]THESE REDSHIFTS ARE FOR THE SIX SOURCES WHICH ALSO HAVE LITERATURE SPECTROSCOPIC REDSHIFTS DESCRIBED IN § 3. THE QUALITY FLAG (Q) FOR THE SPECTROSCOPIC REDSHIFTS IS Q = 1 FOR SECURE REDSHIFTS; Q = 2 FOR REDSHIFTS MEASURED FROM ONLY ONE OR TWO STRONG LINES; Q = 3 FOR TENTATIVE REDSHIFTS MEASURED BASED ON ONE OR TWO VERY FAINT FEATURES; Q = 4 FOR THOSE SOURCES WHICH WERE TARGETED BUT NO REDSHIFT COULD BE DETERMINED.

ALESS SMGS WITH LITERATURE REDSHIFTS

The following sources are ALESS SMGs with previously measured spectroscopic redshifts:

1. ALESS 018.1: listed as ID 66 in Casey et al. (2011), with a redshift of $z = 2.252$ derived from an Hα detection with the Infrared Spectrometer And Array Camera (ISAAC) on the VLT;
2. ALESS 057.1: listed as ID 112a in Szokoly et al. (2004) with a redshift of $z = 2.940$ derived from detections of HeII, OVI and NV with FORS1 / FORS2. It is classed as a QSO with strong high-ionisation emission lines;
3. ALESS 067.1: listed as ECDFS-45 in Kriek et al. (2008) with a redshift of $z = 2.122$, derived from emission lines in the near-infrared spectra observed with GNIRS;
4. ALESS 073.1: listed as GDS J033229.29−275619.5 in the Vanzella, E. et al. (2008) collection of 1019 spectroscopic redshifts for GOODS / CDFS. The redshift of $z = 4.762$ was determined via the detection of Lyα and NV using FORS2.
5. ALESS 098.1: listed as ID J033129 in Casey et al. (2011). The redshift, $z = 1.4982$ is derived through a tentative detection of Hα, however, it is also spectroscopically-identified in the restframe UV in the same paper and therefore it is given a 'secure' status. This redshift is, however, in disagreement with our Q = 1 redshift of $z = 1.3735$ derived from fitting to an [OII] detection in the FORS2 observations, with a tentative detection of Hα at the same redshift under a sky line in the XSHOOTER near-infrared spectrum. We use our redshift in the analysis in this work;
6. ALESS 122.1: listed as radio ID 149 in Bonzini et al. (2012). The redshift of $z = 2.03$ is determined from UV ISM absorption features observed with VIMOS.

NOTABLE INDIVIDUAL SOURCES

Since we have a wealth of spectroscopic data we can utilise the spectra not only for the purpose of determining redshifts but also to search for diagnostic features indicative of AGN activity, star-formation, strong stellar winds etc. Here we highlight and discuss some of the most notable, high signal-to-noise spectra.

ALESS 057.1: This SMG hosts a luminous AGN, as identified in X-rays (Wang et al. 2013). The VIMOS spectrum (Fig. 2) exhibits strong, broad, symmetric Lyα emission, broad NV and CIV emission (FWHM$\sim$ 3700 km s^{-1}) which is significantly blue-shifted ($\sim$ 1600 km s^{-1}) with respect to both the detection of HeII and Lyα (which have velocities that are consistent within measurements errors). The CIV emission line also displays a P-Cygni profile with excess emission towards the blue and absorption towards high velocities.

ALESS 066.1: This SMG is listed as an X-ray AGN at $z = 1.310$ in Wang et al. (2013). However, our MOSFIRE observations reveal the photometry and X-ray emission are dominated by a foreground QSO at $z = 1.310$ but the identification of Hα in K-band at $\lambda = 2.333\mu$m reveals that the SMG lies at $z = 2.5542$. Careful analysis of the ALMA and optical imaging reveals that the SMG is likely to suffer lensing by the foreground QSO which is offset by $\lesssim 1''$ south of the 870μm position.

ALESS 073.1: This SMG also hosts an luminous X-ray AGN (Vanzella, E. et al. 2008; Coppin et al. 2009; De Breuck et al. 2014; Wang et al. 2013) and the spectra (Fig. 2) shows strong, broad NV with a FWHM$\sim$ 3000 km s^{-1} as compared to a relatively narrow and weak Lyα (FWHM$\sim$ 700 km s^{-1}).

ALESS 075.1: We have excellent spectroscopic coverage of this SMG and have strong detections of [OII], [OIII]λ4959, 5007, Hβ and Hα with XSHOOTER. The Hα detection is narrow with FWHM$\sim$160 km s^{-1}. The [OIII] emission is not fit well with a single Gaussian as it is an asymmetric line with a red wing, possibly indicating an outflow (e.g. Alexander et al. 2010). The red wing seen in the [OIII] is indicative of winds which, given the high [OIII] luminosity and the lack of an X-ray detection, may be accelerated by an obscured AGN (i.e. outflows in high-redshift ULIRGs hosting AGN activity; Harrison et al. 2012).

ALESS 079.2: This SMG has strong detections of Hα and [NII] with XSHOOTER. The one- and two-dimensional spectra show structured emission (see Fig. 14). In the one-dimensional spectrum the Hα and [NII] lines are truncated at their red end and appear to be more extended towards lower velocities. The flux ratio of [NII]λ6583/Hα is consistent with the ionising radiation arising from HII regions as opposed to an AGN.

ALESS 087.1: Strong continuum is detected in this SMG with UV-ISM absorption lines consistent with the Lyα emission derived redshift, however, the Lyα is significantly offset northwards of the continuum in the two-dimensional spectrum. We thus produce two one-dimensional spectra in Fig. 14 taken from the position of the Lyα and the continuum. The Lyα profile is marginally asymmetric with a truncated blue edge. The continuum spectrum shows an obvious break and relatively strong SiIV absorption. Unfortunately, there is very poor photometric coverage of this SMG (3.6–8μm only) so although the offset Lyα may be due to a close companion or an interaction with another system, or a less-obscured part of a single galaxy.

ALESS 122.1: This SMG has very blue continuum with strong UV ISM absorption lines in both the FORS2 and VIMOS spectra which are shown in Fig. 14. There is very strong, broad CIV absorption (FWHM of $>$ 7000 km s^{-1}). The CIV exhibits a strong, narrow component associated with the interstellar absorption and a very broad red component

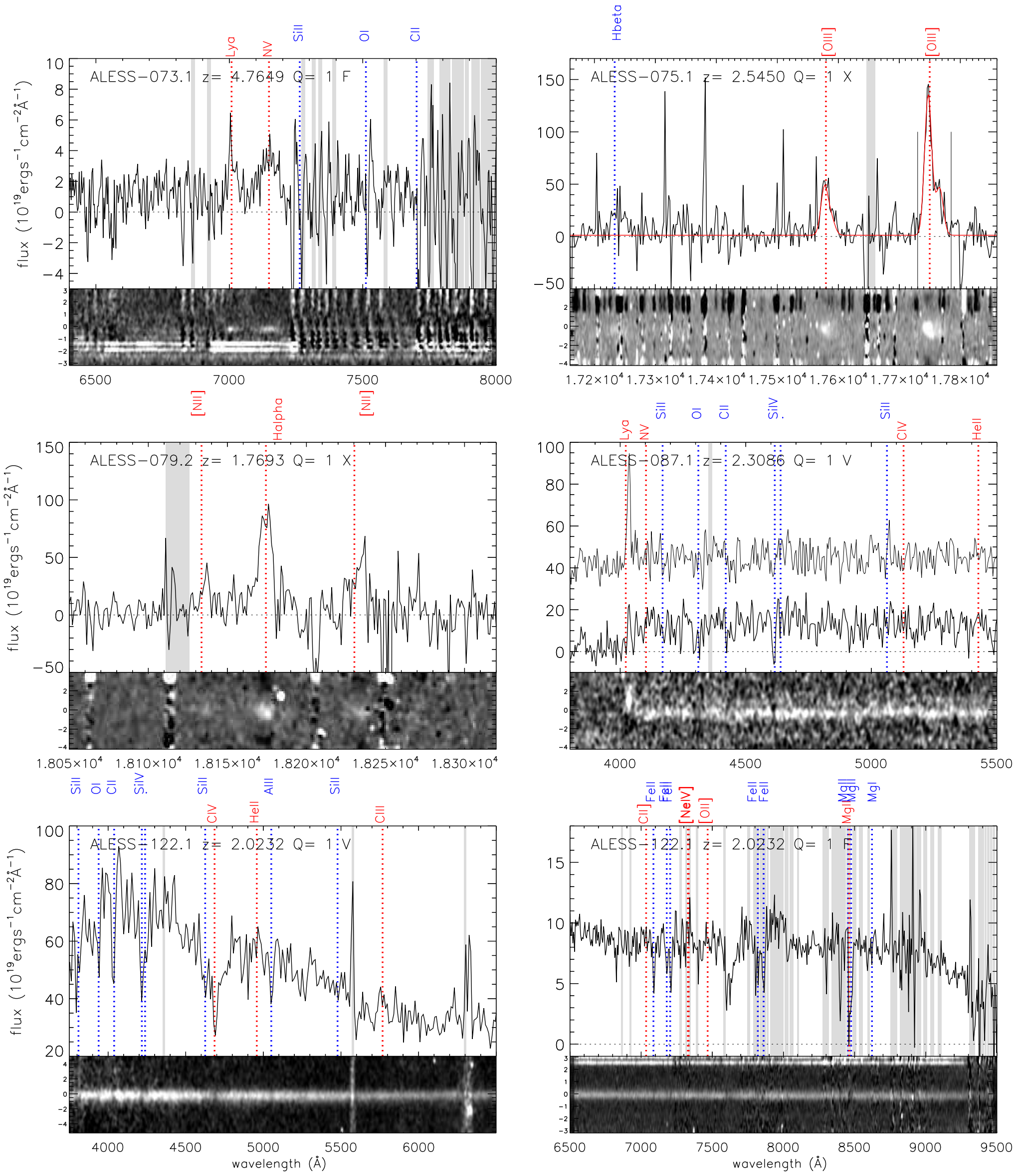

Fig. 14.— Some of the most notable spectra of SMGs in the sample, featuring evidence of winds, AGN activity, and multiple components. The sky subtraction is poor in some of the spectra and is a particular problem in the NIR and in the FORS2 spectrum of ALESS 073.1. The main skylines have been highlighted in grey.

associated with stellar winds. The strength of this redshifted component indicates the presence of a large number of very massive stars ($> 30\,M_\odot$; Leitherer & Heckman 1995). The SiIV, however, is relatively weak for continuous star formation but transforms into a strong P-Cygni profile for bursty star formation. Detection of a P-Cygni profile for SiIV is therefore a strong indicator that the burst duration is short relative to the burst age. The SiIV absorption feature is unusually broad ($> 3000\,\mathrm{km\,s^{-1}}$) in particular in the bluer line. This is the blueshifted wind absorption. The SiIV profile is qualitatively most similar to the line profiles expected for a very recent instantaneous burst of star formation with the intensity of the absorption implying the presence of massive stars. Swinbank et al. (2014) determine $L_{\rm FIR} = (6.0\pm0.4)\times10^{12}\,L_\odot$ for this SMG which implies a star formation rate (SFR) of SFR $\sim 1040\pm70\,M_\odot\mathrm{yr}^{-1}$ (using Kennicutt 1998) which is particularly high compared to the median for the ALESS SMGs of SFR$\sim$ $(310\pm30)\,M_\odot\mathrm{yr}^{-1}$ (Swinbank et al. 2014). We note that an AGN may also exhibit strong CIV absorption and given the very strong continuum and the large width of the CIV in this SMG, it is plausible that it may be a broad absorption line (BAL) QSO.

ANCILLARY REDSHIFTS

When designing the slit masks, we in-filled the slit masks with other candidate high-redshift galaxies, in particular with mid-, far-infrared or radio selected galaxies. Here, we provide the redshifts for the galaxies targeted.

The ID for each galaxy relates to the input catalog from which a target was selected. These are summarised as:
101–500: Statistically Robust or Tentative candidate LESS SMG counterparts from Wardlow et al. (2011) and Biggs et al. (2011) but which were later shown by ALMA to be incorrect IDs (Hodge et al. 2013).

500–700: Robust or tentative IDs for LESS sources with signal-to-noise of SNR = 2.7–3.7σ in the original LESS map. These IDs for "faint SMGs" are derived using 1.4 GHz radio emission (Biggs et al. 2011) but have not yet been confirmed (or ruled out) by ALMA.

700–1000: Galaxies in the LESS error circles which have photometric redshifts that are consistent with the ALESS photometric redshifts (Wardlow et al. 2011).

1000–3000: 24+70μm-selected galaxies from the *Spitzer* FIDEL survey without pre-existing spectroscopic redshifts (Magnelli et al. 2009).

4000–4300: Chandra X-ray sources from the 2 Ms or 4 Ms surveys (e.g. Lehmer et al. 2005; Luo et al. 2008).

50000-51000: Optically faint radio galaxies (OFRGs) from the JVLA 1.4 GHz survey of this field. These radio sources are typically brighter than $>20\,\mu$Jy at 1.4 GHz but have optical magnitudes fainter than $I_{\rm AB} = 22$.

70000–72000: Optically (colour) selected galaxies. These comprise a mix of $z \sim 2$ Lymanα emitting galaxies, BM/BX galaxies and Lyman break galaxies at $1.5 < z < 3.5$.

90000-90200: B- or V-band drop-out galaxies (i.e. candidate $z \gtrsim 2.5$ or $z \gtrsim 3.5$ galaxies).

>80000: Galaxies which were not in any of the other catalogs but which could still be placed on the masks.

Any source that is labelled with a *"b"* suffix denotes a secondary galaxy that happened to lie on the slit, but is not the primary target.

We also note that the catalogs are not unique (a galaxy could be an ALMA source that is also in the FIDEL 24μm catalog, a radio catalog, a BX/BM and also a Chandra source). In those instances, the object will only appear once in the table, but under the ID from which it was selected for slit placement (i.e. there are no RA / Dec repeats). As in Table A1, the instrument IDs are denoted by F = VLT / FORS2, V = VLT / VIMOS, X = VLT / XSHOOTER, M = Keck / MOSFIRE, D = Keck /, DEIMOS, and G = Gemini / GNIRS. The quality flag (Q) for the spectroscopic redshifts is Q = 1 for secure redshifts; Q = 2 for redshifts measured from only one or two strong lines; Q = 3 for tentative redshifts measured based on one or two very faint features; Q = 4 for those sources which were targeted but no redshift could be determined. The redshift distribution for each of these sub-samples is shown in Fig. 15.

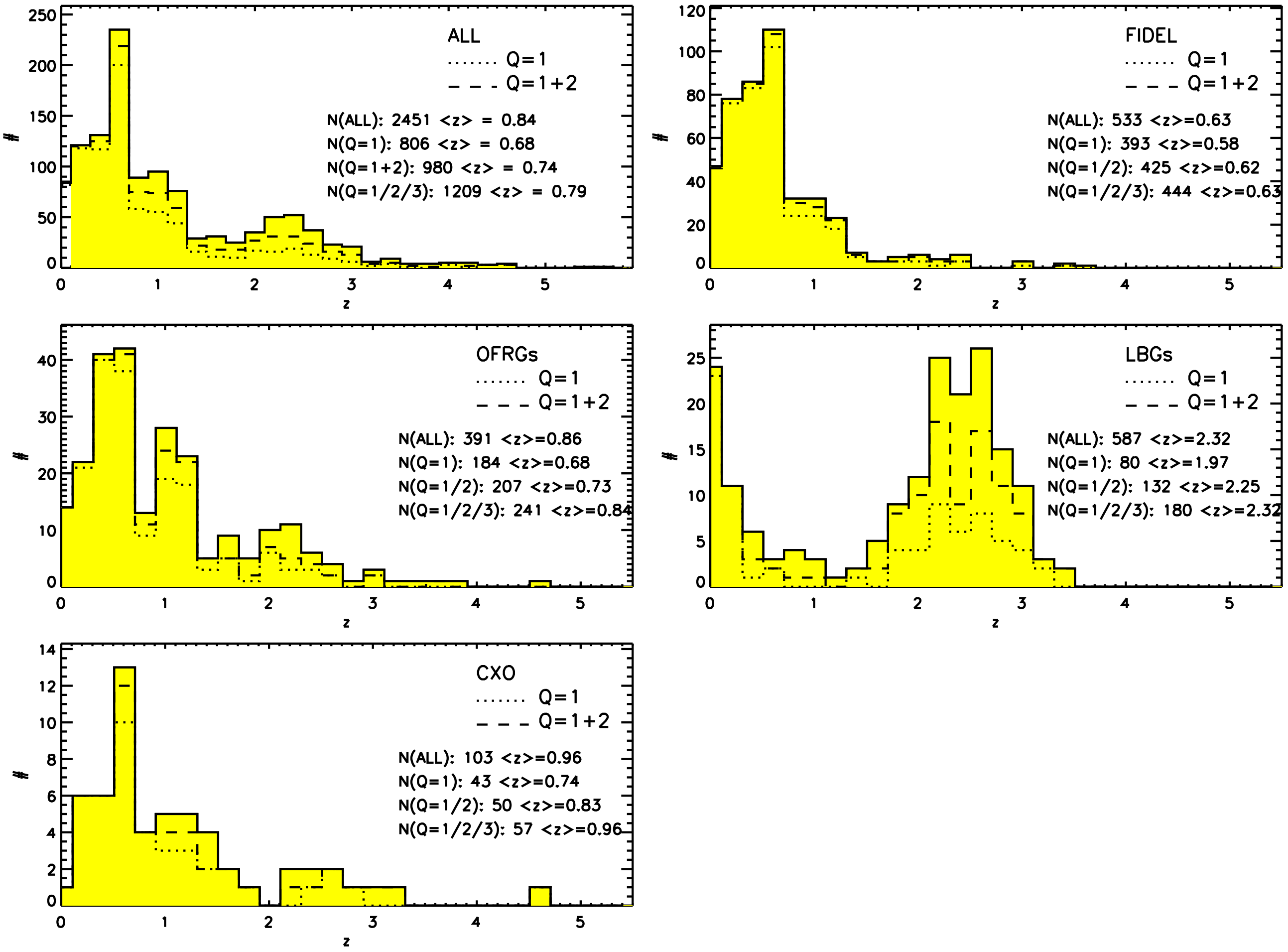

FIG. 15.— Spectroscopic redshift distributions for the various galaxy population targeted during the spectroscopic campaign. In each panel, we show the redshift distribution for all galaxies, but also show the histograms for the best quality (Q = 1) spectra, and those with Q = 1+2. The number of galaxies with spectroscopic redshifts (and the median redshift) are also given in the panels. *Top Left*: Redshift distribution for ALL galaxies targeted; *Top Right*: Redshift distribution for 24μm selected galaxies from the FIDEL survey; *Middle Left*: Redshift distribution for optically faint radio galaxies (OFRGs); *Middle Right:*: Redshift distribution for the LBGs, BX/BMs and Lyα emitters; *Bottom Left*: Redshift distribution for *Chandra* X-ray sources.

Table 3. Spectroscopic redshifts for the full sample

ID	RA (J2000)	DEC (J2000)	$z_{\rm spec}$	Q	Inst	ID	RA (J2000)	DEC (J2000)	$z_{\rm spec}$	Q	Inst
101	53.30820	-27.93445	4.6892	1	F	104	53.26036	-27.94606	1.9469	3	VF
106	52.90094	-27.91398	2.3484	3	VMF	107	52.89957	-27.91209	...	4	VMF
108	52.89780	-27.90952	...	4	VF	109	52.90089	-27.91278	3.0159	2	V
110	52.87580	-27.98573	1.4135	1	F	112	52.87865	-27.98229	0.4342	1	F
113	53.23814	-28.01708	1.3648	3	VF	114	53.23651	-28.01645	...	4	VF
116	53.31593	-27.76045	0.7516	1	VF	117	53.02072	-27.51948	0.9610	2	VF
118	53.01840	-27.52046	0.7283	3	VF	119	53.04730	-27.87038	...	4	F
280	53.08039	-27.87200	...	3	V	122	53.19980	-27.90448	3.1977	3	V
123	53.20365	-27.71445	...	4	VF	123b	53.20339	-27.71603	2.8382	2	V
124	52.96913	-28.05492	...	4	V	127	53.07793	-27.62877	...	4	V
131	53.03317	-27.97311	0.9607	3	VF	133	53.37387	-27.57901	1.2382	2	V
136	53.40405	-27.73279	1.4577	2	VF	137	53.40199	-27.73240	1.7620	3	V
138	53.40152	-27.73158	1.1612	1	VF	140	52.90397	-27.91962	2.5514	1	VMF
141	52.95923	-27.57584	...	4	VF	142	52.95815	-27.57699	...	4	VF
281	52.95785	-27.57508	...	4	V	143	53.25823	-27.74269	1.0908	1	VF
144	53.26195	-27.74324	...	4	F	146	53.43591	-28.06051	0.3345	1	V
148	53.18151	-27.77747	...	4	V	148b	53.18109	-27.77617	0.4031	2	V
149	53.18058	-27.77981	...	4	V	153	52.95378	-28.03722	...	4	V
154	53.40006	-27.89706	...	4	VF	156	52.93709	-27.57664	0.5747	1	VF
157	52.93737	-27.57499	...	4	VF	158	53.19516	-27.85588	...	3	V
159	52.79084	-27.87367	1.2121	1	VF	161	53.12960	-27.98379	...	4	V
164	52.87994	-27.54404	...	4	V	167	53.23330	-27.55525	...	3	VF
168	53.23257	-27.55572	...	4	VF	169	53.15837	-27.53318	...	4	VF
171	52.85102	-27.84553	1.2146	3	F	172	52.92079	-27.74305	...	4	VF
173	52.92196	-27.74666	0.6820	1	VF	174	52.91919	-27.74473	...	4	V
176	52.93513	-27.73924	1.3423	2	VF	177	52.86826	-27.93558	0.6934	1	F
178	52.87039	-27.93566	...	4	V	179	52.99573	-27.91064	0.6322	3	VF
180	52.99575	-27.91028	0.7347	1	VF	181	53.18184	-27.56571	3.0883	3	VF
183	53.25685	-27.67803	1.0157	1	VF	184	53.26075	-27.67564	1.4706	1	VF
185	52.97122	-27.66033	...	3	VF	186	52.96723	-27.65739	2.3428	3	VF
187	52.96914	-27.89275	...	4	V	188	53.10667	-27.55177	...	4	V
190	53.26511	-27.73685	...	4	VF	191	53.32252	-27.85779	...	3	VF
192	53.19174	-28.00580	3.0000	3	VF	194	53.28530	-28.01194	0.9100	1	VF
195	53.00438	-28.00701	4.0572	1	F	196	53.21742	-27.59211	1.4804	1	VF
197	53.22011	-27.58916	...	3	VF	200	53.14152	-27.65409	...	3	V
202	52.89456	-27.99353	1.2853	1	VF	203	52.89452	-27.99251	...	3	VF
205	52.93304	-27.64314	2.3315	2	VF	207	53.27361	-27.55739	...	3	V
208	53.27499	-27.55620	...	3	V	209	53.16690	-27.63571	0.8219	2	V
212	52.86020	-27.93175	0.4134	1	V	214	52.98871	-27.94441	2.3199	3	VF
215	53.41730	-27.66357	2.0835	1	VF	218	52.92363	-27.80834	...	4	VF
221	53.28648	-28.08768	0.6122	1	F	224	52.97838	-27.85286	0.7818	2	F
225	52.79045	-27.75211	1.8930	3	V	226	52.80880	-27.81224	1.2081	2	VF
227b	53.20340	-27.52238	0.3370	1	V	231	53.17869	-27.59927	...	4	V
232	52.89580	-27.67712	0.9890	1	F	233	52.90919	-27.72464	1.0216	1	VF
233b	52.90940	-27.72599	5.6982	1	F	233c	52.90940	-27.72421	0.7315	1	F
234	52.90397	-27.72800	...	4	V	235	52.90971	-27.72320	...	4	V
236	52.79493	-27.93124	0.2797	1	V	239	53.17192	-27.97811	...	4	V
240	53.30445	-27.93250	...	4	VF	241	53.30720	-27.63736	1.2430	1	VF
243	52.87803	-27.95972	1.3681	1	VF	243b	52.87786	-27.95898	0.0000	1	VF
244	53.21397	-27.92878	...	4	VF	246	52.96459	-27.76491	0.7360	1	VF
248	53.35575	-27.56628	...	4	VF	249	53.24092	-27.63307	...	4	VF
250	52.81975	-27.88515	1.2919	1	VF	251	52.91739	-27.93955	1.6172	1	VMF
252	52.91858	-27.94281	1.3928	2	VF	253	53.36660	-27.70067	...	4	VF
254	52.84473	-27.90341	0.7105	1	VF	256	53.35508	-27.57387	2.8167	1	VF
256b	53.35492	-27.57354	...	3	VF	256c	53.35498	-27.57271	0.1812	1	V
256d	53.35496	-27.57589	...	4	VF	278	53.15499	-27.97946	...	3	V
261	52.95705	-27.74452	2.4363	1	V	264	52.86519	-27.65771	...	4	V
265	52.86966	-27.65466	...	3	V	267	52.84107	-27.82601	0.9660	1	VF
269	53.23577	-28.05351	0.2018	1	VF	270	53.36911	-27.94851	1.2020	3	VMF
271	53.38776	-27.57848	...	4	VF	279	53.38899	-27.57889	...	4	V
285	53.38725	-27.58079	2.3438	1	V	273	53.37595	-27.89609	0.1282	1	F
275	53.01275	-27.60056	...	3	VF	276	52.94360	-27.77323	...	4	V
501	53.22343	-27.71864	...	4	VF	503	52.95048	-28.04232	0.7142	1	V
505	53.00151	-28.04868	...	4	V	506	53.13635	-27.76317	0.9500	2	V
506b	53.13637	-27.76078	0.3679	1	V	507	53.31770	-28.03982	0.3492	1	VF
508	52.87516	-27.98211	...	4	V	510	53.00172	-28.03963	...	3	V
510b	53.00186	-28.04357	0.5025	3	V	512	53.30218	-27.77633	0.6084	1	VF
513	53.19716	-27.71331	0.7329	1	V	515	53.18329	-27.56036	...	3	V
515b	53.18321	-27.56240	0.3585	1	V	515c	53.18365	-27.55663	0.4439	1	V
518	52.95645	-27.72207	1.3182	1	VF	519	52.81618	-27.65650	...	4	V
520	52.87198	-27.55570	2.4264	2	V	521	53.17759	-28.01270	0.5350	1	V

Continued from previous page

ID	RA	DEC	z_{spec}	Q	Inst	ID	RA	DEC	z_{spec}	Q	Inst
	(J2000)	(J2000)					(J2000)	(J2000)			
522	52.87832	-27.98233	0.4341	1	VF	523	53.06699	-27.65110	...	4	V
524	53.09277	-27.80130	...	4	V	526	53.36983	-27.91366	3.3378	3	VF
527	53.07715	-27.61020	...	4	V	529	53.37672	-27.65638	...	4	VF
530	53.12473	-27.71670	...	4	V	532	52.95085	-27.75965	...	4	V
533	53.31748	-27.82900	...	4	F	535	53.11880	-27.78280	2.3173	2	V
536	52.86536	-27.62819	...	4	V	538	53.30283	-27.98957	0.5207	1	VF
540	53.02307	-27.98948	...	4	V	541	53.27858	-27.70157	0.5351	1	V
542	53.33718	-27.99891	2.0151	2	V	543	52.96118	-27.59499	...	4	V
544	52.95010	-27.80043	1.9364	2	V	545	52.86406	-27.62923	...	4	V
545b	52.86452	-27.62960	3.7085	3	V	547	52.92422	-27.92700	1.2239	1	VF
548	53.16553	-28.05321	...	3	V	550	52.87667	-27.66678	...	4	V
551	53.06944	-27.66443	...	4	V	553	53.19533	-27.70429	0.1046	1	V
554	53.42113	-27.92732	3.1988	1	V	556	53.04854	-27.62511	...	3	V
558	53.11058	-27.54513	0.2466	2	V	559	52.89666	-27.58582	2.5340	3	V
562	52.97792	-27.82897	...	4	V	566	53.02913	-28.03683	...	4	V
567	53.15111	-27.77443	...	4	V	567b	53.15058	-27.77171	0.2206	1	V
570	52.83292	-27.59715	0.5219	1	V	571	53.31645	-28.04119	...	4	V
572	53.26260	-27.86292	...	4	VF	573	53.21903	-27.99544	...	4	VF
574	52.79282	-27.67234	0.3745	2	V	575	53.22799	-27.57255	0.1424	1	V
577	53.16329	-27.53075	...	4	V	578	53.04843	-27.62385	3.0173	2	V
580	53.13753	-27.76309	...	4	V	580b	53.13734	-27.76272	0.3648	1	V
581	53.27587	-27.81176	...	3	V	582	52.82342	-27.68985	0.3414	1	V
583	52.98446	-27.66724	...	4	V	585b	53.11046	-27.54561	0.2573	1	V
587	52.95712	-27.72404	0.6204	1	V	591	52.87715	-27.66420	...	4	V
702	52.90063	-27.91078	...	4	V	703	52.87399	-27.98576	0.7502	1	V
705	53.37486	-27.57718	...	3	V	707	52.90387	-27.91592	...	4	V
719	53.10521	-27.87408	...	3	F	725	52.93735	-27.74126	0.6729	3	V
728	52.86829	-27.93299	...	4	V	743	53.19147	-28.00614	...	4	V
766	52.99031	-27.94128	0.7346	1	F	768	53.41829	-27.66754	...	4	V
771	53.41612	-27.66591	...	4	V	777	53.22199	-27.63560	...	3	V
780	53.22304	-27.63760	0.6856	3	V	781	53.28810	-28.08980	0.8574	1	F
786	53.18211	-27.59969	...	4	V	787	53.18330	-27.59864	...	4	V
788	53.18253	-27.59760	...	3	V	789	53.17972	-27.59789	0.7300	1	V
794	52.90948	-27.72758	1.5042	2	VF	802	53.30505	-27.63561	0.3331	1	V
804	53.30690	-27.63379	...	3	V	806	53.21447	-27.92528	...	3	V
814	52.81503	-27.88927	0.1812	1	V	818	52.88034	-27.86519	0.5767	1	V
820	52.87740	-27.86232	0.6762	1	VF	821	53.36793	-27.70021	...	4	V
823	53.36948	-27.69804	2.4295	2	V	824	53.36879	-27.69734	...	4	F
826	53.15142	-27.98096	...	4	V	829	52.97931	-27.75566	...	3	V
837	53.01600	-27.60166	0.7197	1	V	841	52.94331	-27.77217	4.3830	2	F
842	52.93991	-27.77091	0.2484	1	VF	902	53.21524	-27.86681	...	3	V
903	53.14357	-27.83472	...	4	V	904	53.09147	-27.81547	...	3	V
905	53.10593	-27.80840	2.3431	3	V	906	53.14059	-27.79561	...	3	V
907	53.07402	-27.77780	1.7406	3	V	908	53.07813	-27.77203	1.8000	4	V
909	53.11838	-27.71293	2.1437	2	V	910	53.04334	-27.84534	...	4	M
1001	52.80350	-27.75873	0.8580	3	V	1003	52.80960	-28.03117	1.4165	2	V
1007	52.81120	-27.64039	0.3123	1	V	1009	52.82320	-27.60384	0.5241	1	V
1010	52.82420	-27.59576	0.5488	1	V	1012	52.84440	-27.59401	0.4840	1	V
1013	52.84490	-27.79059	0.1813	1	V	1014	52.84770	-27.94956	...	4	VM
1014b	52.84779	-27.95035	2.3923	2	V	1015	52.84970	-27.87331	0.3394	1	V
1016	52.85180	-27.95301	0.5266	1	VF	1017	52.85410	-27.78478	0.5257	1	V
1018	52.85920	-27.69887	...	4	V	1019	52.86350	-27.89903	0.5583	1	VMF
1020	52.86670	-27.69873	0.7306	1	V	1021	52.86970	-27.69317	...	4	V
1025	52.88080	-27.62437	1.6191	1	VF	1027	52.88310	-27.58962	0.4462	1	V
1038	52.93520	-27.70348	0.9719	1	VF	1040	52.94250	-27.60734	0.8972	1	VF
1044	52.95300	-27.55326	0.6851	1	VF	1045	52.95440	-27.92209	1.2866	1	V
1047	52.95770	-27.73156	0.6701	1	VF	1048	52.95790	-27.83842	0.7366	1	V
1051	52.98030	-27.77637	1.0367	1	VF	1053	52.99280	-27.84492	...	4	F
1054	52.99840	-27.59995	...	4	V	1055	53.00490	-27.55381	0.7340	1	V
1056	53.00880	-27.69126	...	4	V	1057	53.01160	-27.53984	1.0470	1	VF
1060	53.01800	-27.55187	1.1871	3	V	1061	53.02180	-28.07087	1.8979	1	V
1062	53.03160	-27.82420	0.4685	1	V	1064	53.03600	-27.67851	0.3699	1	V
1065	53.03660	-27.54442	0.5276	1	V	1067	53.04090	-27.58437	...	4	V
1068	53.04520	-27.94387	0.6739	1	V	1069	53.04940	-27.63900	0.3488	1	V
1070	53.04970	-27.64445	0.7291	1	V	1071	53.05180	-28.01706	0.6747	1	V
1072	53.05280	-27.58995	0.4089	1	V	1074	53.06310	-28.08959	0.2756	1	V
1075	53.06630	-28.06312	0.5193	1	V	1076	53.06950	-28.07331	0.9264	2	V
1078	53.07380	-28.04131	0.2813	1	V	1087	53.09570	-27.91462	0.6546	1	VF
1088	53.09860	-27.61345	0.5032	1	V	1089	53.10430	-27.63959	...	4	V
1091	53.11010	-27.57609	0.7444	2	V	1093	53.11580	-27.63042	1.1321	1	V
1094	53.11810	-27.64498	0.3832	1	V	1096	53.12240	-27.58545	0.7087	1	V
1097	53.12340	-27.71175	0.6676	1	V	1099	53.12730	-27.98648	0.1246	1	V
1100	53.13010	-27.61878	0.1223	1	V	1103	53.14250	-27.60259	0.7357	1	V

Continued from previous page

ID	RA (J2000)	DEC (J2000)	$z_{\rm spec}$	Q	Inst	ID	RA (J2000)	DEC (J2000)	$z_{\rm spec}$	Q	Inst
1105	53.14610	-27.92562	0.0379	1	V	1106	53.14730	-27.58864	0.7345	1	V
1108	53.15520	-27.85778	0.5233	1	V	1112	53.16510	-28.01973	0.5294	1	VF
1113	53.16720	-27.62178	0.2965	1	V	1116	53.17730	-27.64053	0.2511	1	V
1122	53.19290	-27.89073	...	4	V	1124	53.20560	-27.61009	0.6288	1	VF
1128	53.21580	-27.99898	0.6197	1	VF	1132	53.24010	-27.72178	0.6675	1	VF
1133	53.24660	-27.72367	1.1323	1	F	1136	53.26690	-27.67126	0.5366	1	V
1137	53.27140	-27.67423	0.3104	1	V	1139	53.28030	-27.76420	0.2179	1	V
1142	53.28570	-28.06884	0.4870	1	F	1144	53.29230	-27.72734	0.1449	1	V
1148	53.31040	-27.79651	1.1620	1	F	1151	53.31960	-27.94170	0.6849	1	V
1153	53.32070	-28.03075	1.1174	1	VF	1154	53.32350	-27.62420	0.3542	1	V
1156	53.32400	-27.77317	1.3468	2	FV	1157	53.32860	-27.90939	0.5256	1	VF
1158	53.32910	-27.59206	0.1481	1	V	1160	53.33660	-27.57548	0.3107	1	V
1162	53.33960	-27.94564	0.6042	1	VF	1163	53.34590	-27.63387	...	4	V
1163b	53.34591	-27.63308	...	4	V	1165	53.37090	-27.66578	1.0429	1	VF
1168	53.38100	-27.77845	0.6861	1	V	1170	53.38960	-27.94617	0.4221	1	V
1171	53.39150	-27.59931	1.2393	1	VF	1172	53.39590	-27.85903	0.2219	1	V
1173	53.39670	-27.80562	...	4	V	1300	53.36510	-27.68261	1.5364	1	F
1302	53.35990	-27.57133	2.5214	3	V	1309	53.02750	-27.82145	0.6777	1	V
1310	52.99640	-27.54701	0.7855	1	F	1316	52.99200	-27.58935	...	4	VF
1317	52.97760	-28.01706	0.6270	1	V	1321	53.02010	-28.02934	0.3768	1	V
1323	53.32920	-27.70818	...	4	V	1326	53.22440	-27.65758	1.3234	1	F
1328	53.28810	-27.97399	2.5718	1	V	1330	53.39930	-27.81068	...	4	V
1331	53.38070	-27.94284	2.6032	1	VF	1333	53.25860	-27.56497	...	4	V
1337	53.04350	-28.01944	...	4	F	1337b	53.04340	-28.02027	0.9009	2	F
1339	53.18650	-27.73508	0.1043	1	V	1342	53.29600	-27.58749	...	4	V
1344	52.97670	-27.73408	...	4	V	1345	53.05140	-27.73153	0.4225	1	V
1347	53.19130	-28.01456	0.8176	1	F	1348	53.06440	-27.96694	0.7354	1	V
1351	53.31230	-27.76571	0.5359	1	F	1353	52.98060	-27.91335	0.7377	1	F
1354	52.94900	-27.91469	...	4	V	1355	53.25680	-27.91967	...	4	V
1356	53.02860	-27.87022	...	4	V	1360	52.97870	-27.94832	1.9578	1	V
1361	53.17100	-27.60681	...	4	VF	1368	53.36820	-27.61207	1.1740	2	F
1370	53.07290	-27.98201	1.0772	1	F	1371	53.00650	-27.98875	0.7340	1	F
1373	52.87560	-27.63656	0.7076	3	V	1377	53.20280	-27.64829	0.8411	1	V
1379	53.28960	-27.76283	0.8892	1	F	1380	53.34510	-27.77357	0.6837	1	V
1380b	53.34512	-27.77273	...	4	V	1384	53.34200	-27.64688	...	4	V
1386	53.30230	-27.84265	0.1296	1	V	1387	53.01910	-27.83520	0.2295	1	V
1390	52.87030	-27.65245	...	4	V	1392	53.25450	-27.70483	0.9666	1	F
1394	52.82290	-27.97225	...	4	V	1396	53.36630	-27.95154	...	4	F
1398	52.98720	-27.60767	...	4	V	1401	53.34870	-27.81991	...	4	V
1405	53.32980	-27.61980	0.6799	1	V	1408	53.34930	-27.72888	0.5336	1	V
1411	52.86540	-27.63504	0.7016	1	V	1412	52.97310	-27.61611	0.5757	1	F
1413	52.94920	-27.65222	1.0369	1	F	1416	53.33420	-27.77015	0.9788	1	F
1418	52.86860	-27.89492	0.2652	1	V	1419	53.34070	-28.06216	0.7728	1	V
1421	53.35660	-27.72767	0.4231	1	VF	1423	52.83540	-27.83319	0.4159	1	VF
1425	52.97100	-27.93517	0.6772	1	V	1428	53.18590	-27.70070	0.7090	1	V
1429	52.98690	-28.03020	1.3808	1	V	1433	52.97180	-27.62520	...	4	V
1436	53.00660	-27.93306	...	4	V	1438	53.12300	-27.56101	0.1462	1	V
1440	53.22120	-27.69317	0.6049	1	V	1442	53.16490	-27.58950	0.2494	1	V
1444	52.86310	-27.64148	0.3747	1	V	1445	53.27690	-27.73996	0.3315	1	V
1447	53.28120	-27.73924	0.9806	1	F	1449	53.24850	-28.02112	0.5502	1	VF
1450	52.87330	-27.57175	0.6788	1	V	1454	53.36920	-27.98084	0.7512	2	F
1455	52.87160	-27.58649	...	4	V	1457	53.26550	-27.60303	0.6229	1	V
1459	53.32570	-27.73872	...	4	V	1461	53.00530	-27.89344	0.4216	1	V
1462	53.31260	-28.04744	0.2104	1	V	1463	53.26830	-27.81533	...	4	V
1464	53.28740	-27.99693	0.5405	2	VF	1465	53.04980	-27.56625	0.6703	1	V
1467	52.92230	-27.74630	0.6817	1	F	1469	52.97360	-27.90600	0.7350	1	F
1471	52.98070	-27.69937	0.6070	3	V	1472	53.21970	-27.70180	0.6669	1	VF
1476	52.83970	-28.00590	...	4	V	1477	53.17010	-27.92975	...	4	V
1479	52.98040	-27.72045	...	4	V	1480	52.88490	-27.63824	0.5488	1	VF
1480b	52.88486	-27.63794	...	4	V	1481	52.91730	-27.75408	0.3936	1	F
1484	52.80170	-27.66411	...	4	V	1485	52.91800	-27.78270	1.0208	1	F
1488	53.02310	-27.63265	0.9590	1	V	1489	53.23990	-27.76442	0.5324	1	V
1490	53.19810	-27.74788	...	4	V	1491	53.02700	-27.94965	0.6557	1	VF
1492	53.33310	-27.80752	1.2029	3	V	1492b	53.33385	-27.80615	0.1327	1	V
1494	53.14410	-27.70674	0.4695	1	V	1497	52.97190	-27.67525	2.1784	3	V
1499	53.08320	-27.95124	1.0891	1	F	1504	52.84360	-27.60057	1.8735	4	V
1505	53.00370	-27.79908	...	4	V	1506	53.26160	-27.56795	0.5014	1	V
1509	52.99470	-27.60649	0.8355	1	V	1511	53.37880	-27.79851	...	4	V
1515	53.07030	-27.90505	0.9653	2	F	1520	53.00130	-28.10628	0.8583	2	V
1521	52.94920	-28.06780	...	4	V	1523	52.79930	-27.75418	...	4	V
1524	53.12650	-27.51131	0.8368	3	V	1526	52.97530	-27.83474	0.7430	1	VF
1527	53.23150	-27.72289	0.1465	1	V	1528	52.85360	-27.86877	1.2262	2	F

Continued from previous page

ID	RA (J2000)	DEC (J2000)	$z_{\rm spec}$	Q	Inst	ID	RA (J2000)	DEC (J2000)	$z_{\rm spec}$	Q	Inst
1530	52.84370	-27.88007	...	4	V	1531	53.00510	-27.69294	0.7337	1	V
1537	53.41500	-27.77399	0.4232	1	V	1538	53.20790	-27.64479	0.6942	3	V
1539	52.87060	-27.84842	0.8451	1	V	1540	53.16570	-28.07147	0.7439	1	V
1541	52.97530	-27.51528	0.0878	3	F	1547	52.90800	-27.59477	0.6248	1	V
1552	52.88100	-27.81680	0.8194	1	V	1562	53.35970	-27.72191	0.9636	1	F
1564	53.16140	-27.53533	0.7063	1	V	1565	53.38700	-27.74704	1.4419	3	F
1566	52.86740	-27.99014	0.1142	1	V	1568	53.23540	-28.04722	1.2124	1	F
1573	53.18340	-28.02956	...	4	V	1576	53.08620	-27.86183	0.6793	1	V
1579	52.99270	-27.91559	0.7372	1	VF	1581	52.98830	-28.05121	0.7954	1	V
1583	52.86640	-28.04544	0.8202	1	V	1584	52.96780	-27.58942	...	4	V
1585	53.23870	-27.72653	1.0415	2	V	1586	53.16190	-27.98851	1.1542	1	V
1587	53.31100	-27.80918	0.8264	1	F	1589	53.21820	-27.69785	0.6099	1	VF
1589b	53.12827	-27.69598	...	4	V	1591	53.04920	-28.12347	0.6993	1	V
1592	53.06980	-28.03257	0.7801	1	VF	1594	53.20210	-27.82629	...	4	V
1595	52.96630	-27.81315	0.5088	1	V	1597	53.25500	-27.97108	2.2920	3	V
1601	52.86290	-27.66683	1.3543	2	V	1603	52.88700	-28.05002	0.7576	1	V
1604	53.17330	-28.02438	0.6842	1	VF	1608	53.13640	-27.90634	0.2134	1	V
1614	53.21540	-27.55110	0.4753	1	V	1615	52.89000	-27.98120	1.5656	1	F
1616	53.13220	-27.95662	0.6636	1	V	1617	52.99290	-27.56063	0.6265	1	VF
1620	53.01060	-28.05579	1.0189	1	V	1621	53.28430	-27.88142	0.7369	2	V
1623	52.96150	-27.78428	2.2546	1	VF	1626	53.33970	-28.07257	1.0448	2	V
1632	53.42620	-27.91408	0.5785	1	V	1634	53.40750	-28.00819	0.3586	1	V
1635	52.94830	-27.99369	0.2361	1	V	1637	53.35430	-27.78462	1.4220	1	V
1641	53.38940	-27.75876	0.4236	1	V	1642	53.12130	-27.59482	1.3198	3	V
1643	53.01320	-28.08244	0.3391	1	V	1644	53.08460	-28.03729	1.6211	1	V
1647	52.96480	-27.66361	0.2896	1	V	1650	52.86120	-27.57410	...	4	V
1653	53.40150	-28.02368	2.2895	2	V	1655	53.07050	-27.62165	0.1468	1	V
1657	53.32050	-27.99894	0.9329	1	F	1658	53.37050	-27.94472	0.8417	1	V
1659	53.34220	-27.86575	0.6875	1	VF	1662	53.25900	-27.53206	0.6076	1	V
1665	53.08280	-27.95561	0.6722	1	VF	1665b	53.08304	-27.95330	3.0779	2	V
1667	53.04540	-27.78947	0.4159	1	V	1671	53.38570	-27.69122	0.7077	1	VF
1673	53.02890	-27.93613	0.7747	1	VF	1675	53.03350	-28.06681	0.7144	1	V
1676	52.98520	-27.58754	0.2325	1	V	1677	52.88630	-27.68401	0.7195	1	VF]
1682	52.81280	-27.82158	1.0255	1	F	1683	53.35930	-27.97491	2.1636	1	M
1684	52.95430	-27.90617	0.5769	1	V	1685b	52.86354	-27.89825	0.7758	1	VF
1686	52.96730	-27.87835	0.6518	1	V	1689	52.96630	-28.01684	0.6109	1	V
1690	52.83270	-27.74496	...	4	V	1691	52.90880	-27.78660	1.0464	1	VF
1693	52.98710	-27.68835	...	4	V	1695	53.43400	-27.95912	...	4	V
1697	53.27950	-27.66337	0.4159	1	VF	1698	53.26540	-27.75846	0.1275	1	V
1699	53.20440	-27.60196	2.0006	3	V	1703	53.39400	-27.79752	...	4	V
1704	52.89550	-27.57860	0.5693	2	V	1706	52.87830	-27.54865	0.2395	1	V
1707	53.32210	-28.09798	1.1148	2	F	1708	53.37610	-27.99588	0.5426	1	V
1710	53.30250	-27.93102	2.5678	1	FM	1712	53.33330	-27.98676	0.6827	1	VF
1713	53.14070	-28.08259	0.6819	1	V	1714	52.90040	-27.53427	...	4	V
1720	52.84570	-27.63237	0.7362	1	V	1725	53.37530	-27.93658	0.1415	1	V
1726	53.27490	-28.00708	0.6329	1	VF	1728	52.86540	-27.79091	0.6805	1	V
1731	53.04960	-28.02498	0.2156	1	V	1732	52.82400	-27.97024	0.6247	1	V
1733	52.81800	-27.67595	...	4	V	1734	52.97900	-27.73624	1.3662	1	F
1736	53.00490	-27.55540	0.7329	1	VF	1740	53.02690	-28.01256	0.6823	1	VF
1741	53.04070	-27.88679	0.7409	1	V	1747	53.01310	-28.05811	...	4	V
1750	53.07610	-28.00229	1.1269	1	F	1752	53.38670	-28.08463	0.5643	1	V
1763	53.01630	-27.95076	0.3130	1	V	1768	53.25230	-27.61162	0.2778	1	V
1772	53.13100	-27.82934	0.2132	1	V	1773	53.10470	-27.70532	1.6168	1	V
1777	52.81350	-27.84906	1.1070	3	F	1780	53.19780	-27.68514	0.4175	1	V
1781	52.89170	-27.69824	0.2186	1	F	1782	52.97190	-27.53468	0.6154	1	VF
1784	53.27560	-28.03452	0.7332	1	F	1788	53.11890	-27.59354	0.5261	1	V
1789	52.93220	-27.58146	...	4	V	1791	53.08340	-27.74667	...	4	V
1792	53.00000	-27.52924	0.2267	1	VF	1795	52.82850	-27.58555	0.8583	2	V
1803	53.13960	-27.65791	0.9798	1	V	1804	52.80200	-27.91609	0.7845	1	VF
1805	52.99230	-27.63786	0.6880	1	V	1810	53.11280	-27.50607	0.6036	1	V
1811	53.34210	-27.80669	0.1247	1	V	1812	53.36360	-27.78323	0.1282	1	V
1814	52.93370	-27.96356	0.8407	1	F	1820	53.35840	-27.64634	1.1172	1	F
1824	52.80120	-27.83878	...	4	V	1827	53.01820	-28.07544	0.2811	1	V
1828	52.83030	-27.96873	0.5276	1	V	1830b	53.06941	-28.06968	0.3336	1	V
1831	53.20610	-27.60335	0.1032	1	V	1833	53.22030	-27.64383	1.2265	1	F
1835	53.10420	-28.06795	0.3825	1	V	1849	53.42330	-27.78427	0.4228	1	V
1853	53.43510	-27.98447	...	4	V	1856	53.12250	-28.06119	0.2145	1	V
1857	53.10040	-27.96671	0.6177	1	V	1863	53.29010	-27.73535	0.1019	1	V
1864	53.22860	-27.96237	0.1753	1	V	1870	53.40730	-28.06725	0.6483	1	V
1873	53.28260	-28.08553	0.6120	2	F	1885	53.21490	-27.98842	0.9593	1	V
1888	53.40400	-27.77657	0.1467	1	V	1891	53.25320	-27.57063	0.0852	1	V
1893	53.08160	-28.07315	0.2409	1	V	1896	52.82620	-27.97744	0.6806	1	V
1897	52.95230	-28.07607	...	4	V	1902	53.39990	-27.87178	0.1822	1	V
1908	53.31130	-28.08513	0.5366	1	V	1913	52.93710	-27.68236	0.4202	1	V

Continued from previous page

ID	RA (J2000)	DEC (J2000)	$z_{\rm spec}$	Q	Inst	ID	RA (J2000)	DEC (J2000)	$z_{\rm spec}$	Q	Inst
1914	53.15210	-27.58138	1.3631	1	F	1917	52.89750	-28.05438	1.3470	1	V
1917b	52.89785	-28.05260	0.2742	1	V	1919	53.42950	-27.75124	0.7809	1	F
1922	53.23880	-27.50062	...	4	V	1924	52.98200	-27.64443	0.5233	1	V
1925	53.25290	-27.64591	0.4275	1	VF	1926	53.00940	-27.66872	0.2270	1	V
1927	52.94260	-27.55717	...	4	V	1931	53.02130	-28.09698	0.2981	1	V
1932	52.83610	-27.77634	0.0745	1	V	1935	52.95780	-27.81029	0.1829	1	V
1944	53.43490	-27.93112	0.2790	1	V	1945	52.99470	-27.53316	0.6265	1	V
1951	53.21610	-27.74343	0.5212	1	1951	1954	53.20840	-27.57718	0.2510	1	V
1954b	53.20810	-27.57576	0.2521	1	V	1954c	53.20800	-27.57933	0.2517	1	V
1962	53.29950	-27.89631	0.5330	1	V	1964	52.89460	-27.93016	0.0961	1	V
1966	53.13400	-28.07412	3.4113	3	V	1968	53.41020	-28.04829	3.4418	1	V
1969	53.05680	-27.56649	...	4	V	1973	53.11300	-28.02339	0.5256	1	V
1977	53.19490	-27.51752	0.8707	1	V	1978	52.85530	-27.99961	1.3751	1	F
1980	53.16160	-27.74682	0.7332	1	V	1988	53.21790	-27.76164	1.3666	1	V
1995	53.30090	-28.02345	0.2900	1	V	1995b	53.30082	-28.02497	0.3327	1	V
2008	53.23600	-27.88812	0.3670	1	V	2009	53.25390	-28.01036	0.1456	1	V
2010	53.12970	-28.07885	0.1552	1	V	2011	52.97450	-28.05944	0.1253	1	V
2014	53.33860	-27.55832	0.5024	1	V	2016	52.90280	-28.10337	...	4	V
2020	53.36040	-27.74578	0.4474	1	V	2026	53.18750	-27.91096	0.4588	1	V
2031	52.94140	-27.85832	0.6811	1	V	2038	53.15950	-28.06826	0.1079	1	V
2039	53.43240	-28.01761	1.3180	1	V	2045	53.34110	-27.68034	0.1482	1	V
2046	53.37780	-27.73411	0.8599	1	V	2052	53.28630	-27.56839	0.6995	2	V
2055	53.17490	-27.66371	0.1538	1	V	2067	53.16320	-27.89933	0.5592	1	V
2069	53.36000	-27.69355	0.0996	1	V	2073	52.88160	-27.75541	0.1793	1	V
2081	52.84080	-27.85636	1.3699	1	F	2086	53.18690	-27.79099	0.2140	1	V
2086b	53.18659	-27.79022	0.1229	1	V	2093	53.39660	-27.76382	0.2192	1	V
2095	53.16210	-27.95010	0.2974	1	F	2096	52.87520	-27.93395	0.6768	1	V
2097	52.81040	-27.61104	0.4838	1	V	2111	53.29040	-27.80044	0.1781	1	V
2112	52.88670	-28.02107	0.1422	1	V	2112b	52.88681	-28.01871	0.1430	1	V
2119	53.18430	-27.86142	0.2787	1	V	4004	52.93092	-27.85105	0.3108	1	V
4009	52.93816	-27.83059	2.7211	1	V	4010	52.93839	-27.90994	1.8892	1	V
4012b	53.14269	-27.64875	0.5610	1	V	4020	53.24056	-27.73051	...	4	V
4022	52.95833	-27.81137	0.4168	1	V	4029	52.96232	-27.68815	0.6697	1	V
4034	52.96646	-27.82493	...	4	V	4035	52.96743	-27.80451	1.2090	2	V
4036	52.96765	-27.69624	...	4	V	4092	53.01447	-27.82647	...	4	V
4104	53.01983	-27.77082	...	4	V	4110	53.02427	-27.80580	...	4	V
4120	53.02813	-27.82269	0.6532	1	V	4122	53.02868	-27.76360	0.8423	1	V
4124	53.02920	-27.84172	0.7337	1	VF	4129	53.03072	-27.81419	0.6206	1	V
4143	53.03841	-27.86209	1.3576	1	VF	4151	53.04095	-27.83612	1.3127	3	V
4155	53.04375	-27.90470	0.6879	2	V	4160	53.04548	-27.78975	0.4226	1	V
4165	53.04608	-27.74912	0.8320	1	V	4168	53.04765	-27.86517	1.0358	3	V
4170	53.04810	-27.78702	0.5758	1	V	4177	53.05141	-27.68347	...	4	V
4179	53.05219	-27.79828	0.3329	1	V	4190	53.05577	-27.73250	...	4	V
4198	53.05896	-27.81962	...	4	V	4200	53.05971	-27.82243	...	4	M
4205	53.06184	-27.79409	0.7362	3	V	4212	53.06358	-27.74406	...	4	V
4221	53.06628	-27.80061	...	4	V	4232	53.07067	-27.83449	...	4	V
4233	53.07075	-27.85072	...	4	V	4238	53.07160	-27.76986	...	4	V
4241	53.07323	-27.82817	0.3376	1	V	4242	53.07348	-27.80336	...	4	V
4245	53.07457	-27.85002	...	4	M	4249	53.07556	-27.61639	...	4	V
4251	53.07600	-27.78063	...	4	V	4256	53.07794	-27.82228	...	4	V
4259	53.07865	-27.75822	0.2969	1	V	4264	53.08025	-27.77574	0.7441	2	V
4266	53.08036	-27.81565	0.6777	1	V	4266b	53.08007	-27.81301	2.7404	1	V
4269	53.08213	-27.76726	...	4	V	4278	53.08469	-27.76534	0.2302	1	V
4286	53.08735	-27.92955	...	4	V	4287	53.08761	-27.75487	...	4	V
4326	53.10251	-27.81473	0.5812	1	V	4327	53.10270	-27.86060	...	4	V
4333	53.10354	-27.84734	0.5905	3	V	4342	53.10500	-27.73452	0.0762	1	V
4358	53.10921	-27.85298	0.6706	1	F	4360	53.10967	-27.82086	0.3400	1	V
4372	53.11330	-27.73794	0.4204	1	V	4379	53.11658	-27.80178	...	4	V
4387	53.11987	-27.74325	...	4	V	4389	53.12019	-27.79888	...	4	V
4390	53.12083	-27.81903	...	4	V	4392	53.12087	-27.77327	...	4	4392
4393	53.12090	-27.82313	...	4	V	4397	53.12192	-27.75294	...	4	V
4401	53.12350	-27.90150	...	4	V	4415	53.12549	-27.73010	0.6672	1	V
4420	53.12654	-27.75662	...	4	V	4426	53.13067	-27.79038	0.6659	1	V
4439	53.13429	-27.81266	0.5354	1	V	4440	53.13455	-27.77103	...	4	V
4443	53.13638	-27.81666	0.6699	1	4443	4449	53.13775	-27.80217	...	4	V
4457	53.14100	-27.76683	...	4	V	4461	53.14178	-27.84142	...	4	V
4464	53.14237	-27.76512	0.3651	1	V	4473	53.14568	-27.90366	0.2805	1	V
4475	53.14599	-27.82571	...	4	V	4476	53.14608	-27.78002	...	4	V
4488	53.14992	-27.85515	0.3588	1	V	4489	53.15013	-27.73994	1.0423	1	V
4495	53.15079	-27.77444	...	4	V	4509	53.15633	-27.86096	0.6891	2	V
4511	53.15730	-27.83373	...	4	V	4520	53.16058	-27.79628	0.4311	3	V
4541	53.16547	-27.91862	0.3654	1	V	4546	53.16687	-27.79883	1.9890	3	V
4548	53.16848	-27.71939	0.4431	2	V	4551	53.17065	-27.74104	...	4	V

Continued from previous page

ID	RA (J2000)	DEC (J2000)	$z_{\rm spec}$	Q	Inst	ID	RA (J2000)	DEC (J2000)	$z_{\rm spec}$	Q	Inst
4559	53.17461	-27.81508	0.6687	1	V	4565	53.17842	-27.94057	0.2870	1	V
4573	53.18173	-27.78310	...	4	V	4582	53.18504	-27.81981	...	4	V
4603	53.19230	-27.95308	...	4	V	4627	53.20524	-27.74352	0.2162	1	V
4631	53.20779	-27.75348	...	4	V	4634	53.20853	-27.76945	...	4	V
4641	53.21513	-27.78760	...	4	V	4645	53.21688	-27.74014	0.5323	1	V
4657	53.23322	-27.82035	...	4	V	4659	53.23384	-27.81114	...	4	V
4690	53.26126	-27.75982	1.1299	3	V	4700	53.26827	-27.93329	...	4	V
4702	53.27042	-27.93085	0.7747	1	V	4708	53.28000	-27.79892	...	4	V
4720	53.29588	-27.79315	...	4	V	4724	53.30804	-27.73991	0.5198	1	V
4725	53.31594	-27.81732	...	4	V	5016	53.40139	-27.74220	1.7071	3	V
9002	52.80250	-27.95507	...	4	V	9012	52.82287	-27.88169	1.2899	1	F
9025	52.86276	-27.99955	...	4	V	9028	52.86883	-27.89516	...	4	M
9030	52.86957	-28.08087	...	4	V	9036	52.88155	-27.96608	...	4	V
9037	52.88650	-27.64013	0.5476	1	V	9050	52.91061	-27.63581	...	4	VF
9066	52.93917	-27.77788	...	4	VF	9073	52.94929	-27.91467	...	4	V
9081	52.95640	-27.86514	1.7983	3	V	9111	53.00557	-28.07789	...	4	V
9140	53.06441	-28.08194	0.4702	3	V	9143	53.06753	-27.65853	1.3260	1	V
9151	53.07764	-27.63497	...	4	V	9156	53.08335	-27.95150	1.0891	1	F
9162	53.09370	-27.82640	0.7301	1	V	9174	53.10289	-27.89291	...	4	F
9175	53.10347	-27.62252	1.8917	3	V	9184	53.11835	-27.98013	...	4	V
9196	53.13400	-28.08540	...	4	V	9200	53.14236	-27.94447	...	4	V
9206	53.15041	-28.02717	...	4	V	9207	53.15066	-27.70640	...	4	V
9214	53.16206	-27.96411	1.2929	1	F	9220	53.17644	-28.07923	...	4	V
9247	53.21523	-27.66033	1.6199	1	VF	9257	53.23653	-27.53502	2.3105	1	V
9259	53.24709	-27.75623	...	4	V	9279	53.28109	-27.85547	...	4	V
9283	53.28990	-27.76295	0.8891	1	F	9297	53.31883	-27.84437	0.0875	1	F
9301	53.32025	-27.99843	0.9326	1	F	9307	53.32413	-27.98507	1.1159	3	F
9308	53.32428	-27.81968	...	4	F	9319	53.35108	-28.02839	0.6244	1	V
9327	53.37622	-27.85153	...	4	V	9332	53.38322	-27.90285	1.3100	1	V
9333	53.38916	-27.75854	0.4198	1	VF	9342	53.42218	-27.63578	0.1019	1	V
9344	53.42657	-27.79366	3.0770	1	V	9345	53.42699	-27.75054	0.7779	1	V
9502	52.80286	-28.02698	0.6769	1	V	9510	52.82622	-27.63835	...	4	V
9576	53.02657	-27.94076	...	4	V	9657	53.21830	-27.69818	...	4	F
9672	53.26867	-28.06087	...	4	F	9694	53.32851	-27.61955	0.8788	2	V
9709	53.38573	-27.59411	0.5228	1	VF	9715	53.41901	-27.77534	0.4192	1	V
10000	52.88223	-27.92262	2.5496	2	M	10001	52.85321	-27.94656	...	4	M
10002	53.03296	-27.87198	...	4	M	10003	53.01181	-27.85067	...	4	M
10004	53.00350	-27.89302	...	4	M	10005	52.96547	-27.85083	...	4	M
10006	53.32332	-27.97592	...	4	M	50004	52.80165	-27.94185	0.6098	1	V
50012	52.80669	-27.75697	...	4	V	50016	52.80819	-27.65298	...	4	V
50018	52.80918	-27.88836	0.7336	1	VF	50028	52.81263	-27.80854	...	4	V
50038	52.82105	-27.92085	...	4	V	50049	52.83069	-27.68748	...	4	V
50052	52.83376	-27.97190	...	4	V	50054	52.83400	-27.65041	0.5258	1	V
50057	52.83598	-27.98355	0.5283	1	V	50064	52.84106	-27.91258	...	4	F
50069	52.84713	-27.81831	0.9665	1	F	50078	52.85379	-27.86898	1.2262	1	F
70066	53.09898	-27.55829	3.1153	1	V	70067	52.92643	-27.96895	3.1766	1	V
70069	53.35564	-28.04622	3.0976	2	V	70072	53.28233	-27.63861	...	4	V
70073	53.08881	-27.60588	3.1094	3	V	70080	53.00912	-27.72860	...	4	V
70087	53.15968	-28.05944	...	4	V	70091	52.82423	-28.05612	...	4	V
70094	52.83208	-28.05489	...	4	V	70096	52.82432	-28.05304	2.7288	1	V
70101	53.03418	-28.04982	...	4	V	70102	53.37338	-28.05033	0.0103	1	V
70106	52.82152	-28.04912	1.8613	2	V	70109	52.82845	-28.04740	...	4	V
70122	53.12305	-28.04243	...	4	V	70127	52.89093	-28.04303	1.9402	2	V
70142	53.37823	-28.03943	...	4	V	70156	53.36756	-28.03603	...	4	V
70158	52.87605	-28.03728	0.1406	1	V	70170	53.37456	-28.03039	...	4	V
70172	53.26571	-28.02956	...	4	V	70173	53.40513	-28.02914	...	4	V
70179	52.85193	-28.02538	2.4114	2	V	70180	52.83001	-28.02435	...	4	V
70181	53.27498	-28.02568	0.1543	1	V	70184	53.35025	-28.02242	1.6795	3	V
70187	52.86084	-28.02244	2.6490	3	V	70190	52.84690	-28.02018	...	4	V
70192	52.83736	-28.01922	0.7429	1	V	70199	53.35595	-28.01584	2.5906	3	V
70200	53.18460	-28.01525	2.9114	3	V	70204	53.40817	-28.01595	1.6065	2	V
70215	52.83119	-28.01213	...	4	V	70216	52.88786	-28.01359	2.5483	1	V
70217	53.22931	-28.01145	...	4	V	70218	53.36554	-28.01231	...	4	V
70219	52.88985	-28.01168	1.7907	3	V	70221	53.17785	-28.01048	...	4	V
70228	53.24893	-28.00426	...	4	V	70232	53.35804	-28.00261	...	4	V
70234	53.26231	-28.00209	...	4	V	70243	53.15216	-28.00061	...	4	V
70252	53.19011	-28.00026	...	4	V	70253	53.25907	-27.99994	...	4	V
70254	52.89604	-28.00111	...	4	V	70262	53.10847	-27.99920	...	4	V
70263	53.16271	-27.99778	...	4	V	70268	53.12748	-27.99602	...	4	V
70269	53.14972	-27.99630	...	4	V	70272	53.17112	-27.99384	...	4	V
70275	53.11254	-27.99296	2.9073	1	V	70278	53.08475	-27.99214	1.9228	1	V
70283	52.92798	-27.98908	2.8933	3	V	70285	53.39533	-27.98761	2.6246	3	V
70285b	53.39521	-27.98854	3.3946	1	V	70290	53.38704	-27.98595	...	4	V
70291	52.96658	-27.98607	...	4	V	70294	53.27430	-27.98538	1.1108	3	V

Continued from previous page

ID	RA (J2000)	DEC (J2000)	$z_{\rm spec}$	Q	Inst	ID	RA (J2000)	DEC (J2000)	$z_{\rm spec}$	Q	Inst
70307	52.96611	-27.98301	...	4	V	70310	52.96677	-27.98049	...	4	V
70318	53.18050	-27.97390	...	4	V	70324	53.23182	-27.97195	...	4	F
70327	53.15372	-27.97196	2.7964	3	V	70334	53.15005	-27.96944	...	4	V
70342	53.38318	-27.96447	...	4	V	70342b	53.38327	-27.96492	1.2144	3	V
70345	53.02701	-27.96350	...	4	V	70347	53.01871	-27.96184	...	4	V
70349	53.10504	-27.96243	0.1243	1	V	70352	53.33956	-27.95954	1.9703	1	VM
70354	53.17649	-27.95782	...	4	V	70355	52.82955	-27.95899	3.2206	2	V
70359	53.02259	-27.95628	2.1182	2	V	70362	53.22939	-27.95591	2.2868	4	V
70363	53.02389	-27.95501	2.0862	2	V	70364	53.25483	-27.95413	...	4	V
70368	53.23909	-27.95224	...	4	V	70370	53.18888	-27.95160	...	4	V
70386	53.20930	-27.94616	...	4	V	70388	53.22236	-27.94424	...	4	V
70390	53.40235	-27.94153	0.1250	1	V	70391	53.23449	-27.94255	0.1765	1	V
70392	53.23668	-27.94147	0.2488	1	V	70398	52.83480	-27.93898	...	4	V
70399	52.96781	-27.93948	2.4451	1	V	70405	53.25415	-27.93790	...	4	V
70408	53.21391	-27.93638	...	4	V	70414	53.08414	-27.93565	2.6797	1	V
70418	53.40896	-27.93361	3.0852	3	V	70419	52.82884	-27.93397	2.9030	2	V
70433	53.25952	-27.92917	0.2766	1	V	70434	53.01946	-27.92973	...	4	V
70434b	53.01973	-27.92889	...	4	V	70435	53.04610	-27.92909	...	4	V
70436	53.37159	-27.92725	...	4	VM	70437	52.83561	-27.92922	0.1690	1	V
70440	53.38409	-27.92515	...	4	M	70442	53.31682	-27.92548	2.1303	1	V
70444	53.26016	-27.92481	...	4	V	70445	52.86209	-27.92634	...	4	V
70449	53.21802	-27.92394	...	4	V	70451	53.38449	-27.92272	2.6466	2	V
70460	53.22810	-27.92052	3.0141	3	V	70464	52.87797	-27.91986	2.3846	2	V
70468	53.36090	-27.91815	...	4	V	70470	53.31589	-27.91922	2.1250	1	V
70471	53.11709	-27.91976	0.1267	1	V	70473	53.22670	-27.91908	...	4	V
70475	53.25737	-27.91835	...	4	V	70479	53.34864	-27.91560	...	4	F
70485	53.12003	-27.91390	...	4	V	70490	53.40470	-27.91013	...	4	V
70492	53.23637	-27.90965	2.9769	2	V	70498	53.41132	-27.90604	1.6256	2	V
70503	53.11270	-27.90449	...	4	V	70504	53.32850	-27.90295	...	4	V
70510	53.33028	-27.89966	...	4	V	70526	53.04141	-27.89401	...	4	V
70527	53.05219	-27.89363	...	4	V	70532	53.36124	-27.89002	...	4	V
70533	53.35981	-27.88816	...	4	M	70536	52.98918	-27.88712	2.0940	2	V
70548	52.87623	-27.88297	...	4	V	70549	52.98314	-27.88319	2.5582	1	V
70550	53.31048	-27.88296	3.1304	1	V	70550b	53.31053	-27.88518	0.4591	3	V
70552	53.33796	-27.88127	...	4	V	70555	53.08207	-27.88193	2.1738	3	V
70557	52.99909	-27.88123	...	4	V	70561	53.34187	-27.87958	...	4	V
70564	53.02874	-27.88215	...	4	V	70568	53.24835	-27.87868	2.5905	1	V
70569	53.41009	-27.87851	...	4	V	70573	53.03264	-27.87786	1.9390	2	V
70574	53.34581	-27.87631	2.8090	1	V	70576	53.23513	-27.87620	...	4	V
70584	52.88640	-27.87687	2.2887	3	V	70587	53.32892	-27.87591	0.0003	1	V
70591	53.05335	-27.87389	0.8205	3	V	70594	53.28186	-27.87322	...	4	V
70599	53.24274	-27.87199	...	4	V	70603	52.87800	-27.87110	...	4	V
70614	53.19738	-27.86879	...	4	V	70620	53.29937	-27.86714	...	4	V
70620b	53.30012	-27.86426	0.3585	1	V	70625	52.90056	-27.86861	...	4	V
70628	52.87962	-27.86702	...	4	V	70630	53.39911	-27.86555	3.1958	2	V
70630b	53.39964	-27.86693	0.2783	1	V	70632	53.00147	-27.86512	...	4	V
70637	52.82569	-27.86283	...	4	V	70641	53.21938	-27.86219	2.8036	2	V
70643	53.36882	-27.86029	...	4	V	70644	53.36601	-27.85946	...	4	V
70647	53.36432	-27.85710	2.5204	2	V	70651	52.84920	-27.85117	...	4	V
70655	53.20830	-27.85142	2.2236	2	V	70657	53.18141	-27.85029	...	4	V
70658	53.28239	-27.84933	...	4	v	70659	53.31235	-27.84795	...	4	V
70661	53.16985	-27.84856	...	4	V	70663	53.35192	-27.84584	...	4	V
70669	53.19384	-27.84427	2.2740	1	V	70671	53.36636	-27.84584	1.8039	3	V
70693	53.24163	-27.84001	0.1213	1	V	70700	52.88937	-27.83749	...	4	V
70701	53.26031	-27.83704	1.1551	3	V	70707	52.86929	-27.83519	...	4	V
70709	52.86362	-27.83479	...	4	V	70711	53.25495	-27.83429	2.3584	3	V
70712	53.24295	-27.83386	2.6424	3	V	70722	53.24029	-27.83205	2.6733	3	V
70725	53.28672	-27.83077	...	4	V	70728	53.00274	-27.83141	...	4	V
70738	53.39269	-27.82592	2.7586	2	V	70746	52.87638	-27.82433	...	4	V
70747	52.93657	-27.82375	2.1777	1	V	70756	52.89125	-27.82133	...	4	V
70757	53.27701	-27.82071	...	4	V	70759	52.95150	-27.82152	...	4	V
70761	52.95928	-27.82039	2.3336	2	V	70764	52.96930	-27.81834	...	4	V
70766	52.95591	-27.81812	...	4	V	70766b	52.95604	-27.81864	...	4	V
70768	52.85592	-27.81257	...	4	V	70769	52.87739	-27.81261	...	4	V
70771	53.21848	-27.81157	2.8594	2	V	70776	53.02806	-27.81099	...	4	V
70778	53.07980	-27.80988	...	4	V	70779	52.86086	-27.80920	...	4	V
70784	53.07073	-27.80739	2.4417	3	V	70789	52.85772	-27.80472	...	4	V
70799	52.82538	-27.80277	...	4	F	70804	52.81952	-27.80144	...	4	V
70805	53.23839	-27.80125	...	4	V	70806	53.35464	-27.80027	...	4	V
70809	52.82646	-27.80066	...	4	V	70814	52.88865	-27.79851	...	4	V
70817	52.88963	-27.79712	...	4	V	70818	53.05218	-27.79749	...	4	V
70828	53.03998	-27.79438	...	4	V	70833	53.22440	-27.79320	...	4	V
70834	53.00766	-27.79380	0.1697	2	V	70838	53.34703	-27.79555	0.1252	1	V
70840	52.95536	-27.79277	...	4	V	70841	53.09800	-27.79157	2.6869	2	V

Continued from previous page

ID	RA (J2000)	DEC (J2000)	$z_{\rm spec}$	Q	Inst	ID	RA (J2000)	DEC (J2000)	$z_{\rm spec}$	Q	Inst
70842	52.99857	-27.79080	...	4	V	70844	52.99791	-27.79083	...	4	V
70846	53.24852	-27.79065	2.8179	2	V	70848	53.14924	-27.78853	...	4	V
70849	53.11568	-27.78761	0.8779	3	V	70851	53.39582	-27.78571	2.4154	3	V
70853	53.19225	-27.78600	...	4	V	70853b	53.19213	-27.78715	1.0939	2	V
70857	53.17712	-27.78406	...	4	V	70859	53.18235	-27.78334	...	4	V
70864	52.87473	-27.78145	0.5217	3	V	70866	53.26264	-27.78053	...	4	V
70869	53.31576	-27.78060	...	4	V	70871	53.25666	-27.77899	2.6937	2	V
70873	52.86424	-27.77902	...	4	V	70875	53.35321	-27.77754	...	4	V
70877	53.35411	-27.77788	...	4	V	70879	53.11357	-27.77745	1.8796	2	V
70882	52.85897	-27.77517	...	4	V	70883	53.27437	-27.77506	...	4	V
70886	52.86699	-27.77388	...	4	V	70888	53.22624	-27.77278	...	4	V
70889	53.10347	-27.77468	0.0006	1	V	70891	53.07133	-27.77188	2.4310	3	V
70822	52.83239	-27.79613	...	4	V	70898	52.83983	-27.77029	...	4	V
70900	53.21570	-27.76899	...	4	V	70901	52.95030	-27.76971	...	4	V
70903	52.95859	-27.76973	...	4	V	70904	52.89893	-27.77063	...	4	V
70906	53.26016	-27.76907	...	4	V	70910	53.04916	-27.76797	...	4	V
70914	53.22890	-27.76962	1.8875	1	V	70917	53.19537	-27.76793	2.8718	1	V
70920	53.04627	-27.76730	...	4	V	70921	52.88225	-27.76699	...	4	V
70927	52.82226	-27.76544	...	4	V	70933	52.88385	-27.76390	2.6086	3	V
70934	52.88548	-27.76258	...	4	V	70936	52.90439	-27.76225	2.8312	3	V
70938	53.18591	-27.76007	2.6243	1	V	70941	53.17352	-27.75712	...	4	V
70942	52.85590	-27.75733	...	4	V	70944	53.29330	-27.75633	2.6876	1	V
70948	52.84347	-27.75579	...	4	V	70949	53.34078	-27.75364	...	4	V
70950	52.97150	-27.75430	...	4	V	70952	53.17128	-27.75748	0.1048	1	V
70953	53.19066	-27.75431	...	4	V	70955	53.33660	-27.75210	...	4	V
70957	52.87317	-27.75098	...	4	V	70958	52.94510	-27.74988	...	4	V
70959	52.87676	-27.74974	...	4	V	70967	52.98810	-27.74129	...	4	V
70970	53.13954	-27.74178	0.1484	1	V	70974	53.22247	-27.73792	...	4	V
70976	53.23451	-27.73765	0.1232	1	V	70984	52.91180	-27.73605	2.3447	2	V
70989	53.32547	-27.73350	...	4	V	70993	53.23909	-27.73270	...	4	V
70994	52.88593	-27.73295	...	4	V	70994b	52.88596	-27.73126	0.4144	2	V
70994c	52.88612	-27.72979	...	4	V	70997	53.34114	-27.73030	...	4	V
70999	52.83665	-27.73033	...	4	V	70999b	52.83688	-27.72831	...	4	V
71005	53.14442	-27.72802	...	4	V	71006	53.14073	-27.72760	...	4	V
71009	52.98011	-27.72777	...	4	V	71011	53.02517	-27.72711	...	4	V
71012	53.15719	-27.72683	...	4	V	71013	53.40902	-27.72625	...	4	V
71024	53.39800	-27.72426	...	4	V	71028	53.12100	-27.72469	...	4	V
71029a	52.82912	-27.72787	0.2760	1	V	71029b	52.82881	-27.72747	...	4	V
71038	53.17883	-27.71689	...	4	V	71043	53.38353	-27.71478	...	4	V
71045	53.38845	-27.71362	...	4	V	71046	52.97019	-27.71438	...	4	V
71047	53.36180	-27.71399	2.3195	3	V	71048	52.97800	-27.71442	...	4	V
71054	53.16605	-27.71213	...	4	V	71056	53.33438	-27.71227	2.7406	1	V
71060	53.36596	-27.71105	...	4	V	71062	52.99693	-27.71272	0.1041	1	V
71063	52.99964	-27.70983	...	4	V	71065	53.01319	-27.70683	...	4	V
71067	52.89440	-27.70715	0.0953	1	V	71072	53.03367	-27.70509	...	4	V
71080	53.06226	-27.70117	...	4	V	71083	53.10868	-27.70005	2.4391	1	V
71084	53.35408	-27.69952	3.4769	2	V	71093	53.15372	-27.69286	2.4300	4	V
71096b	53.14331	-27.69082	...	4	V	71098	53.15749	-27.69054	...	4	V
71100	53.05050	-27.68847	...	4	V	71103	53.26706	-27.68913	0.1275	1	V
71104	53.05224	-27.68724	...	4	V	71109	53.26567	-27.68811	1.0000e-6	1	V
71116	53.14353	-27.68354	2.4187	3	V	71126	52.82160	-27.68258	2.4405	3	V
71127	52.90979	-27.68217	...	4	V	71130	53.15832	-27.68087	...	4	V
71131	53.38105	-27.68579	...	4	V	71133	52.83224	-27.68165	...	4	V
71134	52.83276	-27.68089	...	4	V	71142	52.88322	-27.67781	...	4	V
71144	53.14522	-27.67885	...	4	V	71150	53.40756	-27.67671	...	4	V
71153	53.40908	-27.67569	0.1036	1	V	71154	53.33395	-27.67517	...	4	V
71162	53.33701	-27.67345	2.3532	2	V	71167	52.92889	-27.67404	...	4	V
71169	52.94548	-27.67298	...	4	V	71170	53.06285	-27.67233	...	4	V
71179	53.33800	-27.67050	...	4	V	71182	53.05948	-27.66988	...	4	V
71184	53.33034	-27.66868	2.2124	1	V	71190	53.06749	-27.66956	...	4	V
71194	52.82717	-27.66398	...	4	V	71196	52.84449	-27.66053	2.3524	3	V
71202	53.21168	-27.65569	...	4	V	71204	53.01702	-27.65533	...	4	V
71205	53.29680	-27.65502	...	4	F	71207	53.29255	-27.65318	...	4	V
71212	53.21175	-27.65208	...	4	V	71213	53.26239	-27.65168	...	4	V
71213b	53.26247	-27.65227	0.1071	1	V	71214	52.99720	-27.65209	...	4	V
71223	52.99036	-27.65115	...	4	V	71228	53.18684	-27.64859	2.5163	4	V
71229	52.97575	-27.64900	2.3083	1	V	71231	53.01896	-27.64574	...	4	V
71234	53.38731	-27.64376	...	4	V	71235	53.02618	-27.64445	...	4	V
71236	53.14992	-27.64373	...	4	V	71240	53.36631	-27.64024	...	4	V
71255	53.02472	-27.63728	...	4	V	71261	53.14433	-27.63273	1.9748	1	V
71265	53.14593	-27.62973	...	4	V	71266	53.20312	-27.62968	...	4	V
71268	53.20011	-27.62911	...	4	V	71269	52.96389	-27.62951	...	4	V
71271	53.14864	-27.62796	...	4	V	71277	52.94286	-27.62715	2.1979	2	V
71280	52.93961	-27.62404	...	4	V	71283	52.83249	-27.62271	...	4	V

Continued from previous page

ID	RA (J2000)	DEC (J2000)	$z_{\rm spec}$	Q	Inst	ID	RA (J2000)	DEC (J2000)	$z_{\rm spec}$	Q	Inst
71284	52.95160	-27.62210	...	4	V	71288	53.38067	-27.62070	...	4	V
71289	53.36185	-27.61886	...	4	V	71291	52.86072	-27.61995	...	4	V
71292	52.95415	-27.61982	...	4	V	71293	52.85659	-27.61842	...	4	V
71297	52.84274	-27.61812	...	4	V	71305	52.85186	-27.61708	...	4	V
71312	52.96553	-27.61564	...	4	V	71314	53.00826	-27.61517	...	4	V
71317	52.84061	-27.61417	...	4	V	71320	52.94809	-27.61335	...	4	V
71321	52.86018	-27.61389	...	4	V	71323	52.99465	-27.61355	...	4	V
71329	52.96434	-27.61312	...	4	V	71330	52.97359	-27.61455	...	4	V
71332	52.85824	-27.61460	...	4	V	71340	53.17614	-27.61284	0.1029	1	V
71341	53.18075	-27.61147	...	4	V	71343	53.14756	-27.61252	2.3677	1	V
71348	52.88584	-27.61058	...	4	V	71349	53.13642	-27.61213	...	4	V
71349b	53.13633	-27.61039	0.5234	1	V	71352	53.15603	-27.60929	...	4	V
71353	53.12600	-27.60925	...	4	V	71354	53.09984	-27.60878	...	4	V
71357	52.88933	-27.60864	2.2665	2	V	71358	53.37166	-27.60791	2.7040	2	V
71360	53.04730	-27.60757	...	4	V	71362	53.38520	-27.60678	...	4	VF
71366	53.05007	-27.60710	...	4	V	71367	53.41112	-27.60504	2.4620	2	V
71368	53.34554	-27.60494	...	4	V	71369	53.40870	-27.60515	...	4	V
71370	52.87955	-27.60550	...	4	V	71375	52.96663	-27.60362	...	4	V
71376	53.35872	-27.60235	...	4	V	71379	52.97346	-27.60308	0.8846	3	V
71381	52.95732	-27.60287	...	4	V	71384	52.92542	-27.60217	...	4	V
71386	52.94649	-27.60228	...	4	V	71388	52.93804	-27.60131	...	4	V
71391	52.86853	-27.60145	...	4	V	71392	52.91498	-27.60053	...	4	V
71393	53.17919	-27.60094	...	4	V	71394	53.09024	-27.60011	...	4	V
71395	52.87990	-27.60355	0.2287	1	V	71396	52.90145	-27.60013	...	4	V
71399	52.94619	-27.59951	2.2452	1	V	71401	52.95885	-27.59923	2.1698	1	V
71402	53.24951	-27.59853	...	4	V	71403	52.94130	-27.59879	...	4	V
71405	53.23375	-27.59858	...	4	V	71406	53.05901	-27.59770	...	4	V
71407	53.07639	-27.59739	...	4	V	71409	53.22121	-27.59623	2.3195	1	V
71410	53.28544	-27.59513	1.7478	2	V	71412	53.22648	-27.59575	...	4	V
71414	53.05956	-27.59485	...	4	V	71423	53.04031	-27.59509	0.1486	1	V
71429	52.82285	-27.59064	...	4	V	71430	53.26782	-27.58942	...	4	V
71435	53.39829	-27.58917	...	4	V	71437	53.19364	-27.58892	...	4	V
71442	53.40073	-27.58642	...	4	V	71444	53.08759	-27.58686	...	4	V
71446	53.40802	-27.58482	...	4	V	71447	53.38314	-27.58417	...	4	V
71448	53.06594	-27.58430	...	4	V	71449	52.95904	-27.58420	2.2665	2	V
71452	53.06377	-27.58505	...	4	V	71453	53.27688	-27.58333	...	4	V
71459	52.97973	-27.58135	...	4	V	71463	52.97525	-27.58087	...	4	V
71470	52.99065	-27.57839	2.4069	2	V	71474	52.85022	-27.57854	...	4	V
71477	53.03304	-27.57879	2.4428	3	V	71478	53.39721	-27.57827	0.2976	1	V
71483	53.08930	-27.58039	0.1469	1	V	71485	52.87323	-27.58040	0.2974	1	V
71495	53.16770	-27.57645	...	4	V	71499	52.97639	-27.57319	...	4	V
71501	53.02444	-27.57305	2.4277	3	V	71502	52.99207	-27.57165	2.0507	3	V
71510	53.08369	-27.57000	...	4	V	71511	53.10571	-27.57126	...	4	V
71515	53.39919	-27.56902	...	4	V	71517	53.15446	-27.56955	...	4	V
71518	53.39618	-27.56793	...	4	V	71521	53.09806	-27.56862	0.2179	1	V
71532	52.99641	-27.57031	0.1254	1	V	71533	53.29050	-27.56371	...	4	V
71534	53.20628	-27.56712	0.6871	1	V	71535	53.39240	-27.56376	...	4	V
71537	53.40607	-27.56300	...	4	V	71539	52.94628	-27.56322	2.3623	3	V
71541	52.95511	-27.56214	...	4	V	71542	53.39873	-27.56135	...	4	V
71551	53.06594	-27.55892	...	4	V	71557	53.36280	-27.55701	...	4	V
71575	53.15718	-27.55541	...	4	V	71578	53.09242	-27.55489	...	4	V
71581	53.16133	-27.55536	0.2132	1	V	71582	53.18348	-27.55398	...	4	V
71586	53.36892	-27.55285	2.1481	2	V	71600	53.38266	-27.55075	...	4	V
71605	52.97773	-27.55000	...	4	V	71607	52.92560	-27.54946	...	4	V
71608	52.92824	-27.55177	...	4	V	71609	53.19318	-27.54883	...	4	V
71614	53.13916	-27.54544	...	4	V	71618	52.98850	-27.54068	2.5743	1	V
71619	53.20410	-27.53831	...	4	V	71626	53.32518	-27.54662	2.6691	3	V
71631	52.96761	-27.54790	...	4	V	71634	52.96974	-27.54765	...	4	V
71635	53.11893	-27.53750	...	4	V	71636	53.06692	-27.54095	2.3493	1	V
71653	52.94959	-27.53893	...	4	V	71658	52.91355	-27.53921	...	4	V
71666	53.40644	-27.54071	...	4	V	71668	53.07216	-27.53795	...	4	V
71669	53.28392	-27.53766	...	4	V	71671	53.40950	-27.53737	2.3322	1	V
71671b	53.40959	-27.53876	0.3961	1	V	71671c	53.40959	-27.54074	...	4	V
71671d	53.40950	-27.53539	...	4	V	71672	53.28002	-27.54541	...	4	V
71683	52.99280	-27.54648	...	4	V	71685	53.12145	-27.54055	...	4	V
71691	53.35232	-27.53583	0.7918	3	V	71705	53.30144	-28.05164	3.0777	2	V
71707	52.82340	-28.05043	...	4	V	71712	53.36567	-28.04267	2.8677	3	V
71715	52.89160	-28.03976	2.8563	2	V	71726	53.19563	-28.01523	...	4	V
71732	53.25782	-28.00222	...	4	V	71734	52.93021	-27.97198	...	4	V
71740	53.39015	-27.96241	2.9511	1	V	71741	53.01481	-27.95865	...	4	V
71743	53.20747	-27.94093	...	4	VF	71745	53.06668	-27.93771	...	4	F
71748	53.24783	-27.93303	...	4	V	71751	53.37649	-27.92499	2.2445	3	M
71759	53.20579	-27.89986	...	4	V	71761	53.09334	-27.88706	...	4	V
71765	53.01058	-27.88275	...	4	F	71766	53.05473	-27.88039	...	4	V
71769	53.17813	-27.87934	...	4	V	71777	52.95416	-27.86941	...	4	V

Continued from previous page

ID	RA (J2000)	DEC (J2000)	$z_{\rm spec}$	Q	Inst	ID	RA (J2000)	DEC (J2000)	$z_{\rm spec}$	Q	Inst
71782	53.11161	-27.86280	...	4	F	71786	53.24135	-27.84420	2.6399	3	V
71790	53.32685	-27.84082	...	3	VF	71797	53.20538	-27.83389	...	4	V
71802	53.39692	-27.82948	...	4	V	71809	52.85119	-27.80685	...	4	F
71814	53.34378	-27.79385	2.7316	3	V	71818	53.29178	-27.78863	3.3508	1	V
71831	53.17894	-27.75283	...	4	V	71832	53.14015	-27.75112	...	4	V
71837	52.87014	-27.73085	...	4	V	71838	53.33099	-27.73006	...	4	V
71844	53.01252	-27.72471	...	4	V	71845	53.19991	-27.71656	...	4	V
71852	53.16188	-27.69559	...	4	V	71853	53.35997	-27.68655	...	4	F
71857	53.08138	-27.68363	...	4	V	71860	52.92031	-27.67052	...	4	V
71862	53.21816	-27.67058	...	4	V	71869	53.22303	-27.65025	...	4	F
71874	52.95195	-27.61802	...	4	VF	71876	53.18199	-27.61729	2.6983	2	V
71876b	53.18200	-27.61647	2.6983	2	V	71877	52.97545	-27.61659	...	4	V
71881	53.17833	-27.61256	...	4	F	71886	52.87773	-27.60715	0.4463	2	V
71888	53.17115	-27.60382	...	4	F	71895	53.38312	-27.58315	0.8791	2	F
71896	53.40687	-27.58168	...	4	V	71897	53.00758	-27.58071	...	4	F
71900	52.99490	-27.57519	2.9974	1	V	71901	53.40860	-27.56815	...	4	VF
71905	52.95682	-27.56403	...	4	V	71910	53.34171	-27.55140	...	4	F
71913	53.20503	-27.53735	...	4	F	71920	53.06769	-27.53909	3.1540	2	V
71925	53.18413	-27.54410	...	4	F	71926	53.35226	-27.54499	3.1256	1	V
71927	53.19080	-27.54749	...	4	V	90001	53.12273	-27.92208	...	4	V
90004	53.12514	-27.90115	...	4	V	90006	53.15375	-27.89444	...	4	V
90015	53.12094	-27.88429	...	4	V	90020	53.16547	-27.88140	...	4	V
90029	53.20322	-27.87523	...	4	V	90030	53.05841	-27.87502	...	4	V
90031	53.24737	-27.87426	...	4	V	90038	53.19806	-27.87190	...	4	V
90039	53.11205	-27.87103	...	4	V	90040	53.24553	-27.87077	...	4	V
90042	53.17916	-27.87049	...	4	V	90053	53.22084	-27.86495	...	4	V
90054	53.16052	-27.86498	...	4	V	90056	53.22268	-27.85876	...	4	V
90058	53.24516	-27.85505	2.6728	2	V	90062	53.15765	-27.84991	...	4	V
90063	53.12563	-27.84930	...	4	V	90076	53.18525	-27.83742	...	4	V
90078	53.19116	-27.83380	...	4	V	90087	53.05410	-27.80938	...	4	V
90089	53.21439	-27.80768	...	4	V	90093	53.21203	-27.80549	...	4	V
90095	53.20473	-27.80328	...	4	V	90106	53.13781	-27.79554	...	4	V
90110	53.14800	-27.79290	...	4	V	90114	53.21546	-27.77883	...	4	V
90118	53.03598	-27.77004	...	4	V	90119	53.20360	-27.76742	...	4	V
90120	53.19649	-27.76667	...	4	V	90121	53.02562	-27.76615	3.8015	3	V
90123	53.18938	-27.75769	...	4	V	90124	53.19361	-27.75560	...	4	V
90125	53.07533	-27.75526	...	4	V	90126	53.18465	-27.75472	4.0567	2	V
90129	53.07489	-27.75348	...	4	V	90132	53.13060	-27.75102	...	4	V
90135	53.05808	-27.74099	...	4	V	90136	53.19213	-27.74093	...	4	V
90137	53.16890	-27.74004	...	4	V	90138	53.18467	-27.73870	...	4	V
90139	53.06475	-27.73723	...	4	V	90140	53.03079	-27.73488	3.4988	1	V
90144	53.06483	-27.72653	...	4	V	90145	53.06760	-27.72658	...	4	V
90148	53.15791	-27.72504	...	4	V	90149	53.06844	-27.72463	...	4	V
90150	53.08058	-27.72084	...	4	V	90151	53.07385	-27.71815	...	4	V
90154	53.15842	-27.69954	...	4	V	90157	53.16354	-27.69650	...	4	V
90159	53.13432	-27.69431	3.4645	1	V	90164	53.15287	-27.68685	3.7384	1	V
9992817	52.89323	-28.02985	...	4	V	9993329	53.24806	-28.02328	1.7395	1	F
9993551	53.24861	-28.02079	...	4	F	99944000	53.23748	-27.56208	2.1235	1	V
90157b	53.07606	-27.86536	0.7643	1	V	90164b	53.15287	-27.68725	0.6661	1	V
80000	52.99229	-28.03573	...	4	F	80001	53.03228	-28.02677	...	4	F
80002	53.02890	-28.01001	...	4	F	80003	53.02907	-28.00949	...	4	F
80004	53.03629	-28.00459	...	4	F	80005	53.00008	-27.99712	0.7556	2	F
80006	53.06559	-27.99233	...	4	F	80008	53.06730	-27.98417	...	4	F
80009	53.00032	-27.97803	...	4	F	80010	53.05518	-27.96452	0.6236	1	F
80011	53.07827	-27.96294	...	4	F	80011b	53.07848	-27.96220	...	4	F
80012	53.03062	-27.95609	...	4	F	80013	53.06269	-27.95413	...	4	F
80014	53.03169	-27.94255	...	4	F	80016	53.08918	-27.93030	...	4	F
80017	53.05376	-27.92867	...	4	F	80017b	53.05359	-27.92804	...	4	F
80018	53.08620	-27.92670	...	4	F	80019	53.04334	-27.92148	...	4	F
80020	52.93591	-28.01428	...	4	F	80021	52.90567	-28.01153	1.2136	1	F
80022	52.94616	-28.00931	1.3946	1	F	80023	52.89021	-28.00597	...	4	F
80024	52.88400	-28.00189	1.5942	1	F	80025	52.89408	-27.99788	...	4	F
80026	52.87804	-27.98920	3.8737	2	F	80027	52.87065	-27.98809	...	4	F
80028	52.87586	-27.98631	1.2882	2	F	80029	52.86956	-27.98408	0.7517	1	F
80030	52.86431	-27.98026	0.9815	2	F	80031	52.85848	-27.97718	...	4	F
80032	52.89883	-27.97534	1.0177	1	F	80033	52.91256	-27.97378	...	4	F
80034	52.89602	-27.97196	...	4	F	80036	52.88372	-27.95049	0.9833	1	F
80037	52.88133	-27.94708	...	4	F	80038	52.92141	-27.93243	1.1194	2	F
80039	52.91395	-27.92454	...	4	F	80040	52.87660	-27.92193	1.5340	1	F
80041	52.90495	-27.91589	...	4	F	80042	52.87111	-27.90773	1.3660	1	F
80043	52.88840	-27.90643	...	4	F	80044	52.89490	-27.90412	...	4	F
80045	52.89121	-27.90161	...	4	F	80047	52.84112	-27.91318	...	4	F
80048	52.83894	-27.91118	0.2886	1	F	80049	52.83886	-27.91047	2.8949	3	F
80050	52.83860	-27.90973	...	4	F	80053	52.86316	-27.89725	0.7754	1	F

Continued from previous page

ID	RA (J2000)	DEC (J2000)	$z_{\rm spec}$	Q	Inst	ID	RA (J2000)	DEC (J2000)	$z_{\rm spec}$	Q	Inst
80054	52.85166	-27.89635	...	4	F	80055	52.85070	-27.89491	...	4	F
80056	52.84940	-27.89153	0.6556	1	F	80057	52.80917	-27.88736	...	4	F
80058	52.80917	-27.88886	...	4	F	80059	52.87740	-27.86366	...	4	F
80060	52.87740	-27.86277	...	4	F	80063	52.84099	-27.85882	0.7106	1	F
80064	52.84100	-27.85704	1.0166	1	F	80065	52.82632	-27.85384	...	4	F
80066	52.82498	-27.85154	...	4	F	80067	52.85166	-27.84332	0.5327	1	F
80068	52.84731	-27.81937	...	4	F	80069	52.82979	-27.81565	1.3150	1	F
80070	52.80829	-27.80905	1.2185	1	F	80072	53.02203	-27.92903	...	4	F
80073	52.98198	-27.92712	0.8142	1	F	80075	53.01194	-27.90775	...	4	F
80076	53.02150	-27.90040	0.8460	1	F	80077	52.98247	-27.89805	...	4	F
80079	53.04070	-27.88733	0.7398	1	F	80080	52.96384	-27.88470	...	4	F
80081	53.01057	-27.87526	0.7328	1	F	80082	53.01107	-27.87511	...	4	F
80084	53.03824	-27.86286	...	4	F	80087	53.01826	-27.84900	...	4	F
80088	52.99276	-27.84538	...	4	F	80091	52.99787	-27.83930	1.5786	1	F
80092	53.00140	-27.83767	...	4	F	80093	53.02940	-27.82993	...	4	F
80094	53.03702	-27.81895	...	4	F	80095	52.98612	-27.81609	...	4	F
80096	53.00331	-27.81452	...	4	F	80097	53.03366	-27.81198	...	4	F
80100	53.36943	-27.98167	...	4	F	80101	53.32138	-27.97796	1.0459	2	F
80102	53.32186	-27.97225	4.2417	1	F	80103	53.33830	-27.96901	...	4	F
80104	53.37104	-27.96661	...	4	F	80105	53.36415	-27.96522	...	4	F
80106	53.36432	-27.96440	...	4	F	80107	53.36448	-27.96396	...	4	F
80108	53.35532	-27.96206	0.8037	1	F	80109	53.32493	-27.93946	4.6785	1	F
80110	53.34655	-27.92886	...	4	F	80111	53.36248	-27.92629	...	4	F
80112	53.34492	-27.92086	...	4	F	80113	53.34508	-27.91885	...	4	F
80114	53.34886	-27.91832	...	4	F	80115	53.32332	-27.91217	...	4	F
80116	53.32867	-27.90755	0.5777	1	F	80117	53.32497	-27.90549	...	4	F
80118	53.32226	-27.89986	1.1364	1	F	80119	52.92767	-27.81915	0.9654	1	F
80120	52.92868	-27.81662	...	4	F	80122	52.96959	-27.80623	...	4	F
80123	52.94000	-27.80327	...	4	F	80126	52.94804	-27.79155	...	4	F
80127	52.91820	-27.78228	1.1274	1	F	80128	52.92071	-27.77984	1.0354	1	F
80129	52.94879	-27.77427	1.0953	2	F	80132	52.94049	-27.75521	...	4	F
80133	52.99078	-27.75334	...	4	F	80134	52.92155	-27.74995	...	4	F
80135	52.97895	-27.73562	1.3626	1	F	80139	52.97265	-27.71048	...	4	F
80140	52.93688	-27.70760	1.0411	3	F	80141	52.93529	-27.70285	...	4	F
80142	52.88829	-27.70937	...	4	F	80143	52.94166	-27.69529	...	4	F
80144	52.88629	-27.68490	...	4	F	80145	52.93294	-27.66584	1.0341	1	F
80147	52.91000	-27.64700	...	4	F	80148	52.93327	-27.64107	0.9758	1	F
80149	52.92331	-27.63380	4.0404	1	F	80150	52.92323	-27.63277	...	4	F
80151	52.91352	-27.63113	1.4266	1	F	80152	52.90297	-27.62906	...	4	F
80153	52.90883	-27.62201	0.8319	1	F	80155	52.93612	-27.61645	...	4	F
80156	52.94784	-27.61111	1.5751	1	F	80157	52.94767	-27.60970	1.4765	3	F
80158	53.40264	-27.74401	1.4564	3	F	80159	53.36592	-27.73864	0.9683	1	F
80160	53.40419	-27.73414	...	4	F	80161	53.37115	-27.72602	0.4577	1	F
80162	53.37089	-27.72446	...	4	F	80163	53.37105	-27.72283	...	4	F
80164	53.38283	-27.71537	...	4	F	80165	53.37193	-27.71177	...	4	F
80166	53.38907	-27.70415	...	4	F	80168	53.38576	-27.69541	...	4	F
80169	53.38227	-27.68111	0.7440	1	F	80170	53.38235	-27.68022	...	4	F
80171	53.37053	-27.67877	2.1693	1	F	80172	53.39629	-27.66994	...	4	F
80173	53.37124	-27.66765	0.2884	1	F	80174	53.36853	-27.66091	...	4	F
80175	53.40174	-27.65301	1.0281	1	F	80176	53.40415	-27.64766	...	4	F
80184	52.88922	-27.96755	1.0328	1	F	80188	52.86799	-27.92949	...	4	F
80191	53.12346	-27.94286	...	4	F	80192	53.14395	-27.94847	...	4	F
80194	53.07516	-27.93068	...	4	F	80195	53.05501	-27.92462	1.1830	1	F
80196	53.12619	-27.92194	...	4	F	80197	53.06163	-27.91735	...	4	F
80198	53.08664	-27.91131	...	4	VF	80201	53.05045	-27.89822	...	4	F
80202	53.05036	-27.89741	0.8913	3	F	80203	53.08771	-27.89655	...	4	F
80204	53.12420	-27.88968	0.8947	1	F	80205	53.05371	-27.88658	...	4	F
80207	53.06058	-27.88219	...	4	F	80209	53.06905	-27.87863	1.0445	1	F
80211	53.08916	-27.85724	...	4	F	80213	53.07504	-27.84228	0.5613	1	F
80217	52.94024	-27.76893	...	4	F	80220	52.94526	-27.73356	...	4	F
80221	52.96688	-27.72205	4.5233	1	F	80222	53.28446	-27.73435	...	4	F
80223	53.28479	-27.73368	...	4	F	80224	53.21297	-27.73066	...	4	F
80225	53.21903	-27.71011	0.9422	1	F	80226	53.27629	-27.69647	...	4	F
80227	53.27368	-27.69225	...	4	F	80228	53.20959	-27.68795	2.9726	1	V
80229	53.22768	-27.68554	...	4	F	80230	53.24845	-27.68460	...	4	F
80231	53.25672	-27.67932	...	4	F	80232	53.25947	-27.67323	...	4	F
80233	53.29730	-27.66668	...	4	F	80234	53.22450	-27.65721	...	4	F
80235	53.21821	-27.65233	...	4	F	80236	53.21812	-27.65166	...	4	F
80237	53.24109	-27.63218	...	4	F	80238	53.26704	-27.63042	...	4	F
80239	52.98174	-27.62000	...	4	F	80240	52.94122	-27.61348	...	4	F
80241	53.02617	-27.60328	...	4	F	80243	52.95520	-27.59479	...	4	F
80244	52.99227	-27.58995	0.6712	1	F	80245	52.99168	-27.58743	0.4896	1	F
80247	52.95026	-27.58226	...	4	F	80248	53.00766	-27.58001	0.7278	1	F
80249	53.00228	-27.54975	...	4	F	80250	52.96396	-27.54161	...	4	F

Continued from previous page

ID	RA (J2000)	DEC (J2000)	z_{spec}	Q	Inst	ID	RA (J2000)	DEC (J2000)	z_{spec}	Q	Inst
80251	53.01286	-27.60129	0.9613	1	F	80252	53.22737	-28.02640	...	4	F
80253	53.19129	-28.01305	...	4	F	80254	53.20653	-27.99166	...	4	F
80255	53.24130	-27.99018	...	4	F	80256	53.19702	-27.98597	...	4	F
80257	53.19366	-27.98353	1.1715	3	F	80258	53.25939	-27.97560	0.1470	1	F
80259	53.17951	-27.96917	0.6702	1	F	80260	53.18428	-27.96234	1.0899	1	F
80261	53.21920	-27.95819	...	4	F	80262	53.24690	-27.95538	...	4	F
80263	53.24945	-27.93736	...	4	F	80264	53.21696	-27.93468	...	4	F
80265	53.22568	-27.93244	...	4	F	80266	53.22559	-27.93155	...	4	F
80267	53.18383	-27.91458	...	4	F	80268	53.21595	-27.62185	...	4	F
80269	53.18221	-27.61799	0.6943	1	F	80270	53.21434	-27.61518	...	4	F
80271	53.17351	-27.58552	...	4	F	80273	53.18939	-27.57897	1.4300	2	F
80274	53.16437	-27.57545	1.1877	2	F	80275	53.16453	-27.57352	1.1877	1	F
80276	53.18368	-27.56815	...	4	F	80277	53.21462	-27.56282	...	4	F
80278	53.21324	-27.54540	...	4	F	80279	53.21707	-27.53923	...	4	F
80280	53.15834	-27.53489	0.5021	1	F	80281	53.17274	-27.52417	0.7013	1	F
80282	53.19068	-27.51316	0.8920	1	F	80283	53.21661	-27.51056	0.3833	1	F
80284	53.18823	-27.92584	...	4	F	80285	53.32245	-27.85870	...	4	F
80286	53.32001	-27.85618	...	4	F	80288	53.30954	-27.83686	...	4	F
80289	53.26550	-27.83408	0.8033	1	F	80290	53.30415	-27.83175	...	4	F
80291	53.34062	-27.82735	...	4	F	80292	53.27737	-27.79808	...	4	F
80294	53.31809	-27.79026	0.9826	1	F	80295	53.28848	-27.78603	4.0170	2	F
80296	53.26224	-27.78425	...	4	F	80297	53.29299	-27.77868	...	4	F
80298	53.32423	-27.77229	0.9823	3	F	80299	53.28335	-27.75342	...	4	F
80505	53.31701	-28.02529	...	4	F	80506	53.24376	-28.02815	1.1238	1	F
80507	53.22992	-28.03728	...	4	F	80508	53.28845	-28.04310	0.2712	3	F
80509	53.28758	-28.05056	0.4080	1	F	80510	53.28873	-28.06291	0.6625	1	F
80511	53.25310	-28.06573	1.0309	1	F	80512	53.25287	-28.06634	0.9749	2	F
80513	53.25247	-28.07132	...	4	F	80514	53.26717	-28.07368	1.0205	1	F
80515	53.22899	-28.07711	0.8111	1	F	80516	53.22922	-28.07842	0.7019	1	F
80517	53.29434	-28.08024	1.0454	1	F	80519	53.23547	-28.09377	0.6692	1	F
80520	53.23021	-28.09518	...	4	F	80521	53.32198	-28.09761	...	4	F
80522	53.28599	-28.10145	0.6192	1	F	80523	53.28610	-28.10246	0.7817	1	F
80524	53.28725	-28.10689	1.4218	3	F	80525	53.38842	-27.51744	1.3327	1	F
80526	53.39663	-27.51982	1.1401	1	F	80527	53.39347	-27.52542	0.2434	1	F
80528	53.39347	-27.52584	1.3310	2	F	80529	53.39363	-27.52668	1.1768	1	F
80530	53.40358	-27.53074	...	4	F	80531	53.37422	-27.53480	0.7694	1	F
80532	53.37422	-27.53536	...	4	F	80533	53.33838	-27.53731	...	4	F
80534	53.40243	-27.54176	...	4	F	80535	53.39587	-27.55424	4.0440	1	F
80536	53.36881	-27.56331	2.1933	1	F	80538	53.38777	-27.57726	...	4	F
80539	53.34873	-27.58606	...	4	F	80540	53.40883	-27.59017	5.5012	2	F
80541	53.39901	-27.60244	1.0090	3	F	80542	53.36872	-27.60469	0.4229	1	F
80543	53.35571	-27.61526	...	4	F	80544	53.39265	-27.62197	...	4	F
80545	53.39719	-27.62759	...	4	F	80546	53.38046	-27.62987	0.7561	3	F
80600	52.95930	-27.61058	4.2622	3	F	82005	53.32981	-27.96592	...	4	F
82006	53.31183	-27.96360	2.7944	2	F	82009	53.31181	-27.95781	0.8521	1	F
82013	53.34014	-27.92662	...	4	F	89999	53.21603	-28.03276	0.6648	1	F

TABLE 3

Notes: The labels in the instrument column are defined as: F = VLT / FORS2, V = VLT / VIMOS, X = VLT / XSHOOTER, M = Keck / MOSFIRE (Band *H* or *K*), D = Keck / DEIMOS, G = Gemini / GNIRS. The quality flag (Q) for the spectroscopic redshifts is Q = 1 for secure redshifts; Q = 2 for redshifts measured from only one or two strong lines; Q = 3 for tentative redshifts measured based on one or two very faint features; Q = 4 for those sources which were targeted but no redshift could be determined.